REFERENCE

Modelling of Optical Fibre Long-Period Grating Sensors

Rujie Hou

A thesis submitted in partial fulfilment of the requirements of

Sheffield Hallam University

for the degree of Master of Philosophy

December 2000

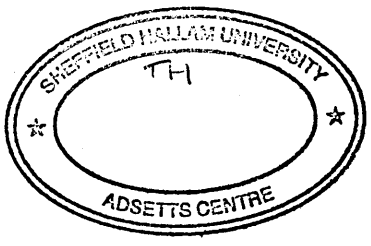
SHEFFIELD HALLAM UNIVERSITY
TH
ADSETTS CENTRE

ABSTRACT

In this thesis a mathematical model of the long-period fibre grating (LPG) sensor has been developed. Numerical simulation of the LPG transmission spectrum behavior is studied when changing the refractive index of the ambient. The attenuation bands are seen to shift to shorter wavelengths as the surrounding index is increased from 1 (air) to1.45 (near fibre cladding index). The results show that the long-period grating is very sensitive to changes in the surrounding index, especially when this index value approaches that of the cladding. This model shows for the first time that the coupling wavelength will shift even when the surrounding index is higher than the cladding index. Numerical results for cladding mode propagation constants, transmission spectra and resonance wavelengths are presented and compared with published data whenever appropriate. The proposed mathematical model can be used as a simulation tool to investigate LPG as a sensor. The LPG fibre when coated with a material and exposed to external analytes will change its refractive index (n_3), which in turn causes a shift in the transmission spectrum. This model can be applied to assist in the development of chemical sensors based on long-period fibre gratings.

ACKNOWLEDGEMENTS

I wish to extend my most sincere thanks to my Director of Studies Dr. Aseel Hassan, and my supervisors Professor Z. Ghassemlooy and Dr. Alexei Nabok for their patience and constant support and encouragement throughout this project. Words are not enough to express their contribution to my research progress.

I also would like to thank Professor Asim Ray, Professor John Young, Ms Judith Rossiter, Dr Reza Saatchi, Dr Andy Simmonds, Mr Alan Goude, Mr Paul Davies and Professor Barrie Jervis for their help during lectures I attended.

I should like to extend my grateful thanks to Kenneth P. Dowker for his help, encouragement and friendship.

My thanks must also be expressed to all of the staff in the School of Engineering and other students at the Electronics & IT division for their help and friendship throughout my studies in the Optical Communications Research Group. Andrew R. Hayes, John D, Siviter, Orjan Kindblom, Thomas Wilkop, Dr. Graham Swift, I. Sallehuddin, Chin-Ying Cheung, Laurenc-E C. Vigon, Bala Amavasai, Chun-Kit See, Nawras M Aldibbiat, B. C. Lee, Junhua Wang and Ruixin Gao deserve a special mention. Thanks also to Dr. Lin Zhang, Dr. Tom D. P. Allsop, Dr. Wei Zhang and Yu Liu in Photonics Research Group of Aston University, UK for their help and supply of LPGs. Thanks to Prof. Turan Erdogan (The Institute of Optics, University of Rochester, New York) and Dr. Vikram Bhatia (Optical Components Development, Corning, New York) for their reply to my E-mail questions.

Finally I would like to thank my wife Beiyan, my daughter Liwen and my parents for their love, support and encouragement.

TABLE OF CONTENTS

TABLE OF FIGURES

CHAPTER 1 INTRODUCTION

Fibre Bragg gratings are becoming very important elements in the field of optical fibre communications and sensing. The property and application of short-period fibre Bragg gratings are introduced first, to provide a stepping stone in understanding the operational characteristics of long-period gratings.

A fibre Bragg grating (FBG) is a periodic perturbation of the refractive index along a small section of the fibre length and is formed by exposure of the core to an intense UV optical interference pattern. The refractive index change Δn is positive in germanium doped single mode fibre with a magnitude ranging between 10^{-5} to 10^{-3}, and the length of FBG is normally within the region of 1-20 mm. When a light beam is coupled into one end of the fibre containing a Bragg grating, a small amount of this light is reflected. All the reflected light combine coherently to one large reflection at a particular wavelength when the grating period is equal to one half the wavelength of the input light as shown in Fig. 1.1. The Bragg wavelength, or resonance condition of the grating, is given by the expression

$$\lambda_B = 2n_{eff}\Lambda \tag{1.1}$$

where Λ is the grating pitch and n_{eff} is the effective index of the core. This is referred to as the Bragg condition, and the wavelength at which this reflection occurs is called the Bragg wavelength. Light signals at wavelengths other than the Bragg wavelength, which are not phase matched, are essentially transparent. Therefore, light propagates through the grating with negligible attenuation or signal variation, and only those wavelengths that satisfy the Bragg condition are affected and strongly back reflected. The ability to accurately present and maintain the grating wavelength is a fundamental

feature and hence an advantage of the fibre Bragg gratings.

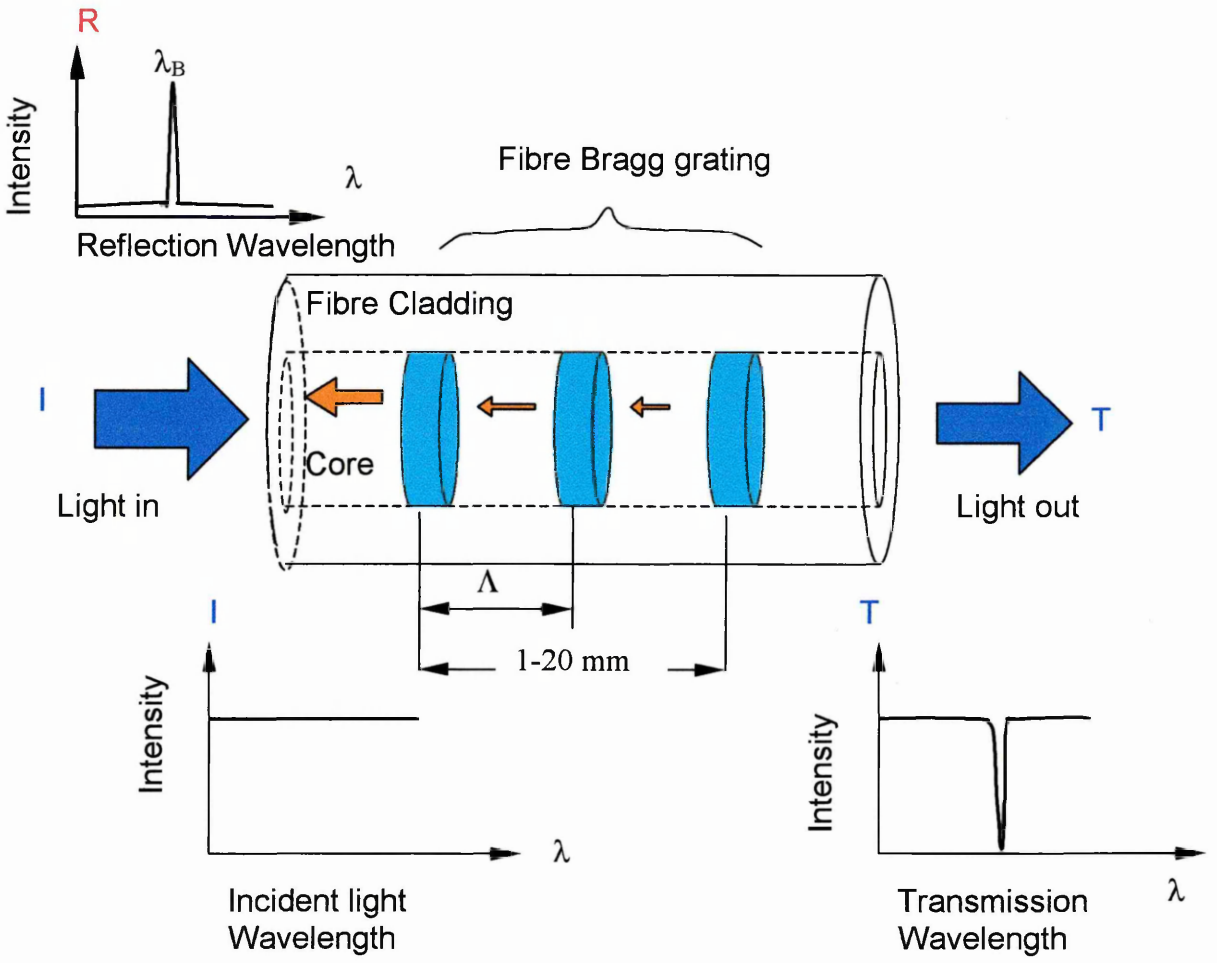

Fig. 1.1. A schematic diagram of a fibre Bragg grating.

Grating-based fibre sensors can be divided into two types: the fibre Bragg grating (FBG) or short-period grating and the long-period grating (LPG) or transmission gratings. Similar to FBG the LPG is a fibre with an ultraviolet (UV)-induced modulation of the index of refraction in the core, with typical modulation depth of 10^{-4} or greater, a period Λ between 100-500 μm and a length of 1-50 mm. The long period grating couples the guided fundamental mode in a single-mode fibre to forward-propagating cladding modes [Vengsarkar *et al* 1996]. The LPG couples light from core into cladding at a specific wavelength in accordance with the relation:

$$\lambda_i = \left(n_{core} - n_{clad}^{(n)}\right)\Lambda \qquad (1.2)$$

where n_{core} is the effective index of the core mode, and $n_{clad}^{(n)}$ is the effective index of the n^{th} axially symmetric cladding mode. Once in the cladding, the light quickly decays due to scattering losses, leaving loss bands in the guided core mode observed at the output. Fig. 1.2 shows a schematic diagram of a typical long-period grating.

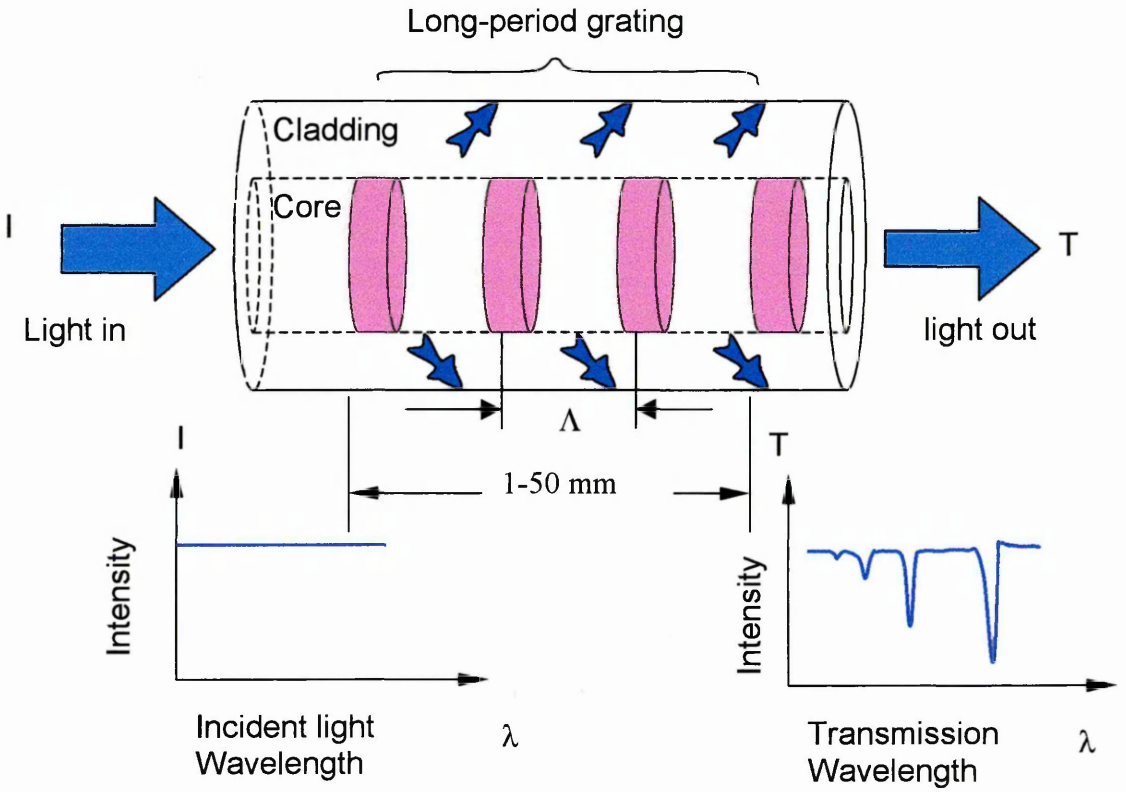

Fig. 1.2. A Schematic diagram of a typical long-period fibre grating.

1.1 Historical Developments

Optical fibre has already revolutionised telecommunications. Today, a single fibre-optic cable can transmit tens of millions of phone calls, data files, and video images. Optical fibres are hair-thin strands of glass that can guide light over a long distance. The fibre has an inner core surrounded by an outer cladding. Both the core and the cladding are usually made of silica glass, but the core has been made photosensitive by including

dopant such as germanium to increase its refractive index. The fibre is encased in a plastic coating to protect it.

The refractive index of the core can be modulated along the length of the fibre by exposing the core of the fibre to a pair of interfering beams of ultraviolet light. Hill and co-workers, at the Canadian Communications Research Centre in Ottawa, have discovered this phenomenon in 1978 [Hill *et al* 1978]. The phenomenon is called photosensitivity, which involves changing the refractive index of an optical waveguide on exposure to the external UV light source. Hill *et al* (1978) have used the interference pattern of two counter-propagating beams of blue-green light (488 or 514 nm) to form a refractive index grating on the core of germanium doped single-mode fibre. Such grating couples light from the forward-propagating LP_{01} fundamental mode to the reverse-propagating LP_{01} mode at a wavelength for which the phase-matching condition for mode coupling is satisfied [Hill *et al* 1978]. For the grating fabricated by Hill and co-workers, the reflection wavelength, also referred to as Bragg wavelength, was made equal to the writing UV wavelength since the grating was written by launching light in the fibre core. Thus, the application of these gratings in the visible spectrum has limited their use in communication systems at 1.31 μm, until late 1980s when the transverse holographic method for grating fabrication was proposed by Melts *et al* [Bhatia 1996]

In 1988, Meltz and co-workers [Meltz, *et al* 1989], at the United Technologies Research Centre in Connecticut, USA, have shown that a strong index of refraction change occurred when a germanium-doped fibre was exposed to direct UV light close to 5 eV. This coincides with the absorption peak of a germania-related defect at a wavelength range of 240-250 nm. They have made a Bragg grating in a fibre by illuminating the fibre from the side with two beams of ultraviolet light. The UV light had a wavelength

of 240 nm. Where the two UV light beams overlapped they interfered with each other to create a pattern of bright and dark stripes which made a grating in the fibre. The Bragg grating spacing is controlled by the angle between the two light beams; thus making reflectance possible at any wavelength. Even though the writing wavelength was at 244 nm, grating could be fabricated to reflect at any wavelength, thus permitting their use in modern telecommunication and sensor systems [Othonos and Kalli 1999]. Formation of a controlled grating in a fibre has therefore become possible and enabled the fabrication of a small grating of a finite length. This side-writing technique is easy, efficient and enables mass production of fibre gratings.

A new type of fibre grating called long-period fibre grating (LPG) was first presented by Vengsarkar and co-workers in 1996 as band-rejection filters [Vengsarkar *et al* 1996]. In these gratings the forward propagating fundamental core mode is coupled to various forward propagating cladding modes. At the same time, it has been shown that the coupling wavelengths shift when the external refractive index changes [Bhatia and Vengsarkar 1996]. Since then the LPG has been used as a novel fibre device in both telecommunications as a gain flattening and band rejection filter, and in the sensor field as a temperature, strain and refractive index sensor.

1.2 Recent Progress

Fibre optical sensors have many operational advantages over existing conventional electromechenical sensors. Fibre Bragg grating sensor technology has become one of the most progressive sensing topics of this decade in the field of optical fibre sensor technologies as they are capable of measuring a wide range of parameters [Grattan and Sun 2000, Hill and Melts 1997, Erdogan 997, Othonos and Kalli 1999, Kashyap 1999,

Rao 1999, Hotate 1997, Kersey 1997]. Typically, at 1.5 μm the wavelength strain responsivity is ~1 pm/nε (pico-meter per nano-strain), with a wavelength shift of 15 pm/^{o}C for temperature sensing [Othonos and Kalli 1999]. The fibre Bragg grating sensor has several advantages over all other fibre optic sensors; it is constructed from a single, unweakened fibre, with a linear measured response, including potentially low-cost and unique wavelength-multiplexing capacity.

Long-period grating can be used for temperature, strain, and index of refraction sensing [Bhatia 1996, Patrick *et al* 1998] and for simultaneous measurement of temperature and axial strain [Bhatia 1999]. Rapid progress has been made in chemical sensor [Patrick et al 1997], structure analysis and control [Vries *et al* 1998], medical application [Othonos and Kalli 1999] and biochemical sensors [Zhang 1999].

Fibre gratings now have broad applications in optical fibre products and networks. Gratings are incorporated in optical fibre devices for wavelength division multiplexing and dispersion compensation in many telecommunications applications [Giles 1997, Othonos and Kalli 1999, Kashyap 1999].

1.3 Tasks of the Project

The general objective of this research project is to develop a mathematical model for a long-period grating sensor and the use of MATLAB to implement the simulation. This includes:

1. Understanding the optical properties of fibre gratings, studying the mechanisms of fibre photosensitivity and fibre grating fabrication.

2. A comprehensive and detailed study of fibre Bragg grating (FBG) sensors and long-period grating (LPG) sensors.

3. Developing a mathematical model for index sensors based on long-period fibre grating using MATLAB programming.

4. Modelling of some practical examples for sensor applications. The results will be compared with data obtained from existing literature. The developed model can be used as a powerful tool for developing an LPG chemical sensor.

1. 4 Thesis Outline

The outline of this thesis is as follows. Chapter 2 covers fibre photosensitivity, fabrication of fibre grating and fibre Bragg grating property and theory. Chapter 3 will present the fibre Bragg grating applications, while Chapter 4 is devoted to the long-period fibre grating sensors and Chapter 5 presents modelling of the long-period grating sensor methods. In chapter 6 concluding remarks are included and future work is outlined.

CHAPTER 2 FIBRE BRAGG GRATING PROPERTY AND THEORY

2.1 Introduction

Photosensitivity is a very important aspect of the fibre grating phenomena. This chapter is a review of the literature on photosensitivity and fabrication of fibre gratings. Section 2.3 will introduce the principles of coupling mode theory and the diffraction grating allowing an easier understanding of fibre grating theory.

2.2 Photosensitivity and Fabrication of Fibre Gratings

2.2.1 Photosensitivity in Optical Fibre

Photosensitivity in optical fibre refers to a permanent change in the index of refraction of the fibre core when exposed to light with a characteristic wavelength and intensity that depends on the core material [Othonos and Kalli 1999]. Initially, photosensitivity was thought to be a phenomenon only associated with optical fibres having a large concentration of germanium (Ge) in the core and which was photoexcited with 240-250 nm ultraviolet (UV) light. Following many years of research, however, photosensitivity has been observed through photo-excitation at different UV wavelengths in a wide variety of different fibres, many of which do not have germanium as the only dopant and some of which contain no germanium at all. Nevertheless, germanium-doped optical fibre remains one of the most important materials for the fabrication of devices utilising photosensitivity.

2.2.2 Physical Mechanism Behind Photosensitivity

The precise principles of photosensitivity and the accompanying refractive index change have yet to be fully understood. It is clear that no single model can explain all the experimental results, as there are several microscopic mechanisms at work [Othonos and Kalli 1999]. There are many theories that have been formulated in order to explain the phenomenon of photosensitivity, two of which are explained in the following sections.

2.2.2.1 Colour-Centre Model

Defects are important to optical fibres because their absorption bands cause harmful transmission losses; these defects are called colour-centres [Othonos and Kalli 1999]. There is considerable evidence that photosensitivity of optical fibres is due to defect formation inside the Ge-doped core of silica fibres. The fibre core is often doped with germania during manufacturing in order to increase its refractive index and introduce an index step at the core-cladding interface. Typically the Ge concentration is 3-5% and is often increased to improve photosensitivity [Agrawal 1995]. The normal molecular structure of silica is tetrahedral, with each silicon atom being singly bonded to four oxygen atoms. In quartz, this tetrahedral forms a regular lattice, but in glass, they form a disordered structure. Since germanium atoms have the same valency they can replace the silicon atoms in the glass structure. The presence of Ge atoms leads to formation of oxygen-deficient bonds (such as Si-Ge, and Ge-Ge bonds) which act as defects in the silica matrix. This forms a defect band with an energy gap of about 5eV (energy required to break the bond), and 244 nm radiation from an excimer laser can break these defects such as Ge (1) and Ge (2) [Agrawal 1995]. The Ge (1) centre is an electron

trapped at a Ge atom co-ordinated to four O-Si next-nearest-neighbour atoms, while the Ge(2) centre is an electron trapped at a Ge atom co-ordinated to one O-Ge (≡ Ge-O-Ge ≡) and three O-Si next-nearest-neighbour atoms [Othonos and Kalli 1999] as shown in Fig. 2.1.

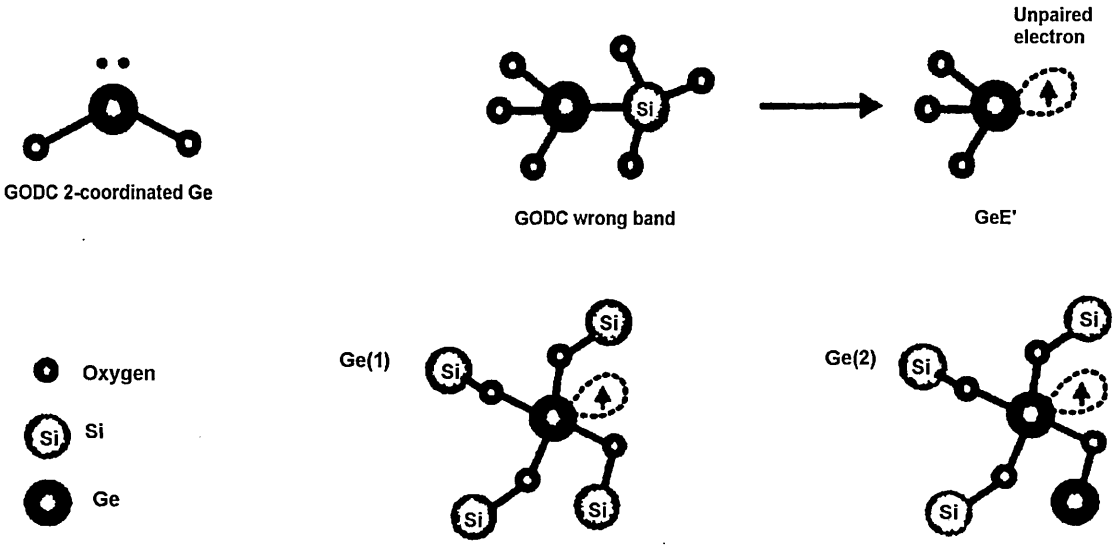

Fig. 2.1. A schematic of the GeE' centre, Ge(1) and Ge(2) electron trap centres [Othonos and Kalli 1999].

The presence of GeE' centres is crucial for the above physical mechanism of photosensitivity. Possible photochemical reaction for GeE' centre formation is as follows:

A Ge-Si (or Ge-Ge) bond is ionised by UV radiation; the bond is broken, resulting in a GeE' centre, a positive charged Si or Ge centre and free electron [Archambault 1994], as shown in Fig. 2.2. This electron may be retrapped at another defect site.

Most fibres show an increase in the population of GeE' centres after UV exposure. The change in the population of GeE' centres cause change in the UV absorption spectrum $\Delta\alpha$, which lead to a change in the refractive index directly through the Kramers-Kronig relation [Othonos and Kalli 1999], expressed as:

$$\Delta n_{eff}(\lambda) = \frac{1}{2\pi^2} P \int_0^{\infty} \frac{\Delta\alpha_{eff}(\lambda)}{1-(\lambda/\lambda')^2}\, d\lambda \qquad (2.1)$$

where P stands for the principle part of the integral, λ is the wavelength, and $\Delta\alpha_{eff}(\lambda)$ is the effective change in the absorption coefficient of the defect, given by

$$\Delta\alpha_{eff}(\lambda) = (1/L)\int_0^{L} \Delta\alpha(\lambda, z)\, dz \qquad (2.2)$$

where L is the sample thickness. This takes into account the fact that the bleaching beam is strongly attenuated as it passes through the sample, thus bleaching does not occur uniformly with increasing depth, and $\Delta\alpha_{eff}(\lambda)$ may be modelled as a Gaussian distribution. Eq. 2.1 may be used to calculate the index change that is induced by bleaching of the absorption bands. The boundaries are set to λ_1 and λ_2, the limits of the spectral range within which absorption change takes place and λ' is the wavelength for which the refractive index is calculated. Typically the index change $\Delta n\ (\lambda)$ is about 10^{-4} in the1.3~1.6 μm wavelength range, but can exceed 10^{-3} in fibres with high Ge concentration [Agrawal 1995].

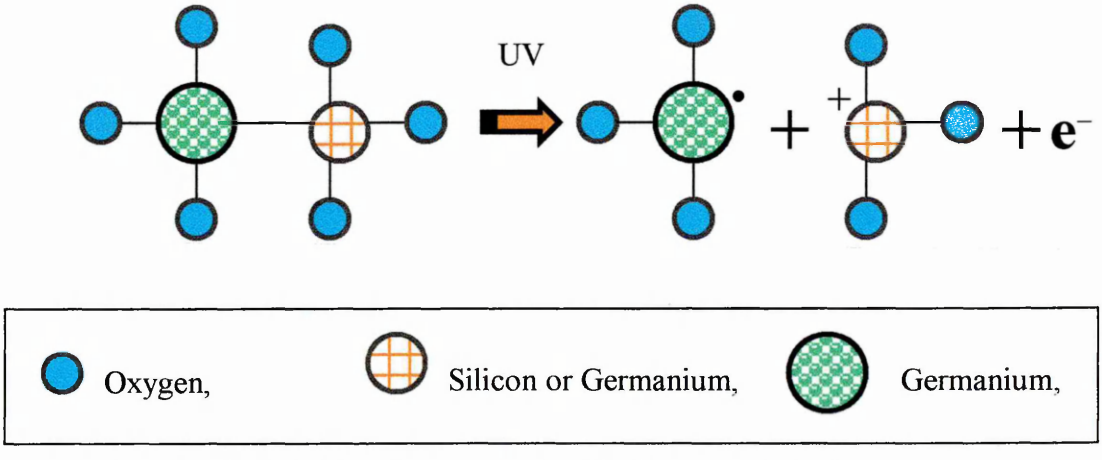

Fig. 2.2. The GeO defect of germania-doped silica, in which the atom adjacent to germanium is either a silicon or another germanium. It can absorb a photon to form a GeE' defect. The GeE' defect shows the extra electron (associated with the Ge atom), which may be free to move another GeE' hole site, or one of the Ge(n) defect centres [After Kashyap 1999].

Indeed fibre cores with a large concentration of Ge atoms are found to be more photosensitive and lead to larger index changes simply because $\Delta\alpha$ is large in Eq. 2.1. Support for this model also comes from recent observations that photosensitivity (the amount of index change) can be enhanced by two orders of magnitude by soaking the fibre in hydrogen gas at high pressures (200 atmospheres) and at room temperature. Presumably the density of Ge-Si oxygen-deficient bonds increases because hydrogen can recombine with oxygen atoms.

2.2.2.2 Permanent Electric Dipole Model

The dipole model is based on the formation of built-in periodic space-charge electric fields by the photo-excitation of defects. Photo-ionisation of the Germanium-oxygen deficient centre (GODC), Ge-Si, or Ge-Ge, creates positively charged GeE' hole-centres and free electrons as shown in Fig. 2.2. The defect is fixed to the matrix whereas the electron has enough energy to escape, diffusing away and getting trapped at neighbouring Ge (1) and Ge (2) sites to form negatively charged Ge $(1)^-$ and Ge $(2)^-$ respectively. The GeE' trapped holes and $Ge(1)^-$ and $Ge(2)^-$ trapped electrons result in electric dipoles with spacing of the order of several angstroms($\dot{A}$). Each resulting dipole will produce a static dc polarisation field that extends over molecular lengths [Othonos and Kalli 1999].

The internal electric field *E(x)* locally modifies the refractive index in accordance with [Saleh and Teich 1991]:

$$\Delta n = -\frac{1}{2} n^3 r E(x) \tag{2.3}$$

where *E(x)* is the internal electric field, *n* and *r* are the appropriate values of refractive

index and electro-optic coefficient for the material.

During the writing process of a Bragg grating, when the fibre is exposed to a UV interference pattern, the free electrons in the high intensity regions will diffuse until they are trapped by defects in the low intensity regions. This redistribution of charges within the fibre will create periodic space-charge electric fields. There is a $\pi/2$ phase shift of the index change relative to the interference pattern of the UV light (Othonos and Kalli 1999) as shown in Fig. 2.3.

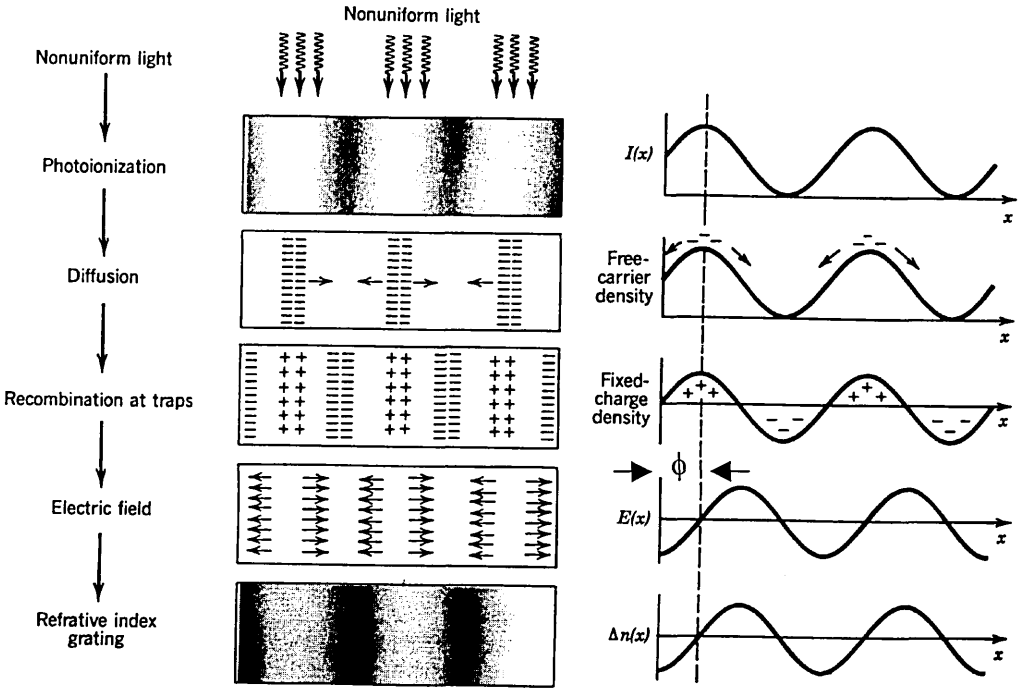

Fig. 2.3. Response of a photorefractive material to a sinusoidal spatial pattern [Bahaa and Saleh 1991]

From Fig. 2.3 we can see that the two coherent light beams intersect in an electro-optic crystal, forming an interference pattern. Electrons are excited where the intensity is large and migrate to regions of low intensity. The electric field associated with the resultant space charge operates through the electro-optic effect to produce a refractive index grating. ϕ is the phase shift (in radians) between the light interference pattern and index grating (Yariv 1997).

2.2.2.3 Enhanced Photosensitivity in Silica Optical Fibres by Hydrogen Loading

Since the discovery of photosensitivity and the first demonstration of grating formation in germanosilicate fibres, there have been considerable efforts made towards understanding and increasing the photosensitivity in optical fibre. Standard single-mode telecommunications fibres, doped with 3% germanium, typically display index changes of about 3×10^{-5}. In general, increasing the doping level at high temperatures can result in large index changes of about 5×10^{-4}. Increases in the photoinduced index modulations to values of the order of 10^{-3} and higher have been realised via low temperature hydrogen loading (hydrogenation).

Lemaire and co-workers [Lemaire, *et al* 1993] were the first to report a simple and highly effective approach for achieving a very high UV photosensitivity in optical fibres using low temperature hydrogen treatment prior to UV exposure. Fibres are soaked in hydrogen gas at temperatures ranging from $20-75\ ^{o}C$ and pressures from 20-750 atm (typically 150 atm), which results in diffusion of hydrogen molecules into the fibre core. Permanent changes in the fibre core index of 10^{-2} are possible.

High-temperature hydrogen treatment reduces germania, producing an enhanced concentration of GeO molecules. The addition of hydrogen to Ge-doped glass leads to the breakdown of the Si-O-Ge bonds, resulting in the formation of Si-OH bonds and germanium-oxygen deficiency centre (GODC), both of which lead to increase in the index of refraction [Bhatia 1996]. Chemically, the reduction process may occur as follows [Kashyap 1999]:

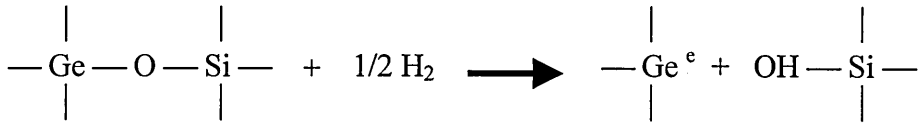

The other suggested reaction is the formation of GeH and OH ions from a Ge(2) defect. The GeH is responsible for the change in the refractive index via the Kramers-Kronig rule. The possible route may be as follows [Kashyap 1999]:

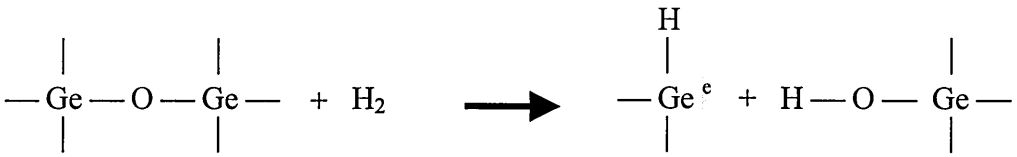

One advantage of hydrogen loading is the fabrication of Bragg gratings in any germanosilicate and germanium-free fibres. Another advantage is thermal treatment offers a simple method to obtain index modulation without resorting to the conventional method of irradiating the fibre with ultra-violet radiation [Bhatia 1996].

2.2.3 Fabrication of Fibre Grating

Typical long period gratings are fabricated by creating a periodic modulation of the refractive index in the core of the fibre. This is accomplished by exposing a fibre with germanium-doped core to ultraviolet (UV) light at wavelength of 244 nm or 248 nm, using one of three typical methods: (1) Holographic interferometry,
(2) Phase/Amplitude mask and (3) Point -by point writing [Zhang 1999]. For detailed technology see references by Othonos and Killi [1999] and Kashyap [1999].

2.2.3.1 *Holographic Interferometer Technology*

In the holographic interferometry method, two beams from the same light source are made to interfere on the core of the photosensitive fibre as shown in Fig. 2.4.

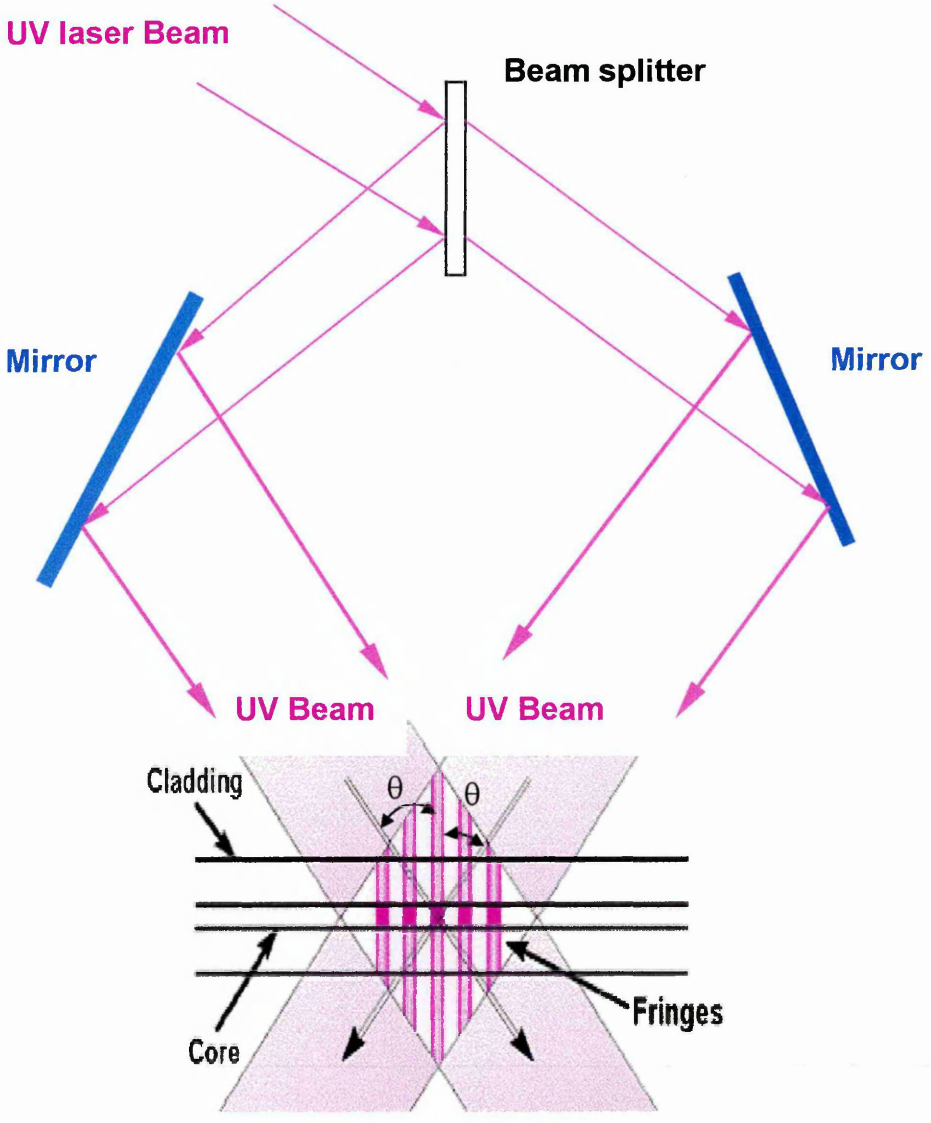

Fig. 2.4. A schematic diagram of holographic interferometer for fibre grating fabrication.

The grating period depends on the writing wavelength, and the half angle θ between the intersecting UV laser beams. The relation between them can be represented by [Agrawal 1995]:

$$\Lambda = \lambda_{UV} / 2 \sin\theta \qquad (2.4)$$

where λ_{UV} is the wavelength of the UV laser light. The LPG period Λ is controlled by adjusting the angle θ between the two laser beams.

Although the UV radiation covers both the fibre cladding and core, the index variation occurs only in the fibre core, because only the germanium-doped fibre core possesses sufficient photosensitivity to produce a permanent refractive index shift [Hill 1978].

The advantage of this approach is that it offers complete flexibility for producing LPG with various lengths and periods.

2.2.3.2 *Phase-Mask Technology*

In the Phase-mask method a laser beam passes through a phase or amplitude mask which is a diffractive optical element used to split the incoming beam into two diffraction orders, +1 and -1, with an equal power level, as shown in Fig. 2.5.

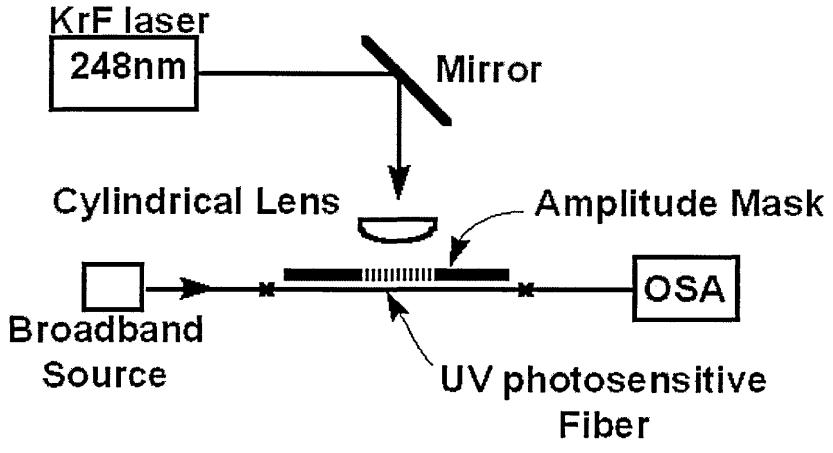

Fig. 2.5.a. A schematic of phase-mask method [Oct. 2000, URL: http://samsungelectronics.com/products/fiberoptics/d31.html]

The advantages of the phase mask technology are that it is not sensitive to environmental conditions such as vibrations, and thus fibre gratings can be mass produced with more consistent results as they do not depend on the set-up configurations. The main disadvantage is that different phase masks are required if the resonant wavelengths of the grating period are changed.

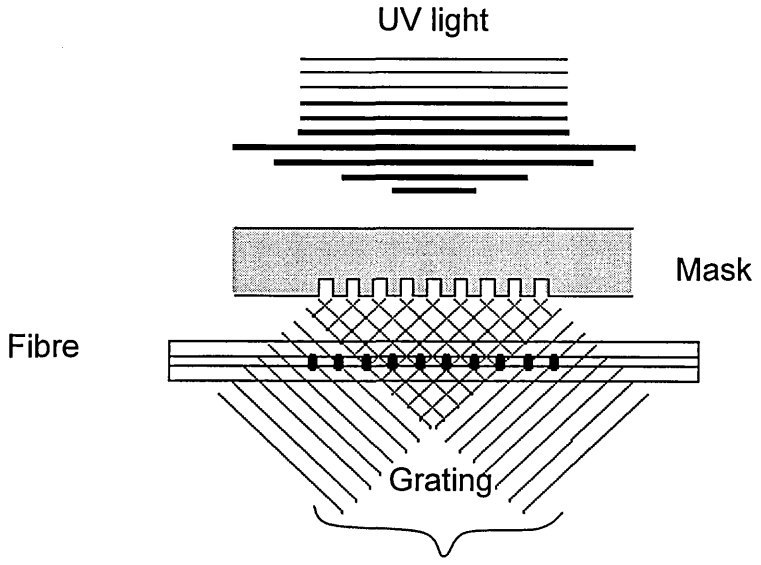

Fig. 2.5.b. Diffraction pattern of UV light onto fibre through amplitude mask.

In long period grating fabrication, the most commonly used methods employ amplitude masks made from chrome. The chrome amplitude mask cannot stand very high UV laser power, as the high-density UV laser beam will damage the chrome mask. Recently O/E LAND INC developed a high power metal mask for long-period gratings. The new metal mask can stand an UV laser beam intensity of 30 times greater than normal Chromium masks [http://www.o-eland.com /AmplitudeMasks.html].

2.2.3.3 *Point by Point Writing*

The third LPG fabrication method is point-by-point writing as shown in Fig. 2.6.

The focused laser beam passes through a slit onto the fibre as the fibre moves forward step by step. Each step moves the fibre exactly a distance equal to the desired periodicity Λ. Since the periodicity of LPGs are large (on the order of hundreds of micrometers), it is easy to control the step size by using a computer controlled step-motor. The advantage of point-by-point writing method is the ease of changing the LPG's periodicity allowing the production of very long LPGs [Zhang 1999].

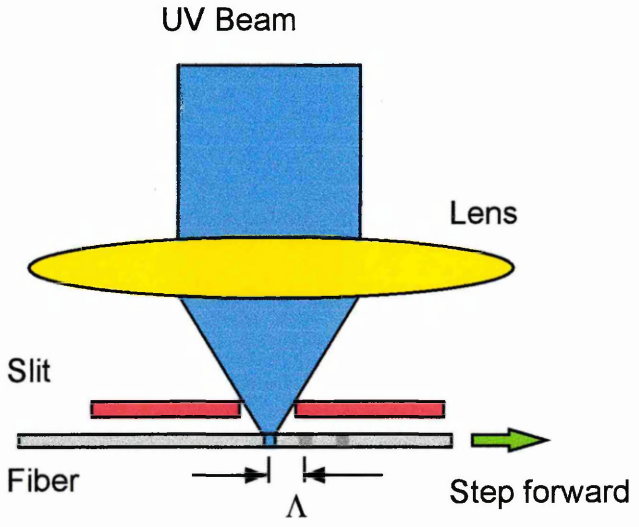

Fig. 2.6. Point-by-point writing [After Zhang 1999]

2.3 Fibre Bragg Gratings Theory

2.3.1 Coupling Mode Theory

Coupled mode theory is the theoretical approach that has been most widely applied to investigations of interactions likely to occur within an optical waveguide.

The coupling mode theory is one of the most popular techniques utilised in describing the behaviour of Bragg gratings, mainly due to its simplicity and accuracy in modelling the optical properties of most fibre gratings. This section does not provide a derivation of the coupling mode theory since it is well described in the literature [Yariv 1973,

Huang 1986, Hall 1987, Marcuse 1991, Agrawal 1995, and Erdogan 1997]. The derivation in this section closely follows the work given by Erdogan [Yariv 1973].

Consider the optical fibre of Fig. 2.7 that is disturbed by a perturbation of period Λ along the fibre axis, originating at $z = 0$ and terminating at $z = L$. This perturbation can be caused by a period variation in the core index.

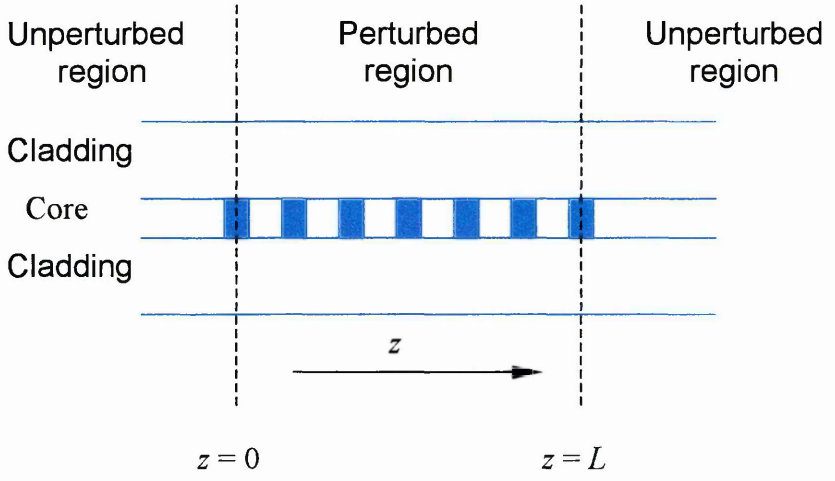

Fig. 2.7. Illustration of an optical fibre under perturbation. The perturbation exists from $z = 0$ to $z = L$.

Consider two modes denoted by a and b travelling along the positive z direction with discrete propagation constants β_a and β_b, respectively, such that,

$$a(z,t) = A(z)e^{i(\omega t-\beta_a z)} \tag{2.5}$$

$$b(z,t) = B(z)e^{i(\omega t-\beta_b z)} \tag{2.6}$$

where ω is the angular frequency and $A(z)$ and $B(z)$ are complex normalised amplitudes that are independent of z in a loss-less unperturbed fibre. The presence of a disturbance that causes the two modes to exchange energy such that $A(z)$ and $B(z)$ become function of the variation of the propagating distance. The objective of coupling mode theory is to find the variation in $A(z)$ and $B(z)$ as a function of z [Bhatia 1996]. Without resorting to

detailed mathematical analysis we can outline the basic coupling mode theory. The complex amplitudes *A(z)* and *B(z)* in this case are no longer constant but will be found to depend on *z*. They will be shown below to obey relations of the type [Yariv 1973]:

$$\frac{dA}{dz} = k_{ab} B e^{-i\Delta z} \tag{2.7}$$

$$\frac{dB}{dz} = k_{ba} A e^{+i\Delta z} \tag{2.8}$$

where k_{ab} and k_{ba} are termed as the cross-coupling coefficients (or coupling constants) and dictate the magnitude of coupling between the two modes. Δ is the phase mismatch between the propagating modes and is typically the difference in their propagation constant and is modified to:

$$\Delta = \beta_a - \beta_b - \frac{2\pi}{\Lambda} \tag{2.9}$$

An analysis of the coupling mode equations reveals that for synchronous transfer of power between the two modes, the value of Δ should ideally be of zero value. Using Eq. 2.9 we obtain what is commonly termed as the phase-matching condition between the two modes [Bhatia 1996].

$$\Delta\beta = \beta_a - \beta_b = \frac{2\pi}{\Lambda} \tag{2.10}$$

where $\Delta\beta$ is their differential propagation constant.

2.3.1.1 Co-Directional Coupling

This is the case where modes *a* and *b* carry power in the same direction. The total power carried by modes *a* and *b* is given by $|A(z)|^2$ and $|B(z)|^2$, respectively. Since in lossless system, there is no variation in the total power in the *z* direction, the conservation of total power is thus expressed as [Yariv 1973]:

$$\frac{d}{dz}\left(|A|^2+|B|^2\right)=0 \tag{2.11}$$

We can manipulate Eq. 2.7 and 2.8 to obtain:

$$k_{ab}=-k_{ba}^{*} \tag{2.12}$$

where, * denoted the complex conjugate. Assuming that only mode b carries power at z = 0, the boundary conditions are:

$$a(0)=0 \tag{2.13}$$

$$b(0)=A \tag{2.14}$$

which can be used to solve the coupling mode equations. Thus the complex modal amplitudes can be written as [Yariv 1997]:

$$A(z)=A\frac{2k_{ab}}{\sqrt{4k^2+\Delta^2}}\,e^{-i\left(\frac{\Delta z}{2}\right)}\sin\left[\frac{1}{2}\left(\sqrt{4k^2+\Delta^2}\right)z\right] \tag{2.15}$$

and

$$B(z)=Ae^{i\left(\frac{\Delta z}{2}\right)}\left\{\cos\left[\frac{1}{2}\left(\sqrt{4k^2+\Delta^2}\right)z\right]-i\frac{\Delta}{\sqrt{4k^2+\Delta^2}}\sin\left[\frac{1}{2}\left(\sqrt{4k^2+\Delta^2}\right)z\right]\right\} \tag{2.16}$$

where

$$k^2=|k_{ab}|^2 \tag{2.17}$$

The eigenmodes can now be obtained by substituting the values of the complex amplitudes $A(z)$ and $B(z)$ in Eqs. 2.5 and 2.6. The power in the two modes are given by [Bhatia 1996]:

$$P_a(z)=|A(z)|^2=P_0\frac{\sin^2\left[kz\sqrt{1+\left(\frac{\delta}{k}\right)^2}\right]}{1+\left(\frac{\delta}{k}\right)^2} \tag{2.18}$$

and

$$P_b(z) = |B(z)|^2 = P_0 \left\{ \frac{\cos^2\left[k z \sqrt{1+\left(\frac{\delta}{k}\right)^2} \right] + \left(\frac{\delta}{k}\right)^2}{1+\left(\frac{\delta}{k}\right)^2} \right\} \qquad (2.19)$$

where $\delta = \Delta/2$ is called the detuning parameter and P_0 is the incident power in eigenmode b ($P_0 = P_b(0) = |A|^2$). Hence we see that the two modes have sinusoidal variations in the propagating power. The frequency and magnitude of power coupling is a function of the detuning ratio δ/k . Fig. 2.8 depicts the variation in the incident power normalised values of P_a and P_b as function of $k z$ for two different values of detuning ratio. From Fig. 2.8 it is evident that under the condition of phase-mismatch ($\delta \neq 0$), the mode coupling is small and become negligible for $\delta/k >> 1$.

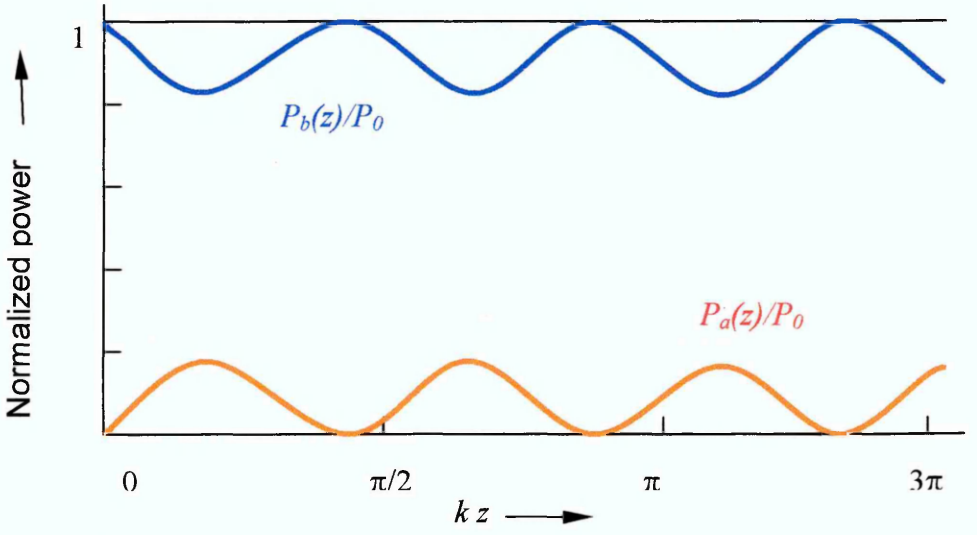

Fig. 2.8 Variation of the power of the two co-propagating eigenmodes a and b involved in coupling for phase-mismatched ($\delta/k = 2$) case. The values are normalised to the incident power in mode b ($P_b = P_0$) [After Bhatia 1996].

On the other hand, at phase match condition ($\delta = 0$), Eqs. 2.18 and 2.19 can be modified to yield:

$$P_a(z) = P_0 \sin^2(k z) \qquad (2.20)$$

$$P_b(z) = P_0 \cos^2(kz) \tag{2.21}$$

The above equations predict a large degree of interaction between the two modes depending on the value of the coupling coefficient. This is confirmed by Fig. 2.9, which shows that the modes are continuously exchanging power in the region of perturbation with a spatial period given by π / k.

At $z = 0$, all of the power is in the b mode. For $z > 0$, the power oscillates back and forth (periodically) between the waveguides. In particular, coupling transfer from waveguide b to waveguide a occurs at a distance $L = \frac{\pi}{2k}$ known as the transfer length [Hall 1987].

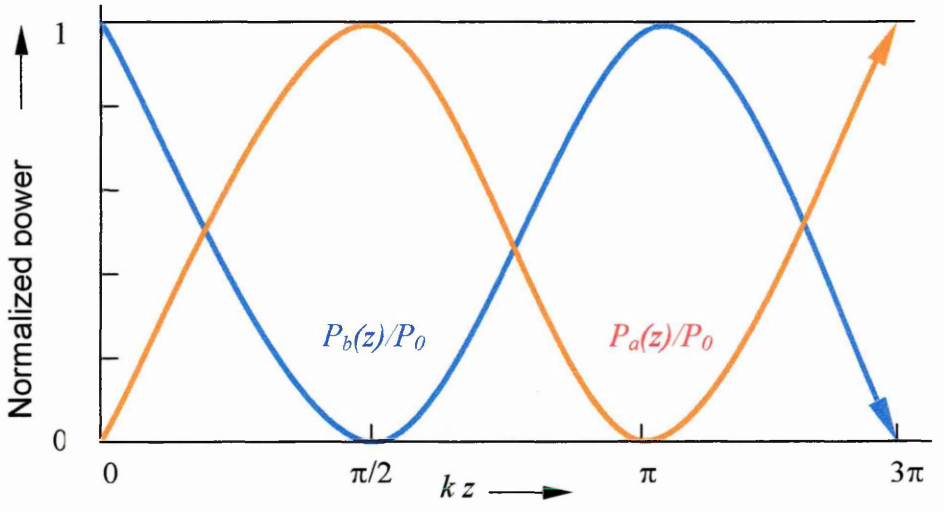

Fig. 2.9. Variation of the power of two co-propagating eigenmodes (a) and (b) involved in coupling for phase-matched ($\delta / k = 0$) case. The values are normalised to the incident power in mode b ($P_b = P_0$) [After Bhatia 1996].

The modal interaction terminates at $z = L$, where the perturbation ceases to exist. At that point, the ratio C ($C \leq 1$) of the power in mode (a) to that originally in (b)can be determined from Eq. 2.18 and 2.19 as [Hall 1987]:

$$C = \frac{P_a(L)}{P_b(0)} = \frac{\sin^2\left[kL\sqrt{1+\left(\frac{\delta}{k}\right)^2}\right]}{1+\left(\frac{\delta}{k}\right)^2} \qquad (2.22)$$

where δ is the detuning parameter $\delta = \frac{1}{2}\left[\beta_a - \beta_b - \frac{2\pi}{\Lambda}\right]$, k is the coupling constant for the grating and L is the grating length.

At $z = L$, the normalised power T_b remaining in mode b is simply given by $T_b = 1 - C$. For most applications the length L of the perturbation region is constant while the coupling coefficient k is varied to achieve complete power transfer from mode b to a. Although the maximum power transfer occurs when $kL = m\ \pi/2$, where m is an integer, the device operation is typically optimised for m=1, which yield $k = \pi/2L$ [Bhatia 1996]. The coupling constant (k) in LPG is proportional to the UV-induced core index change (Δn) and is typically increased to maximise the power transfer to the cladding mode. Thus Δn (and hence, k) is increased until the condition $kL = \pi/2$ is met [Vengsarkar *et al* 1996].

2.3.1.2 Contra-Directional Coupling

In this case the propagation in unperturbed medium is considered where the propagation of mode a towards the left (- z) and mode b towards right (+ z) is described by:

$$a(z,t) = A(z)e^{i(\omega t + \beta_a z)} \qquad (2.23)$$

$$b(z,t) = B(z)e^{i(\omega t - \beta_b z)} \qquad (2.24)$$

where A and B are constants and β_a and β_b are the respective propagation constants of the two modes. A periodic perturbation can lead to power exchange between the two modes. Conservation of total power can be expressed as [Yariv 1973]:

$$\frac{d}{dz}\left(|A|^2+|B|^2\right)=0 \qquad (2.25)$$

The relation between the cross-coupling coefficients is modified to

$$k_{ab}=k_{ba}^{*} \qquad (2.26)$$

so that

$$\frac{dA}{dz}=k_{ab}Be^{-i\Delta z} \qquad (2.27)$$

$$\frac{dB}{dz}=k_{ba}^{*}Ae^{+i\Delta z} \qquad (2.28)$$

where * denotes the complex conjugate. In this case we take the mode b with an amplitude $B(0)$ to be incident at $z = 0$ on the perturbation region which occupies the space between $z = 0$ and $z = L$. Since mode a is generated by the perturbation we have $a(L) = 0$. With these boundary conditions the solution of Eq. 2.27 and 2.28 is given by [Yariv 1973]:

$$A(Z)=B(0)\frac{2ik_{ab}e-i(\Delta z/2)}{-\Delta\sinh\frac{SL}{2}+iS\cosh\frac{SL}{2}}\sinh\left[\frac{S}{2}(z-L)\right] \qquad (2.29)$$

$$B(Z)=B(0)\frac{e-i(\Delta z/2)}{-\Delta\sinh\frac{SL}{2}+iS\cosh\frac{SL}{2}}\left\{\Delta\sinh\left[\frac{S}{2}(z-L)\right]+iL\cosh\left[\frac{S}{2}(z-L)\right]\right\} \qquad (2.30)$$

where $S\equiv\sqrt{4k^2-\Delta^2}$, $k\equiv|k_{ab}|$.

Under phase-matching conditions $\Delta = 0$, gives:

$$A(Z)=B(0)\left(\frac{k_{ab}}{k}\right)\frac{\cosh[k(z-L)]}{\cosh(kL)} \qquad (2.31)$$

$$B(Z)=B(0)\frac{\cosh[k(z-L)]}{\cosh(kL)} \qquad (2.32)$$

A plot of modes power $|B(z)|^2$ and $|A(z)|^2$ for this case is shown in Fig. 2.10.

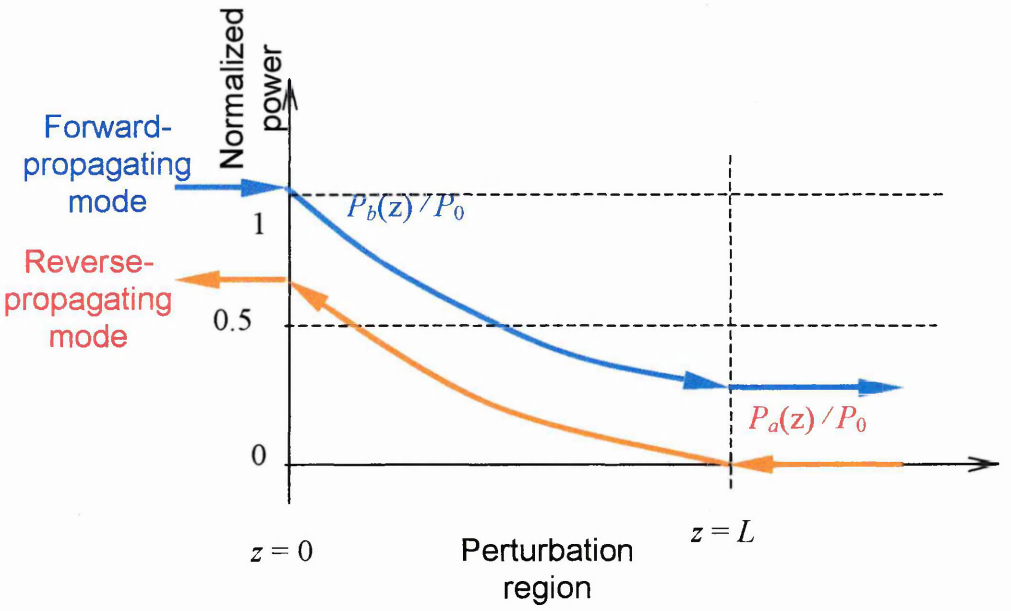

Fig. 2.10. The transfer of power from an incident forward wave $B(z)$ to a reflected wave $A(z)$ for the case of contra-directional coupling for the phase-matched ($\Delta = 0$) condition [After Bhatia 1996].

The reflectivity $R = |B(z=0)/A(z=0)|^2$ is given by [Hall 1987]:

$$R = \frac{\sinh^2(kL\sqrt{1-\Delta^2/k^2})}{\cosh^2\left(kL\sqrt{1-\Delta^2/k^2}\right)-\Delta^2/k^2} \tag{2.33}$$

The normalised residual power T in the mode b at $z = L$ is $T = 1 - R$ [Bhatia 1996].

By setting $\Delta = 0$ in Eq. 2.33, the maximum reflectivity (R_{max}) is given by [Agrawal 1995]:

$$R_{max} = \tanh^2 kL \tag{2.34}$$

For $kL = 2$, $R_{max} = 0.93$. The condition $kL > 2$ with $k = 2\pi\delta n/\lambda$ (δn is a value of peak induced-index change) can be used to estimate the grating length required for high reflectivity. For $\delta n \sim 10^{-4}$ and $\lambda = 1.55$ μm, L should exceed 5 mm to yield $kL > 2$ [Agrawal 1995].

Comparing the co-directional coupling equations (Eqs. 2.7 and 2.8) with the contra-directional coupling equations (Eqs. 2.27 and 2.28), the only difference found is the minus sign in the second equation of each pair [Hall 1987].

The coupled-mode formalism is not restricted to problems for which only two waves propagate. The restriction that only two modes propagate is usually an approximation. The number of equations increases with the number of propagating modes, which means that exact analytical solutions are few and far between when more than two modes propagate. Analysis of general coupled mode theory formalism is given in Appendix 4.

2.3.2 Diffraction Grating

Before deriving the theory of fibre Bragg gratings, it is important that the principle of diffraction gratings are understood. Diffraction grating is an optical component, which can be made of a transparent plate with a periodically varying thickness or a periodically graded refractive index. Consider here a diffraction grating made of a thin transparent plate placed in the $z = 0$ plane, the thickness of which varies periodically in the x direction with a period Λ. This plate converts an incident plane wave of wavelength λ, travelling at a small angle θ_i with respect to the z-axis, into several plane waves travelling at small angles with respect to each other, as shown in Fig. 2.11.

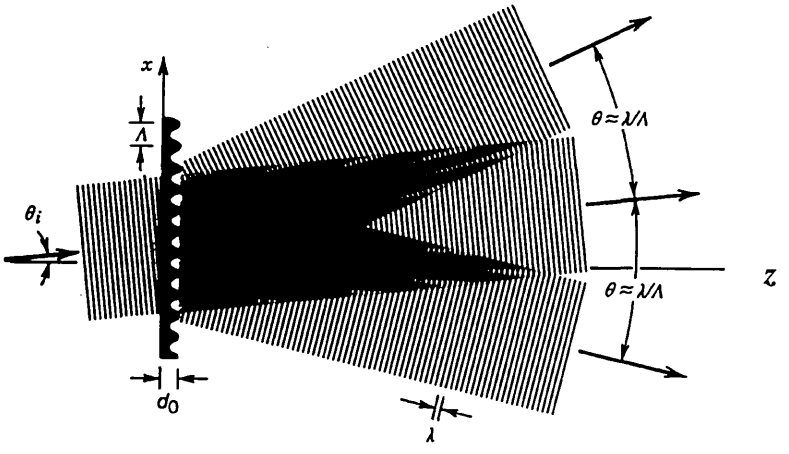

Fig. 2.11. A thin transparent plate with periodically varying thickness serves as a diffraction grating [Saleh 1991].

In Fig. 2.11, the d_0 is the thickness of the thin transparent plate. The diffraction grating equation is expressed as [Saleh 1991]

$$\theta_m = \theta_i + m\frac{\lambda}{\Lambda}, \qquad m = 0, \pm 1, \pm 2, \ldots, \text{ with the } z\text{-axis}, \tag{2.35}$$

where m is called the diffraction order.

The diffracted waves are separated by an angle $\theta = \lambda / \Lambda$. The above grating equation is valid in the paraxial approximation (when all angles are small). This approximation is applicable when the period Λ is much greater than the wavelength λ, and in this case the angle of diffraction will be small. In the more general analysis of thin diffraction gratings, without the use of the paraxial approximation, the incident plane wave is converted into several plane waves at angles θ_m satisfying the following equation [Saleh 1991]:

$$\sin\theta_m = \sin\theta_i + m\frac{\lambda}{\Lambda} \tag{2.36}$$

A fibre Bragg grating is simply an optical diffraction grating (see Fig. 2.12) and thus its effect upon a light wave incident in the grating at an angle θ_1 can be described by the familiar diffraction equation [Erdogan 1997]:

$$n\sin\theta_2 = n\sin\theta_1 + m\frac{\lambda}{\Lambda} \tag{2.37}$$

where θ_2 is the angle of the diffracted wave.

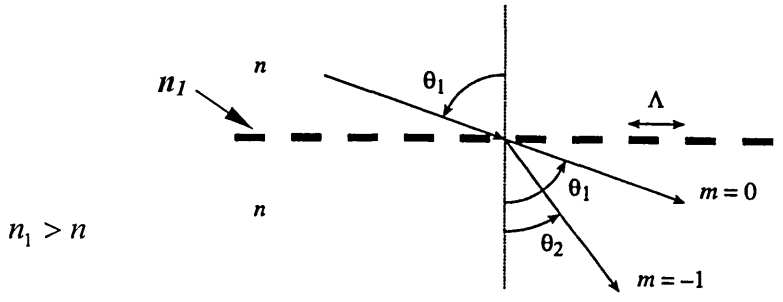

Fig. 2.12. The diffraction of a light wave by a grating [Erdogan 1997].

This equation predicts only the angles at which constructive interference occurs, but it is nevertheless capable of determining the wavelength at which a fibre grating most efficiently couples light between two modes.

2.3.3 Fibre Bragg Grating

In fibre Bragg gratings (also called reflection or short-period gratings), coupling occurs between modes travelling in opposite directions. Fig. 2.13 illustrates reflection by a Bragg grating of a mode with a bounce angle of θ_1 into the same mode travelling in the opposite direction with a bounce angle of $\theta_2 = -\theta_1$.

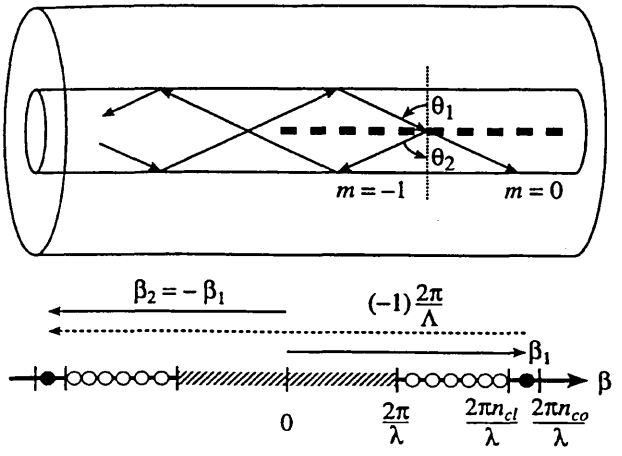

Fig. 2.13. Ray-optic illustration of core-mode Bragg reflection by a fibre Bragg grating. The β axes below the diagram demonstrate the grating condition in Eq. 2.37 for m = −1 [Erdogan 1997].

We may rewrite Eq 2.37 for guided modes as

$$n \sin\theta_2 = n \sin\theta_1 + m\frac{\lambda}{\Lambda} \quad ,$$

multiplying both side by $\frac{2\pi}{\lambda}$, gives

$$\frac{2\pi}{\lambda} n \sin\theta_2 = \frac{2\pi}{\lambda} n \sin\theta_1 + \frac{2\pi}{\lambda} \mathrm{m}\frac{\lambda}{\Lambda}$$

Since the mode propagation constant β is simply $\beta = (2\pi / \lambda)\, n_{eff}$, where $n_{eff} = n_{co} \sin\theta$, n_{eff} is the effective refractive index of core, and n_{co} is its refractive index, then

$$\frac{2\pi}{\lambda} n_{eff\,2} = \frac{2\pi}{\lambda} n_{eff\,1} + \mathrm{m}\frac{2\pi}{\Lambda}$$

Since $\mathrm{k} = \frac{2\pi}{\lambda}$, this gives:

$$\mathrm{k}\, n_{eff\,2} = \mathrm{k}\, n_{eff\,1} + m\frac{2\pi}{\Lambda}$$

$$\beta_2 = \beta_1 + \mathrm{m}\frac{2\pi}{\Lambda} \tag{2.38}$$

For first-order diffraction, which usually dominates in a fibre grating, $m = -1$. This condition is illustrated on β axis shown in Fig. 2.13. The solid circles represent bound core modes ($n_{cl} < n_{eff} < n_{co}$), the open circles represent bound cladding modes ($1 < n_{eff} < n_{cl}$), and hatched regions represent the continuum of radiation modes. Negative β value describes modes that propagate in the opposite direction. By using Eq. 2.38 and recognising $\beta_2 < 0$, the resonant wavelength for reflection of a mode of index $n_{eff\,1}$ into a mode of index $n_{eff\,2}$ is derived as follows:

Since $n_{eff} = \frac{\beta}{k}$, and $k = \frac{2\pi}{\lambda}$, then Eq. 2.38 can be rewritten as follows

$$\frac{\beta_2}{k} = \frac{\beta_1}{k} + m\frac{2\pi}{k\Lambda}$$

$$\frac{\beta_2}{k} = \frac{\beta_1}{k} + m\frac{2\pi}{(\frac{2\pi}{\lambda})\Lambda}$$

$$n_{eff\,2} = n_{eff\,1} + m\frac{\lambda}{\Lambda}$$

and remembering $\beta_2 < 0$, if $m = -1$

$$n_{eff\,2} = n_{eff\,1} + (-1)\frac{\lambda}{\Lambda} \tag{2.39}$$

If the two modes are identical ($n_{eff1} = -n_{eff2}$), we get the familiar result for the Bragg reflection:

$$\lambda = 2\, n_{eff1}\Lambda = 2\, n_{eff}\Lambda \tag{2.40}$$

Fibre phase gratings are produced by exposing optical fibre to a spatially varying pattern of ultraviolet intensity. The optical properties of a fibre grating are essentially determined by the variation of the induced index change $\overline{\delta}\, n_{eff}$ along the fibre axis z. Fig. 2.14 illustrates the main type of fibre Bragg gratings

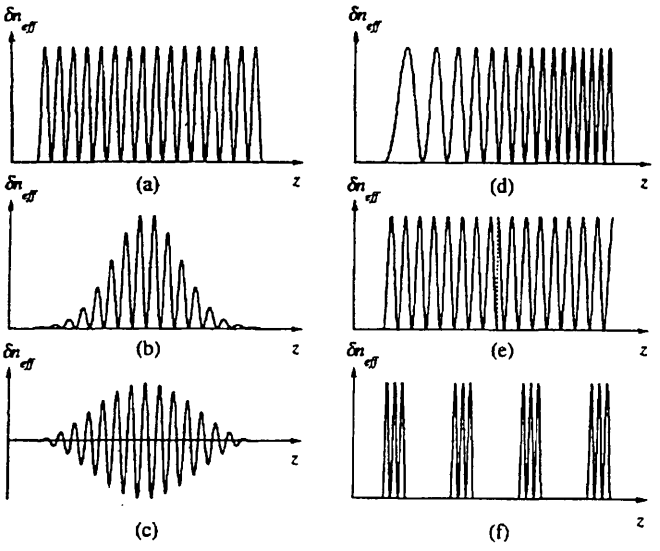

Fig. 2.14. Common types of fibre gratings as classified by variation of the induced index change along the fibre axis, including: (a) uniform with positive only index change, (b) Gaussian-apodized, (c) raised-cosine-apodized with zero-dc index change, (d) chirped, (e) discrete phase shift (of π), and (f) superstructure [Erdogan 1997 a].

When a phase grating is induced in a fibre, it exists only in the fibre core, changing the core index (n_1) to $n_1(z)$ but leaving the cladding (n_{cl}) and surrounding (n_3) indices unchanged, as follows [Erdogan 1997 b]:

$$n(r, z) = \begin{cases} n_1(z) = n_1 + \overline{\delta} n_{eff}(z)\left\{1 + v\cos\left[\dfrac{2\pi}{\Lambda} z + \phi(z)\right]\right\} & r \le a_1 \\ n_2 & a_1 \le r \le a_2 \\ n_3 & r > a_2 \end{cases} \tag{2.41}$$

where a_1 is the core radius, a_2 is the cladding radius, n_1 is the unperturbed core index, Λ is the period of the grating, $\bar{\delta} n_{eff}(z)$ describes the profile of the "dc" induced-index change, averaged over a grating period. $\phi(z)$ describes the grating chirp, and v is the induced-index fringe modulation, where $0 \leq v \leq 1$, as shown in Fig. 2.15.

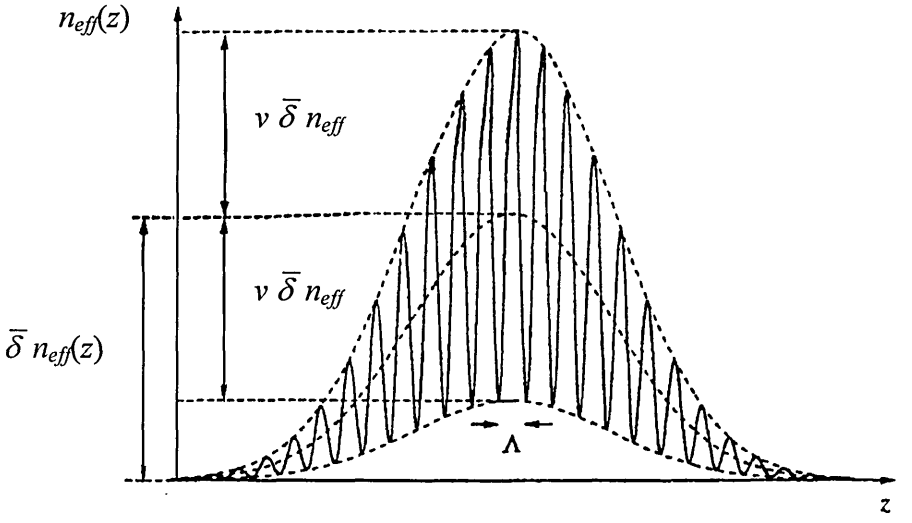

Fig. 2.15. A diagram showing the ultraviolet-induced refractive index change in the core for a grating with a Gaussian profile along the fibre z-axis.

Here we will merely outline the fibre Bragg grating transmission and long-period grating transmission without resorting to detailed mathematical analysis. The reflectivity of uniform Bragg grating of length L with constant modulation amplitude and period is given by [Erdogan 1997a]:

$$\rho = \frac{-k \sinh\left(\sqrt{k^2 - \hat{\sigma}^2}\, L\right)}{\hat{\sigma} \sinh(\sqrt{k^2 - \hat{\sigma}^2}\, L) + i\sqrt{k^2 - \hat{\sigma}^2} \cosh(\sqrt{k^2 - \hat{\sigma}^2}\, L)} \tag{2.42}$$

where $\hat{\sigma}$ is calculated from

$$\hat{\sigma} \equiv \delta + \sigma - \frac{1}{2}\frac{d\phi}{dz} \tag{2.43}$$

The detuning δ is defined as:

$$\delta \equiv \beta - \frac{\pi}{\Lambda} = \beta - \beta_D$$

$$= 2\,\pi\, n_{eff}\left(\frac{1}{\lambda} - \frac{1}{\lambda_D}\right) \tag{2.44}$$

where $\lambda_D = 2n_{eff}\Lambda$ is the design peak reflection wavelength, σ is the "dc" coupling coefficient defined by:

$$\sigma = \frac{2\pi}{\lambda}\bar{\delta}n_{eff} \tag{2.45}$$

and k is the "ac" coupling constant defined by:

$$k = \frac{\pi}{\lambda} v \bar{\delta} n_{eff}\,. \tag{2.46}$$

If the grating is uniform along z, then $\bar{\delta}n_{eff}$ is a constant and $d\phi/dz = 0$, and thus k, σ, and $\hat{\sigma}$ are constants.

Using Eq. 2.42, a number of Bragg grating reflectivity plots can be generated as shown in Fig. 2.16 and Fig. 2.17. The plots were generated using MATLAB, and the parameters used are: Grating length: 0.84×10^{-3} m, Centre wavelength: 1.286×10^{-6} m, Wavelength range: 1.286×10^{-6} – 1.290×10^{-6} m.

The MATLAB codes are given in Appendix 3.1.

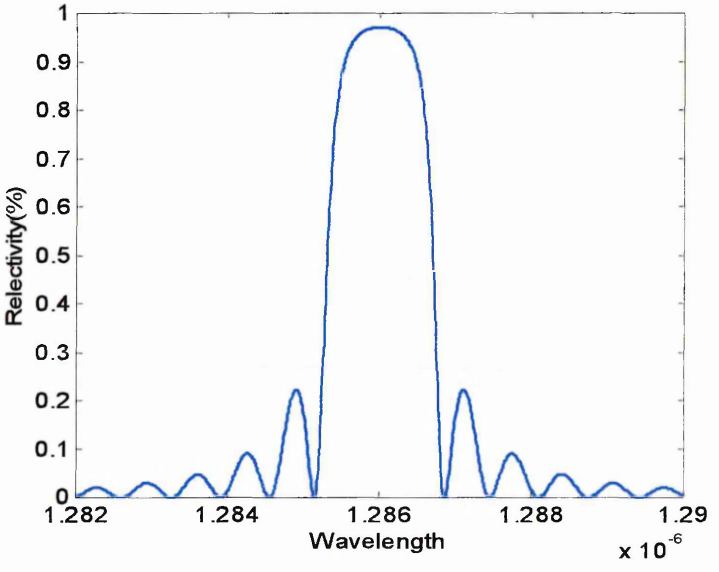

Fig. 2.16. Calculated reflection of a Bragg grating

The fibre Bragg grating reflectivity increases and it becomes narrower as the fibre Bragg grating length increases as shown in Fig. 2.17.

The MATLAB codes are given in Appendix 3.2.

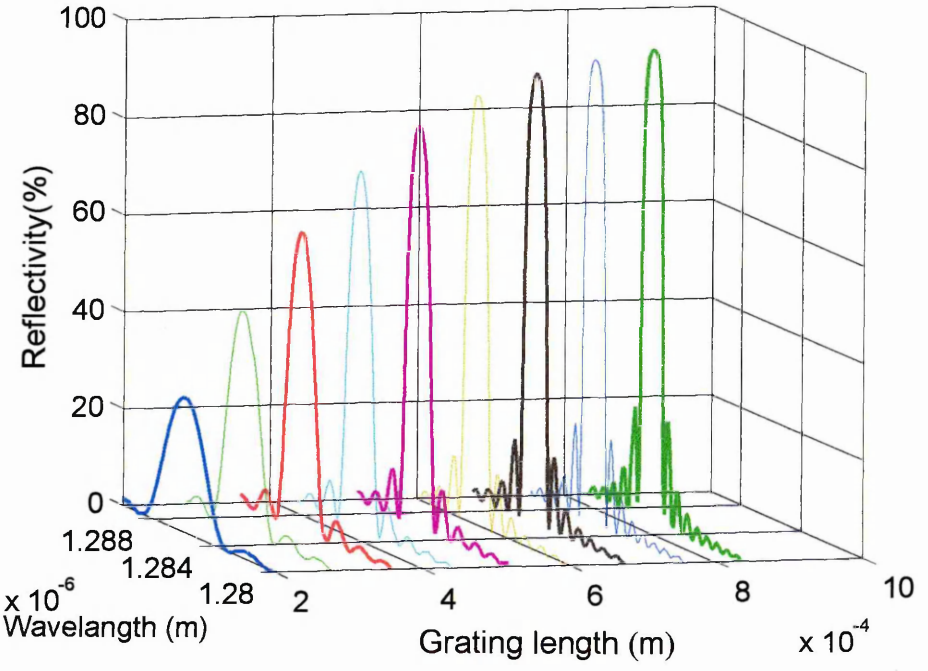

Fig. 2.17. Reflectivity versus wavelength for a range of fibre Bragg grating lengths.

2.3.4 Long-Period Grating

Fibre Bragg gratings can be broadly classified into two types: the Bragg grating (also called the reflection or short-period grating), in which coupling occurs between modes travelling in opposite directions; and long-period gratings (also called transmission gratings). Diffraction by transmission grating of a mode with a bounce angle of θ_1 into a co-propagating mode with a bounce angle of θ_2 is illustrated in Fig. 2.18. In this illustration the first mode $m = 0$ is a core mode while the second is a cladding mode ($m = 1$). Since β_2, in this case, is positive, Eq. 2.38 ($\beta_2 = \beta_1 + m\frac{2\pi}{\Lambda}$) predicts the resonant wavelength for a long-period grating as:

$$\lambda = (n_{co} - n_{cl})\,\Lambda \tag{2.47}$$

For co-propagating coupling at a given wavelength, evidently a much longer grating period Λ is required than for counter-propagating coupling [Erdogan 1997 a].

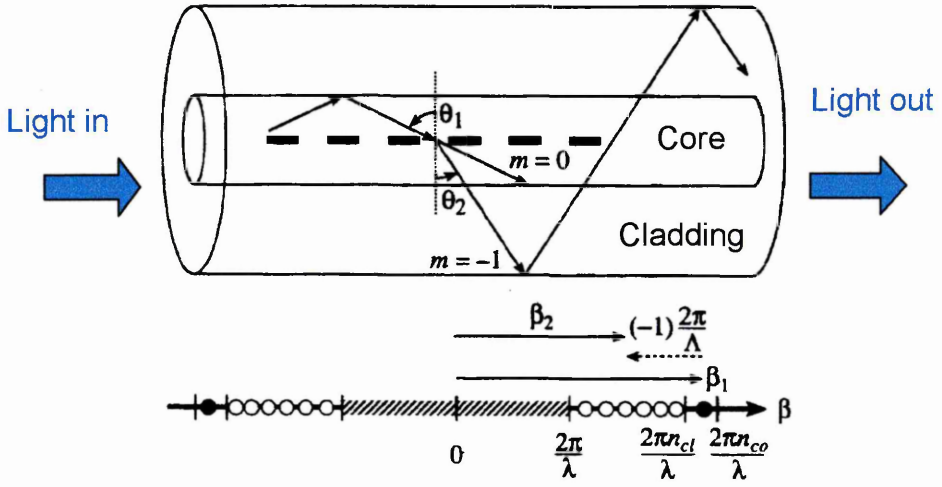

Fig. 2.18. Cladding-mode coupling by a fibre transmission grating. The β axes below the diagram demonstrate the grating condition in Eq.2.38 for $m = -1$ [after: Erdogan 1997 a].

For a long period grating, transmission can be approximately determined by using expressions derived in the literature [Hall 1987] for co-directional mode coupling. The ratio of power coupled into the n^{th}-cladding mode ($P_{cl}^{(n)}(L)$) to the initial power contained in the guided LP_{01} mode (P_{01}) is given by [Vengsarkar *et al* 1996]:

$$\frac{P_{cl}^{(n)}(L)}{P_{01}} = \frac{\sin^2\left[k_{m-01}^{cl-co} L \cdot \sqrt{1+\left(\dfrac{\delta}{k_{m-01}^{cl-co}}\right)^2}\right]}{1+\left(\dfrac{\delta}{k_{m-01}^{cl-co}}\right)^2} \tag{2.48}$$

where δ is the detuning parameter given by:

$$\delta \equiv \frac{1}{2}\left\{\beta_{core} - \beta_{clad} - \frac{2\pi}{\Lambda}\right\}$$

$$= \pi \Delta n_{eff} \left(\frac{1}{\lambda} - \frac{1}{\lambda_D} \right) \tag{2.49}$$

where β_{core} is the propagation constant of fibre core and β_{clad} is that of fibre cladding. L is the grating length and k_{m-01}^{cl-co} is the coupling constant for the long-period grating. Details for the calculation of k_{m-01}^{cl-co} can be found in the literature [Erdongan 1997a]. The coupling constant k_{m-01}^{cl-co} is proportional to the UV-induced index change, which forms the grating and is typically increased to maximise the power transfer to the cladding mode. Thus Δn and hence k_{m-01}^{cl-co} are increased until the condition $k_{m-01}^{cl-co} L = \pi / 2$ is met. Using MATLAB, the ratio of coupling power (Eq. 2.48) has been calculated and the results are shown in Fig. 2.19. The figure below was plotted using the MATLAB code given in Appendix 3.3.

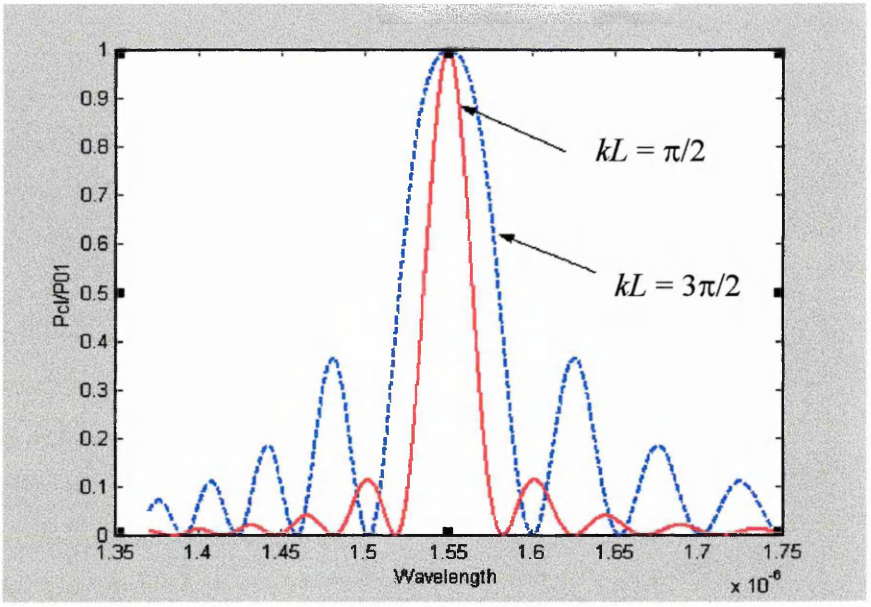

Fig. 2.19. Calculated ratio of power coupled into the cladding mode to the initial power contained in the guided LP_{01} mode through uniform long period gratings, with $kL = \pi / 2$ (solid line) and $kL = 3\pi / 2$ (dashed line).

The transmission of long-period grating is given by the following expression:

$$T_{LPG} = 1 - \frac{P_{cl}^{(n)}(L)}{P_{01}}$$

Using Eq. 2.48 and the relation $\sin^2 X + \cos^2 X = 1$, give:

$$T_{LPG} = 1 - \frac{\sin^2\left[k_{m-01}^{cl-co} L\sqrt{1+\left(\frac{\delta}{k_{m-01}^{cl-co}}\right)^2}\right]}{1+\left(\frac{\delta}{k_{m-01}^{cl-co}}\right)^2}$$

$$= \cos^2\left[k_{m-01}^{cl-co} L\sqrt{1+\left(\frac{\delta}{k_{m-01}^{cl-co}}\right)^2}\right] + \sin^2\left[k_{m-01}^{cl-co} L\sqrt{1+\left(\frac{\delta}{k_{m-01}^{cl-co}}\right)^2}\right]$$

$$- \frac{\sin^2\left[k_{m-01}^{cl-co} L\sqrt{1+\left(\frac{\delta}{k_{m-01}^{cl-co}}\right)^2}\right]}{1+\left(\frac{\delta}{k_{m-01}^{cl-co}}\right)^2}$$

$$= \cos^2\left[k_{m-01}{}^{cl-co} L\sqrt{1+\left(\frac{\delta}{k_{m-01}{}^{cl-co}}\right)^2}\right] + \frac{\delta^2}{(k_{m-01}{}^{cl-co})^2+\delta^2}\sin^2\left[k_{m-01}{}^{cl-co} L\sqrt{1+\left(\frac{\delta}{k_{m-01}{}^{cl-co}}\right)^2}\right] \quad (2.50)$$

Eq. 2.50 can also be re-written in the form [Erdogan 1997a]:

$$T_{LPG} = \cos^2\left[k_{m-01}{}^{cl-co} L\sqrt{1+\left(\frac{\delta}{k_{m-01}{}^{cl-co}}\right)^2}\right] + \frac{1}{1+\left(\frac{k_{m-01}{}^{cl-co}}{\delta}\right)^2}\sin^2\left[k_{m-01}{}^{cl-co} L\sqrt{1+\left(\frac{\delta}{k_{m-01}{}^{cl-co}}\right)^2}\right] \quad (2.51)$$

In order to check whether the MATLAB code used to plot the T_{LPG} is correct, it is necessary to compare the calculated transmission spectrum with those measured experimentally [Erdogan 1997a]. Fig. 2.20 shows the calculated transmission for a relatively weak grating that couples the LP_{01} core mode to the lower-order cladding mode in a standard dispersion-shifted fibre $(\Delta n_{eff} = 0.0042)$. The grating is 50 mm long and has a coupling-length product of $kL = 0.39$. The MATLAB codes used to plot the

long-period grating transmission are given in Appendix 3.4

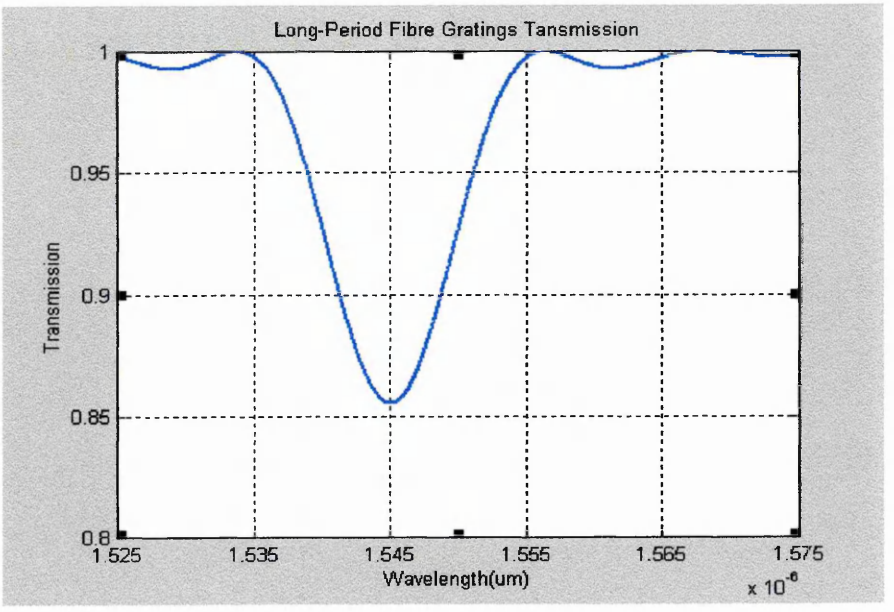

Fig. 2.20. Calculated transmission through a uniform long-period grating.

The results shown in Fig. 2.20 reveal a very good agreement with the experimentally measured values given in Fig. 2.21, suggesting that the code is correct.

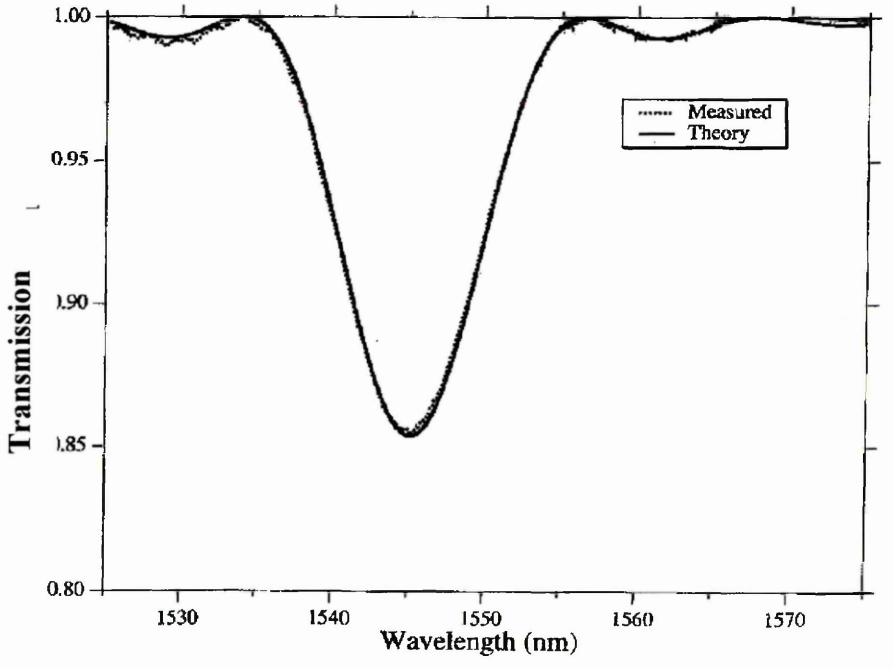

Fig. 2.21. Measured (dotted line) and calculated (solid line) transmission through a uniform cladding-mode transmission grating [Erdogan 1997a].

CHAPTER 3 FIBRE BRAGG GRATING APPLICATIONS

3.1 Introduction

The use of fibre Bragg grating in both sensing and communications applications will be presented in this chapter. Fibre grating sensor applications focus on temperature, strain, index and chemical sensing, while their use in communications applications focuses on fibre amplifiers, dispersion compensation, filters and wavelength division multiplexers / demultiplexers. It is noteworthy that no other single device has had such important applications in both sensing and optical communications fields simultaneously. Section 3.2 deals with FBG in sensor applications while section 3.3 is devoted to Bragg grating in the field of communications.

3.2 Fibre Bragg Grating (FBG) Sensors

FBG sensors are one of the most exciting developments in the field of optical fibre sensors in recent years. The main reason for this is that fibre Bragg grating sensors have a number of distinguished advantages over conventional fibre optic sensors, including potentially low-cost and unique wavelength-multiplexing capacity.

Fig. 3.1 shows a typical reflection spectrum of Bragg grating. The parameters of interest are as follows:

Centre wavelength: 830 nm ± 5.0 nm,

FWHM (full width half maximum): 1 nm ± 0.2 nm

Reflectivity > 90%

Fibre type: York SM800

Refractive index of core 1.45 ± 0.01

Diameters of core and cladding 5/125 μm

Index modulation of grating is typically 0.0008

Length of FBG 1 cm

Period of grating 368 ± 3 nm.

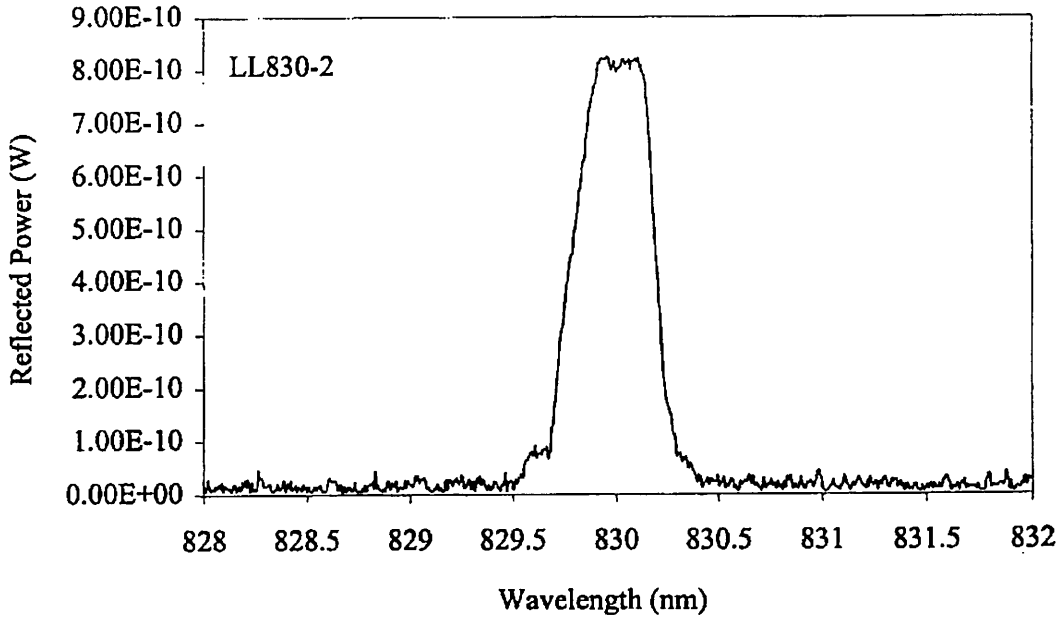

Fig. 3.1. Typical reflection spectrum of Bragg grating.

The Bragg grating resonance, which is the centre wavelength of the back-reflected light from a Bragg grating, depends on the effective index of refraction of the core and the periodicity of the grating. The effective index of refraction, as well as the periodic spacing between the grating planes, will be affected by changes in strain and temperature. The following is a theoretical detail of FBG for temperature and strain sensors.

3.2.1 Fibre Bragg grating temperature sensor

The basic principle of operation commonly used in a fibre Bragg grating-based sensor

system is to monitor the shift in the wavelength of the reflected "Bragg" signal as a result of temperature change. The Bragg wavelength or the resonance condition of a grating is given by:

$$\lambda_B = 2n_{eff}\Lambda \tag{3.1}$$

where n_{eff} is the effective index of refraction in the core and Λ is the grating period. Launching a spectrally broadband source of light into the FBG sensor, results in grating reflecting a narrowband spectral component at the Bragg wavelength. In the transmitted light this spectral component is missing, as depicted in Fig. 3.2.

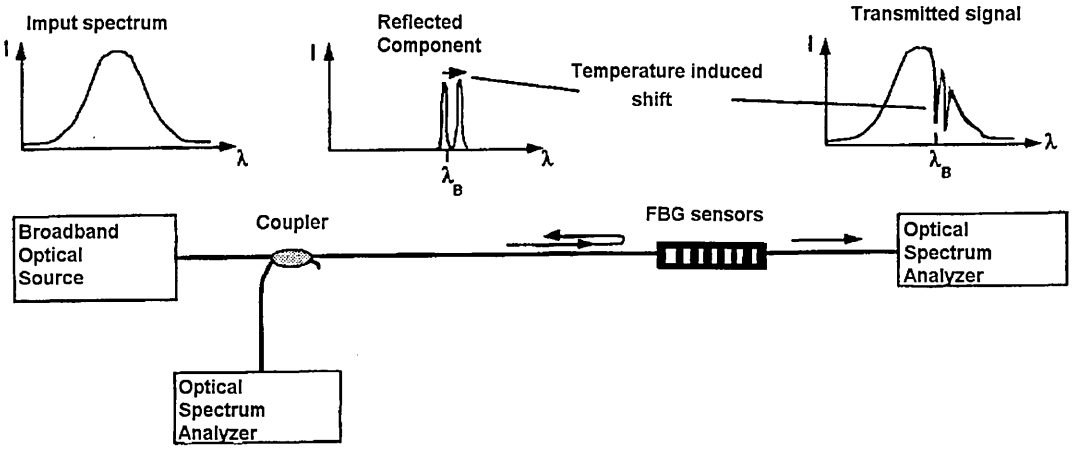

Fig. 3.2. Typical FBG temperature sensor [After Kersey, *et al* 1997],

The bandwidth of the reflected signal, which has typical values between 0.05 - 0.3 nm in most sensor applications, depends on several parameters, in particular the grating length. Perturbation of the grating results in a spectral (Bragg wavelength) shift, which can be detected either in the reflected or transmitted spectrum [Kersey *et al* 1997].

For a temperature change of ΔT, the corresponding wavelength shift $\Delta\lambda_B$ is given by [Rao 1997]:

$$\Delta\lambda_B = \lambda_B(1+\xi)\Delta T \tag{3.2}$$

where ξ is the fibre thermo-optic coefficient. For silica fibres, the wavelength-temperature sensitivities have been measured with a value of about 6.8 pm $^{o}C^{-1}$ for FBGs with 800 nm central wavelength [Morey *et al* 1989], whereas those measured for 1.55 μm FBGs were about 13 pm $^{o}C^{-1}$ [Rao 1995].

The dependence of the Bragg wavelength on temperature can be given by the following detailed expression [Rastogi 1997]:

$$\Delta\lambda_B = \{(d\Lambda/dT)/\Lambda + (dn/dT)/n\}\cdot\lambda_B\Delta T \tag{3.3}$$

The first part of this expression relates to the thermal expansion coefficient of the fibre, and is approximately 0.55×10^{-6} $^{o}C^{-1}$ for silica, whereas the second term, is due to the thermal dependence of the refractive index. The latter represents the thermo-optic coefficient, with an approximate value of 8.6×10^{-6} $^{o}C^{-1}$ for the germania-doped, silica-core fibre, and it accounts for approximately 95% of the observed shift.

Fig. 3.3 shows the shift in wavelength of a 1.3 μm fibre Bragg grating with temperature over a range 5 ^{o}C to 85 ^{o}C. The normalized thermal responsivity at constant strain is gives by:

$$\frac{1}{\lambda_B}\frac{\delta\lambda_B}{\delta T} = 6.67\times10^{-6}\ ^{o}C^{-1} \tag{3.4}$$

A wavelength resolution of about 1 ppm (0.001 nm) is thus required (at a λ_B ~1.3 μm) in order to resolve a temperature change of nearly 0.1 ^{o}C [Kersey 1997].

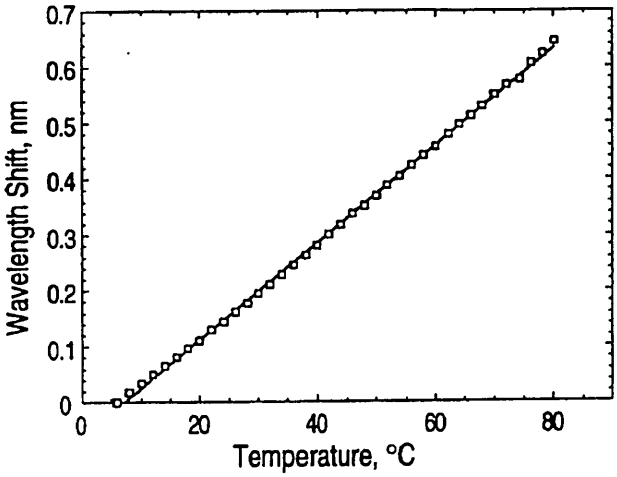

Fig. 3.3. Temperature response of FBG sensor [Rastogi 1997]

3.2.2 Fibre Bragg Grating Strain Sensor

The strain response arises due to both the physical elongation of the sensor (and thus the corresponding fractional change in the grating pitch) and the change in fibre index due to photoelastic effects. The shift in the Bragg wavelength with strain can be expressed by:

$$\Delta\lambda_B = (1 - p_e)\ \varepsilon_z\ \lambda_B \tag{3.5}$$

where ε_z is the applied strain, and p_e is an effective photoelastic coefficient term which is given by

$$p_e = (n_{eff}/2)[P_{12} - \mu(P_{11} + P_{12})] \tag{3.6}$$

where $P_{i,j}$ coefficients are the Pockel's coefficients of the strain-optic tensor, μ is Poisson's ratio and n_{eff} is the effective index of refraction of the core. For a typical germanosilicate optical fibre $P_{11} = 0.113$, $P_{12} = 0.252$, $\mu = 0.16$, and $n_{eff} = 1.482$. The factor p_e has a numerical value of about 0.22 for fused silica. Fig. 3.4 shows the measured strain response of a 1.3 μm FBG.

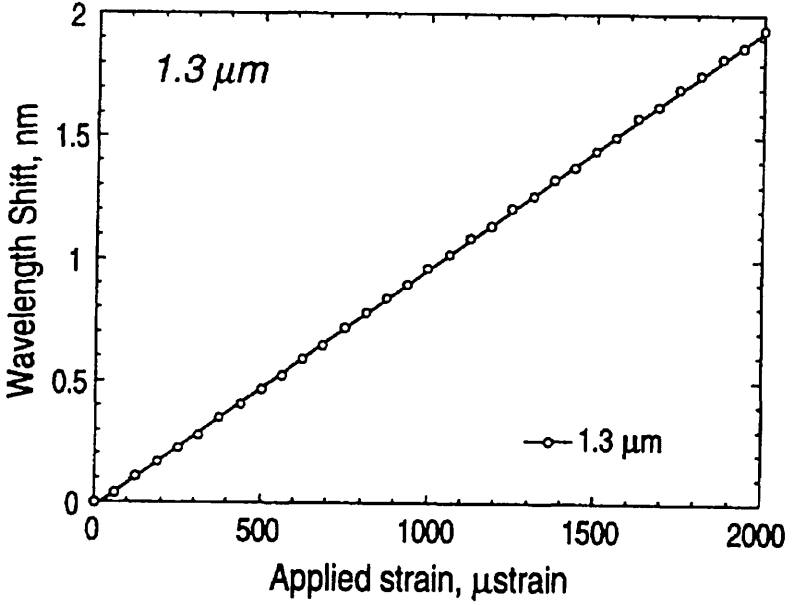

Fig. 3.4. Strain response of FBG sensor [Rastogi 1997].

3.2.3 Fibre Bragg Grating Chemical Sensor

The FBG can be used for chemical sensing based on the fact that the central wavelength of an FBG varies with refractive index change, i.e. chemical concentration change, via the evanescent field interaction between the FBG and the surrounding ambient [Rao 1999]. Meltz and co-workers have written an FBG onto an etched D-shaped fibre by reducing the layer below the flat surface of D fibre from its original thickness of 16 μm to less than 2 μm, and have estimated the cladding layer thickness above the grating to be about 0.5 microns. Using this method it may be possible to resolve a refractive index variation of 5×10^{-6} [Meltz 1996].

The principle of a FBG chemical sensor can be explained as follows:

Any change in the effective refractive index of a propagating mode will cause a corresponding change in the Bragg wavelength. If the evanescent field of the fibre extends beyond the cladding into a superstrate or if the cladding is porous, then it will be sensitive to the refractive index of the material within or around the fibre cladding layer. As long as the mode remains guided, that is, as long as the modified index does

not exceed the core value, then the Bragg spectrum will be shifted and one can measure the refractive index of the superstrate or the modified porous cladding [Meltz 1996].

A new type of fibre grating, the long-period grating has been discovered to be more sensitive to refractive index changes of the material around the grating cladding when compared with FBG 's [Bhatia and Vengsarkar 1996]. More details of index sensors are given in Chapter 4 and Chapter 5.

3.3 Fibre Grating in Communications

FBGs have emerged as important components in a variety of lightwave applications. They have revolutionised the means by which light is processed within the fibre. It is clear that the FBG has opened the way to all-fibre devices in communications. The following are examples of fibre grating application in the field of communications.

3.3.1 Fibre Amplifiers

It is now widely accepted that optical amplifiers have revolutionised the field of optical communications. The most widely used optical amplifiers are erbium-doped fibre amplifiers (EDFAs) which operate in the important third low-loss communication window around 1.5 μm. Fibre photosensitivity and specifically fibre Bragg grating technology has dramatically improved erbium-doped fibre amplifier performance over the past few years, in the areas of pump laser wavelength stabilisation, pump reflectors, and gain wavelength flattening. Fibre Bragg gratings have now established themselves as important devices in the erbium-doped fibre amplifier system.

3.3.1.1 *Erbium Doped Fibre in EDFA*

The EDFA has a fibre segment a few meters long which is heavily doped with ion of the rare earth element erbium (and also co-doped with Al and Ge), and may be excited by a number of optical frequencies 514 nm, 532 nm, 667 nm, 800 nm, 980 nm and 1480 nm. The shortest wavelength, 514 nm excite erbium ions to the highest possible energy level. From this level, they may drop to one of four intermediate metastable levels. From the lowest metastable level, they finally drop to the initial (ground) level, emitting photons of wavelength around 1550 nm. Similar activity takes place with the remaining wavelengths, although the number of metastable levels decreases as the wavelength becomes longer. Finally, the longer wavelength 1480 nm, excites ions to the lowest metastable level from which they drop directly to the ground level. Fig. 3.5 illustrates the two lowest and most important energy excitation and spontaneous emission for erbium. The two convenient excitation wavelengths are 980 nm and 1480 nm. When 980 nm or 1480 nm source propagates through an EDFA fibre, erbium ions are excited and stimulated emission takes place releasing photon energy in the wavelength range 1520 to 1620 nm [after: Kartalopoulos 2000].

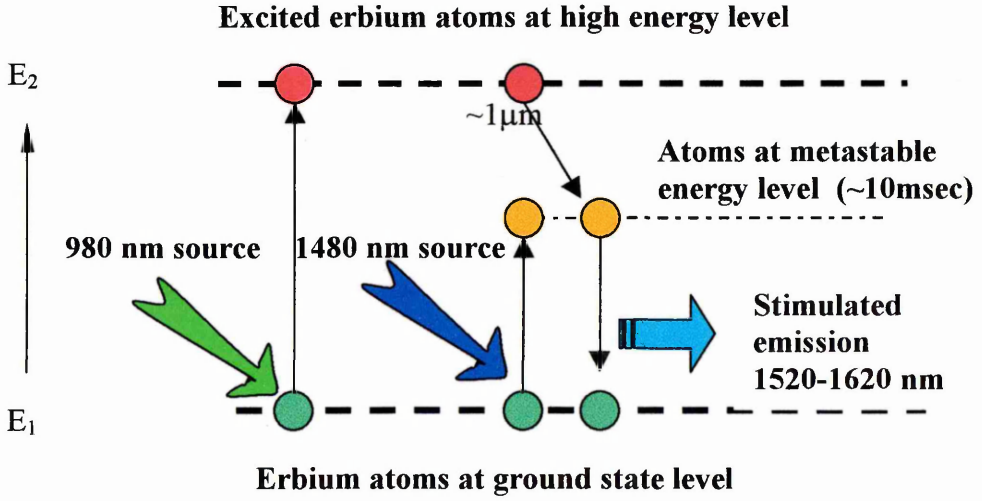

Fig. 3.5. Principle of spontaneous emission of erbium; only the two lower levels are shown.

3.3.1.2 *The Erbium Doped Fibre Amplifiers (EDFAs)*

An EDFA amplifier with integral LPG is constructed from coupling devices, erbium-doped fibre, an LPG and two isolators, etc as shown in Fig. 3.6. The EDFA exhibits the following features, a high gain, low pump power, high saturation power, extremely low polarization sensitivity, low noise and low inter-channel cross talk. They can be used as power amplifiers, in-line amplifiers, as well as pre-amplifiers. EDFAs can provide high gain over a bandwidth as wide as 80 nm and output power as high as +37 dBm. Erbium-doped fibre amplifiers can simultaneously amplify weak light signal at wavelengths across their entire operating range. Fig. 3.6 shows a schematic of such a system. The principle is as follows:

A weak optical signal enter from the left, passing through an optical isolator, which prevents light scattering within the optical amplifier from leading back down the input fibre and potentially generating noise. It then enters a coil of doped fibre, typically several meters long. Light from a pump laser operating at 980 nm or 1480 nm illuminates the doped fibre, exciting erbium atoms along its length. The light signal then stimulates the excited atoms to emit light at the signal wavelength and in phase with the signal. Another optical isolator keeps scattered light from the output fibre from going back into the fibre amplifier.

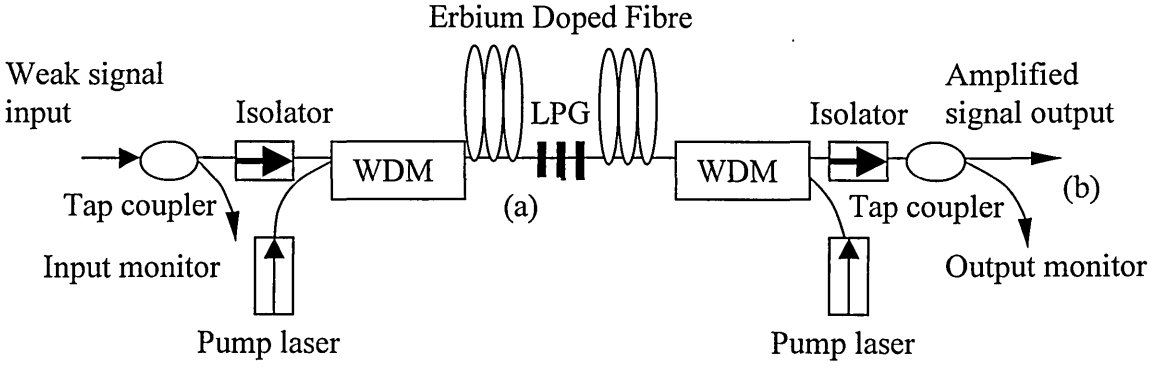

Fig. 3.6. Schematic of typical EDFA with long-period grating gain flattening filter. [after: 1999/2000 Fibre Optic Catalogue, Laser 2000 (UK) Ltd.].

The useful optical bandwidth of the amplified lightwave systems is limited because of the gain-narrowing characteristics of optical amplifiers. Erbium-doped silica fibre amplifiers show gain peaking at 1530 nm and 1560 nm and the useful bandwidth may be reduced to less than 10 nm, see Fig. 3.7(a). In WDM systems the fibre amplifier is carrying multiple wavelengths, and needs some equalisation scheme to maintain a uniform gain at all wavelengths. As a solution, optical filters are added in order to reduce the intensity of the wavelengths that are amplified most strongly.

Significant progress in gain flattening has been achieved using long -period fibre gratings as filters in erbium-doped fibre amplifiers (see Fig. 3.7.(d)). Unlike short-period fibre Bragg grating, long-period fibre gratings work by phase matching the guided-core mode to cladding modes in the fibre, inducing non-reflective loss. The phase matching condition of the long-period grating, $\beta_{co}(\lambda) - \beta^{n}{}_{cl}(\lambda) = 2\pi / \Lambda$, is satisfied for a number of fibre cladding modes, so there are several resonance (Fig.3.7.(b)) in the loss spectrum with 60-100nm spacing. Typical grating pitch and index change in long-period grating equalisers for use in the 1550 nm wavelength region are 400-500 μm and 5×10^{-4}, respectively. Recently, 22dB gain with 1 dB flatness from 1528 to1568 nm has been demonstrated using long-period grating equalisers [Wysocki, 1997]. In another experiment, a 0.2 dB gain ripple over 30nm was achieved [Zyskind 1997]. These results greatly enhance the WDM capacity of amplified lightwave system and may in the future enable practical tera bit per second transmission through a single-mode fibre [Onaka, *et al* 1996].

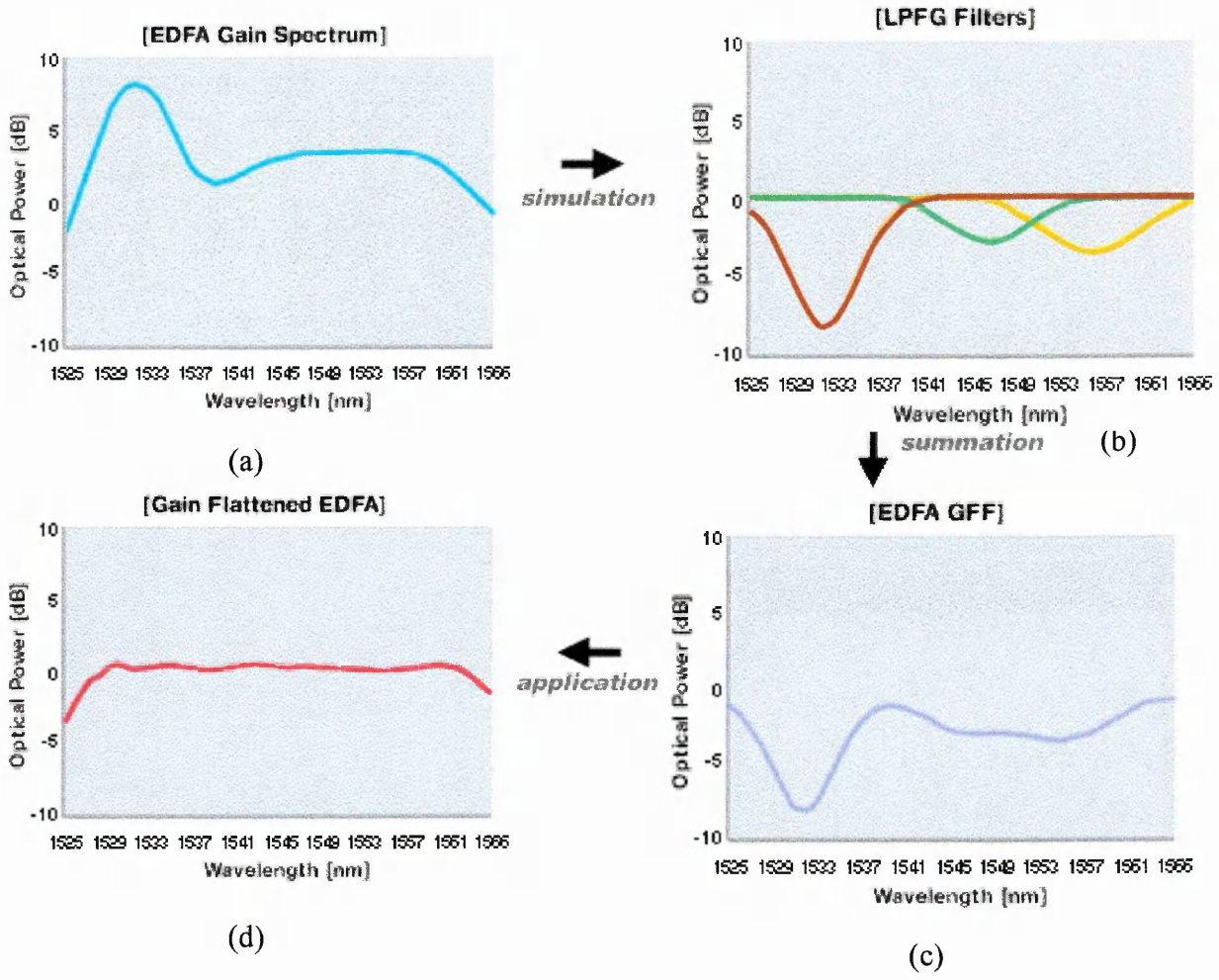

Fig. 3.7. Application of LPG in EDFA gain flattening filter (GFF).
[after: Samsung Electronics Co.,Ltd.,
http://samsungelectronics.com/products/fiberoptics/d31.html].

Fig. 3.7 shows that EDFA BW without LPG gain flattening filter only 10 nm, 1dB flatness is obtained (Fig. 3.7(a)). Adding LPG gain flattening filter to EDFA BW results in 35 nm, 1dB flatness (Fig. 3.7(d)).

3.3.2 Fibre Raman Amplifiers

Recent advances in grating technology and the development of high-power diode pump lasers have revived interest in Raman fibre amplifiers. Raman can provide amplification at both the 1.3 μm and 1.5 μm windows. Raman amplifiers possess many attractive features such as low noise, polarisation insensitive gain, and the ability to achieve

amplification in ordinary germanosilicate transmission fibre. Raman amplifiers have been successfully used as pre-amplifiers, power amplifiers and distributed amplifiers in a number of digital and analogue (single channel/WDM) transmission experiments.

Fibre Raman amplifiers were considered to be the main technology for optical amplification. They may be obtained from a simple cascaded Raman resonator [Grubb 1994]. The linear cavity of the 1300 nm amplifier is shown in Fig. 3.8.

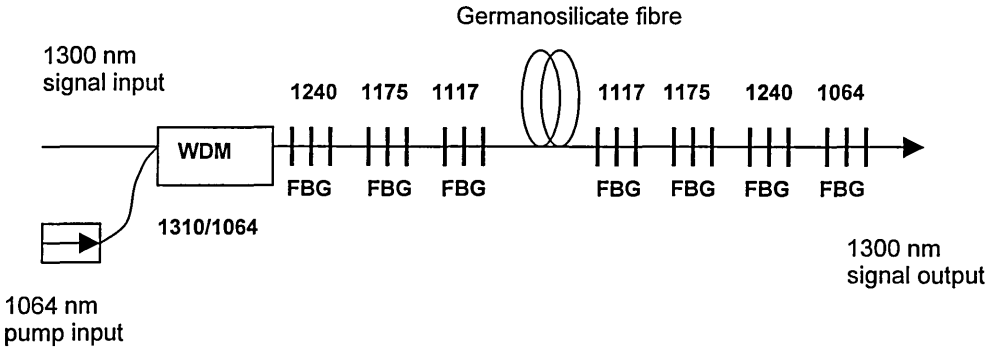

Fig. 3.8. Schematic of 1.3 μm Raman amplifier utilising a series of Bragg gratings as the high reflectors to the various Stokes-lines [After Grubb 1994].

This system uses WDM couplers and a set of gratings to allow gain in the 1300 nm window when pumped by a 1064 nm source. The gain is available at the fourth Stokes wavelength. These amplifiers have gains as high as 40 dB with saturated output powers of 24 dBm. With high germania concentration (higher Raman gain), the pump power can be lowered to 300 mW while providing a gain of 25 dB [Dianov 1995].

A cascaded Raman resonator amplifier system was the first silica fibre-based optical fibre amplifier to be demonstrated at 1300 nm with a gain of 40 dB and an output power of +24 dBm. Fig. 3.8 shows a schematic of such system, where laser light at 1060 nm generated from a high-power cladding-pumped fibre laser is injected into a long length

of germanosilicate fibre. At both ends of the fibre there are highly reflective Bragg gratings, with centre wavelengths at the first three Stokes-lines starting at 1060 nm. This configuration converts the fundamental pump light (1060 nm) efficiently to light at 1240 nm. When a signal at 1300 nm is injected through this structure, it will experience amplification since it is designed to be at the next Stokes Raman shift from the 1240 nm pump light [Othonos Kalli 1999]. The optical spectrum with five Stokes lines is shown in Fig. 3.9.

A Raman amplifier wavelength range from 1.1 to 2.0 μm is possible. Since cladding-pumped laser can be varied by nearly 100 nm, one can efficiently down-convert to virtually any arbitrary wavelength with the use of the appropriate fibre Bragg gratings. Clearly, Bragg gratings are playing an important role in Raman amplifier technology and are having a strong impact in communications lightwave applications [Othonos and Kalli 1999].

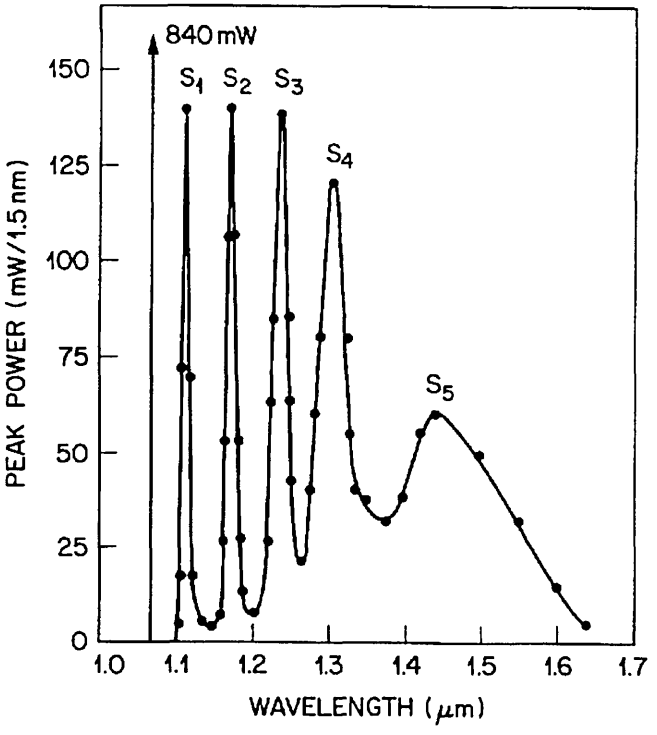

Fig. 3.9. Stimulated Raman scattering (SRS) spectrum showing generation of five Stokes lines S_1 to S_5 by using 1060 nm pump pulses. Vertical line shows the pump output. Peak power was measured though a monochromator with 1.5 nm resolution [After Cohen and Lin 1978].

3.3.3 Chirped Bragg Gratings Compensate for Dispersion

With the advent of long-haul high-capacity systems operating at high speeds, chromatic dispersion effects can be a real problem. Dispersion effects occur as different wavelengths as signal propagate at different speeds along the optical fibre. The problem is exacerbated in high-speed dense wavelength division multiplexing (DWDM) networks because they rely on wavelength in the 1550 nm widow where dispersion is the highest. Dispersion broadens the signal pulse thus increasing the bit-error rate. As network data rates increase, chromatic dispersion in a standard single-mode fibre becomes the main factor limiting performance. At data rates of 2.5 Gbit/s, a signal can be transmitted without significant degradation for distances up to 1000 km, This distance however drops sharply to 60 km at 10 Gbit/s and to a mere 15 km distance at 20 Gbit/s.

In addition, a large portion of the world wide installed base of fibre is of the older variety, optimised for transmission at 1310 nm. Such fibre exhibits high chromatic dispersion of about 17 ps/nm-km when used to transmit at the more commonly used telecom wavelength of 1550 nm, as shown in Fig. 3.10 [Jama 1996].

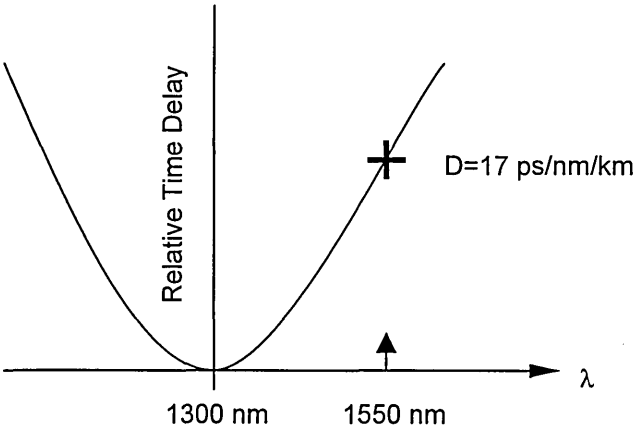

Fig. 3.10. Relative time delay through conventional transmission fibre as a function of wavelength [After Ciles 1997].

Upgrading existing lightwave systems to 10 Gbit/s channels usually requires dispersion compensations often using long lengths of dispersion-compensating fibre [Nuyt, et al 1997]. A severe shortcoming of dispersion-compensating fibre is evident when multiple optically amplified DWDM channels are launched into its small core at an optical amplifier site. Another disadvantage of dispersion-compensating fibre is its high attenuation which is 0.6 dB / km (three times that of non-dispersion-compensating fibre) [Ohn and Donohue, Sep 2000. URL: http://www.e-tek.com/products/articles.htm]. Taking all these issues into account, it becomes necessary to seek other alternative technology for dispersion compensation.

One attractive technology for dispersion compensation is the linearly chirped fibre Bragg grating. Bragg gratings provide dispersion compensation for 1550 nm telecommunications networks without introducing non-linear effects, allowing increased data rates. The grating serves as a selective delay line, which delays the wavelengths that travel faster through the fibre until the other wavelengths catch up. The spacing of the grating is chirped (gratings that have a non-uniform period along their length are therefore known as chirped.), increasing along its length, so it reflects different wavelengths at different points along the fibre. Suppose, for example, that the longer wavelengths in a pulse arrived first and the shorter wavelengths arrived last. We could stack a series of gratings along a fibre with the short period facing the incident light, Then the shorter wavelength λ_{short} reflected at the near end of grating and the longer wavelengths λ_{long} at the far end. Thus, the longer wavelength must travel further within the gratings before they are reflected, thereby experiencing an additional time delay with respect to the shorter wavelength, as shown in Fig. 3.11. Based on this picture one may be write a simple expression for the group delay dispersion of a linear chirped grating of length given as:

$$\tau = \frac{2n_{eff}L_{grating}}{c}, \qquad [ps] \tag{3.7}$$

where n_{eff} is the effective refractive index for the mode propagating in the fibre core and $L_{grating}$ is the length of the grating. The average dispersion D_{ave} of the grating is correlated to the delay τ and the bandwidth of the grating through:

$$D_{ave} = \frac{\tau}{\lambda_{long} - \lambda_{short}} = \frac{\tau}{\Delta\lambda}, \quad [ps/nm] \tag{3.8}$$

where $\Delta\lambda$ is the chirp of the grating and λ_{long} and λ_{short} are the longest and shortest wavelengths respectively imprinted in the grating [Ibsen *et al* 1999].

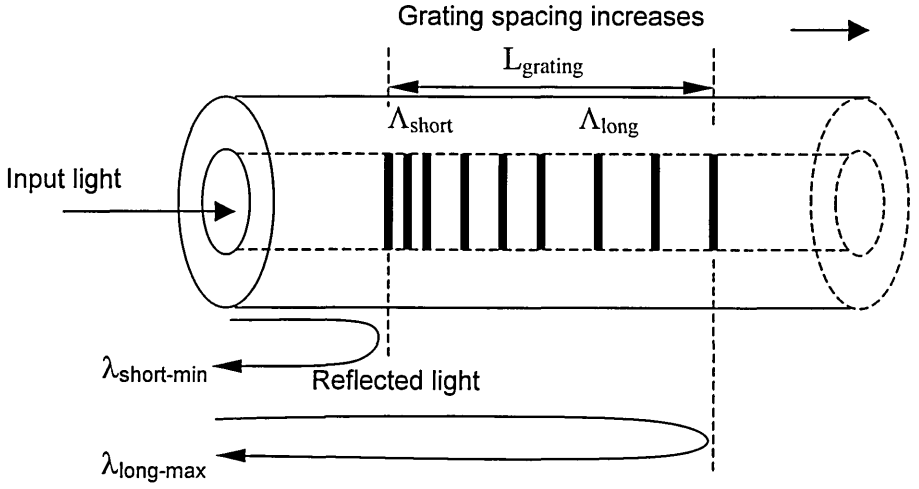

Fig. 3.11. Schematic representation of the principle of dispersion in chirped grating. A series of gratings with different spacing can serve as a delay line to compensate for dispersion.

From Eq. 3.8 it can be seen that the dispersion for a 100 km length of standard fibre with 17 ps/nm km dispersion at 1550 nm may be compensated over a bandwidth of $\Delta\lambda$ = 0.2 nm by linearly chirped grating of approximately 3.5 cm in length [Othonos

and Kalli 1999]

$$(L_{grating} = \frac{c\tau}{2n_{eff}} = \frac{c100D_{ave}\Delta\lambda}{2n_{eff}} = \frac{3\times10^{8+9-12}\times100\times17\times0.2}{2\times1.45} \approx 3.5\times10^{7}\,nm = 3.5cm).$$

The enormous growth rate of data in commercial and domestic networks forces an ever increasing demand for capacity onto the backbone networks. With the recent expansion in line rate to 10 Gbit/s and the realisation of optical amplification, the limitation for information throughput is now dispersion rather than loss. Fibre grating offers an alternative to tens of kilometres of Dispersion Compensating Fibre (DCF) which is a speciality fibre and therefore is more expensive. Nortel's (Northern Telecom) innovative solution is a speciality fibre which has a reflective grating structure written in the core using ultra-violet laser holography. The significance of increasing the grating length to 2.4 metres is that it allows more DWDM channels to be transmitted on the same fibre. This breakthrough was achieved at Nortel's R& D facilities in Harlow. Nortel's longest dispersion compensating grating fibre in the world has given the customers a compact, passive and cost-effective method of maximising the full bandwidth capacity.

The following is an example of a new product for dispersion compensating from E-TEK Dynamics, Inc. Their ITU Fixed Dispersion Compensator with a low group delay ripple and high centre wavelength accuracy, provides an effective solution to chromatic dispersion in most high bit rate DWDM networks.

Typical Performance (E-TEK.com)

Centre Wavelength Range:	1526 nm~1565 nm on ITU grid
Dispersion over:	-0.5 dB bandwidth 200 ps/nm~1700 ps/nm
Insertion Loss:	1.0 dB
Bandwidth:	0.5 nm @1300 ps/nm, 1.0 nm@700 ps/nm

Package Dimensions 220 mm (L) x 18.5 mm (W) x 10 mm (H)

3.3.4 Fibre Grating Band-Pass Filters

Band -pass filters are considered one of the most fundamental devices in multiwavelength optical networking and in most communication systems where wavelength demultiplexing is required. There are several techniques for fabricating these band-pass filters utilising Bragg gratings.

3.3.4.1 Basic Bragg Grating Filter

One of the most basic filters may be constructed by simply splicing or inscribing a fibre grating to a 50:50 (3dB) fibre coupler (Fig. 3.12). This is one of the simplest methods of accessing the narrowband signal reflected by fibre Bragg grating. The disadvantage is obviously that the reflected signal suffers a 6 dB loss by passing through the coupler twice.

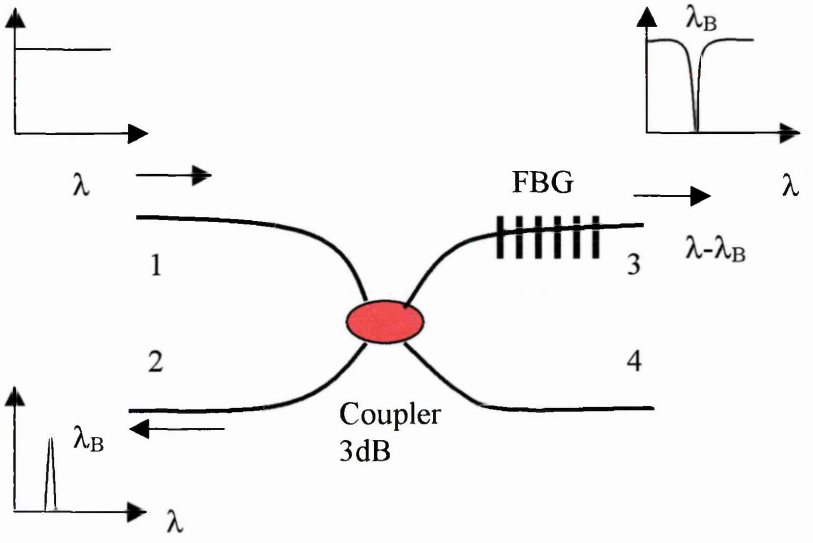

Fig. 3.12. Basic Bragg Gratings Filters showing input (port 1) and output (ports 2 and 3) [After Othonos and Killi 1999].

Moreover, half of the out-of-band signal is also lost and the return loss is only 6 dB. For most systems applications these drawbacks are unacceptable, and more elaborate solutions must therefore be employed.

3.3.4.2 Circulator-Based Filters

Optical circulators are non-reciprocal bulk optics components with multiple input and output ports. Fig. 3.13 shows a high-performance add/drop filter which can be obtained simply by attaching a fibre grating to the second port of a 3-port circulator. With port 1 as the input, the wavelength channel reflected by the grating is transmitted through port 3 while the out-of-band signals are transmitted through the grating on port 2. Commercially available circulators have very high port-to-port isolation (typically 50-60 dB) and thus give the filters excellent wavelength isolation and return loss. However, circulators are very expensive and have high insertion losses (1-2 dB port to port), which would make an all-fibre solution more suitable in many applications [Othonos and Killi1999].

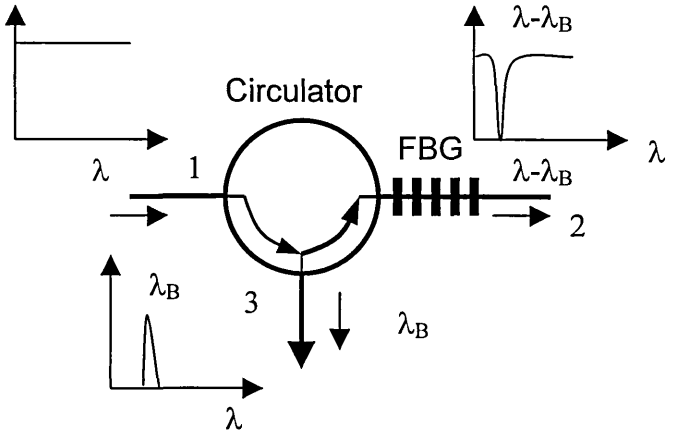

Fig. 3.13. Circulator-based filter

3.3.4.3 Add/Drop Multiplexer Based on Bragg Gratings in Twin-Core Fibre Mach-Zehnder Interferometer

One of the key components in new multi-channel telecom systems is an optical add/drop multiplexer. To minimize the balance requirements of a Mach-Zehnder interferometer in the add/drop multiplexers, a twin-core fibre based system has been proposed and demonstrated [Bethuys 1998]. A specially designed twin-core fibre, where each core has the specifications of standard single mode fibre, has been developed. Two identical fibre Bragg gratings and two couplers arranged in Mach-Zehnder configuration are constructed into the twin core fibre, as shown in Fig. 3.14. The principle is such that light is launched at the input ports and splits equally between the two arms of the twin core fibre section. The Bragg gratings reflect a specified wavelength channel. The reflected wavelength recombines and exits as a dropped channel. From symmetry considerations, the added function must also require the same condition. An add channel enters through the add port, splits equally, reflects off the grating, recombines and joins the remaining wavelengths through the output.

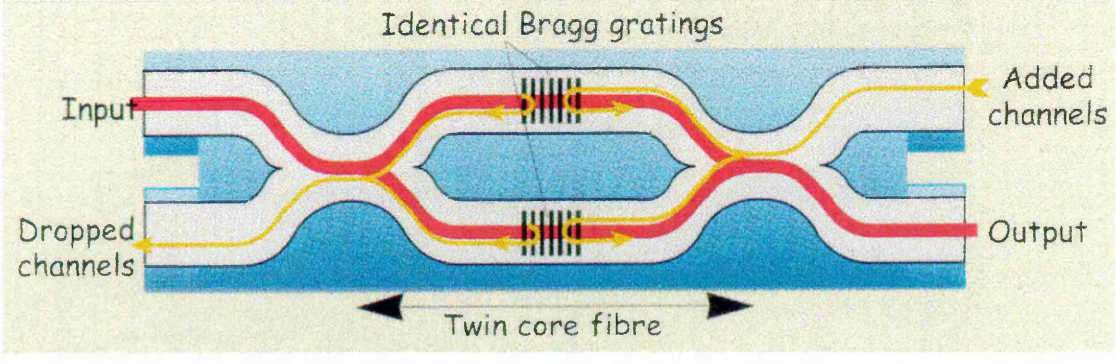

Fig. 3.14. Schematic of the Add/Drop multiplexer based on Bragg gratings in Twin-core fibre Mach-Zehnder interferometer [1999/2000 Fibre Optic Catalogue, Laser 2000 Ltd.UK].

The cladding-mode coupling losses for each passed channel were measured to be under 0.3 dB. At the Bragg wavelength, extinction was near 29 dB and 0.8 nm, and the bandwidth was measured at 20 dB in the transmitted spectrum. Furthermore, isolation between the add and the output ports at the Bragg wavelength was measured to be at least 30 dB. Several of these new twin core systems can be cascaded (one for each wavelength) to form a complete DWDM system. So this kind add/drop multiplexer may play an important role in communications networks.

3.3.5 Fibre Bragg Gratings Applications in Dense Wavelength Division Multiplexer (DWDM) Systems

The hybrid DWDM device combines fibre Bragg gratings and dielectric-coated band-pass filters and can meet the required specification in various cost-effective structures. Fig. 3.15 is an example of a hybrid demultiplexer.

An eight-wavelength optical input signal passes through an isolator to a 3-dB coupler and is split into two equal output arms. Each of the output arms has four apodized fibre Bragg gratings for a 0.4 nm channel spacing with a high reflectivity to block the optical signals at the four alternative wavelengths. The same structures can be used to extend DWDM multiplexers and demultiplexer from 8 channels to 16, 32, or 64, by proportionally adding more fibre Bragg gratings on the two arms of the 3-dB fibre coupler and on port 2 of the two optical circulators.

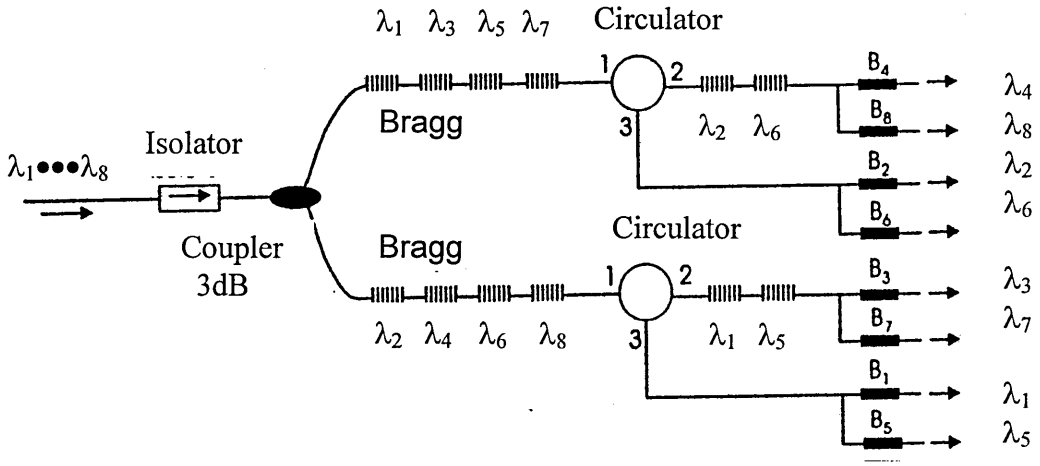

Fig. 3.15. Hybrid dense wavelength division demultiplexer, each with a channel spacing of 0.4 nm. The system is constructed by incorporating fibre Bragg gratings and dielectric-coated band-pass filters [Othonos and Kalli 1999].

4.1 Introduction

Long-period gratings were first presented by Vengsarkar and co-workers in1996 as band-rejection filters [Vengsarkar 1996a], and later as gain equalizers of Erbium-doped fibre amplifiers (EDFA) [Vengsarkar 1996b, 1996c]. At the same time, they showed that the coupling wavelengths shift with the external refractive index change [Bhatia 1996]. Since then many other authors have reported that the LPG has been used as novel fibre sensors in the temperature, strain and refractive index sensing field [Kersey 1997, Patrick 1998]. The LPG can also be used for structural analysis and control [Vries, *et al* 1998], biosensors [Zhang 1999] and recently Bhatia has shown that the LPG can be used as a multi-parameter sensor [Bhatia 1999]. This chapter gives a review of temperature, strain and index sensors and the development of a model for an index sensor and chemical gas sensor.

Long-period fibre gratings are photo-induced fibre devices with the period of the order of hundreds of micrometers as shown in Fig. 4.1.

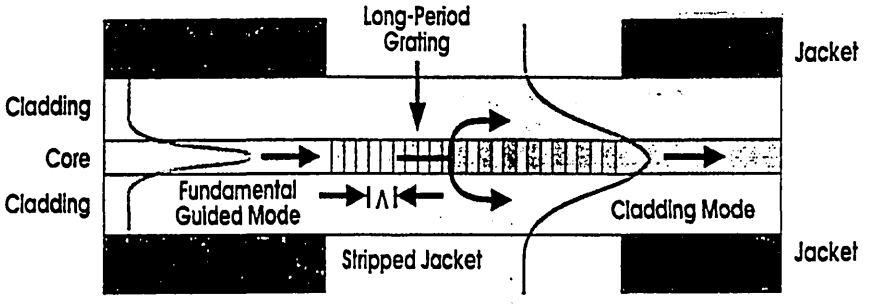

Fig. 4.1. Coupling of the fundamental guided mode to cladding modes in an LPG. Λ is the periodicity of the refractive index modulation in the fibre core. [Tolpegin 1997]

For a single-mode fibre, when a broad band light passed through the LPG, narrow light bands centred at given wavelength are coupled into the fibre cladding. These cladding modes decay rapidly as they propagate along the fibre owing to the lossy cladding coating interface. The wavelengths at which the coupling from the guided fundamental mode to the cladding modes occur are dependent on the periodicity Λ and the photo-induced index change Δn of the grating, according to the following phase matching condition [Vengsarkar 1996]:

$$\beta_{core} - \beta^{(n)}{}_{clad} = \frac{2\pi}{\Lambda} \tag{4.1}$$

Where β_{core} denoted the propagation constant of the fundamental mode in the fibre core, and $\beta^{(n)}{}_{clad}$ denotes the propagation constant of the n^{th} cladding mode of the fibre cladding. Considering the relation of $\beta = 2\pi n_{eff} / \lambda$, where n_{eff} is the effective index of the mode, Eq. 4.1 can be represented using the effective indices of the corresponding modes as [after: Patrik 1998]:

$$\lambda^{(n)}{}_i = \left(n_{core}(\lambda_i) - n_{clad}{}^{(n)}(\lambda_i)\right)\Lambda \tag{4.2}$$

where $\lambda^{(n)}{}_i$ is the n^{th} coupling wavelength, $n_{core}(\lambda_i)$ is the effective index of the core, $n_{clad}{}^{(n)}(\lambda_i)$ is the effective index of the n^{th} cladding mode and Λ is the period of the LPG. Fig. 4.2 shows a typical LPG spectrum, which is measured using an HP 70951B Optical Spectrum Analyzer. The peak absorption occurs at $\lambda = 1.371807$ μm. It shows the phase matching between the guided core mode and 10^{th} forward propagating cladding mode.

The specifications of the LPG fibre used are listed in Table 4.1.

Table 4.1: CIII Boron (not hydrogenated) LPG fibre specifications

Parameter	Value
Core index n_1	1.458
Cladding index n_2	1.455
Core radius	2.625 μm
Cladding radius	62.5 μm
Pitch of the grating	325 μm
Index modulation	1.295×10^{-4}
Length of LPG	5 cm

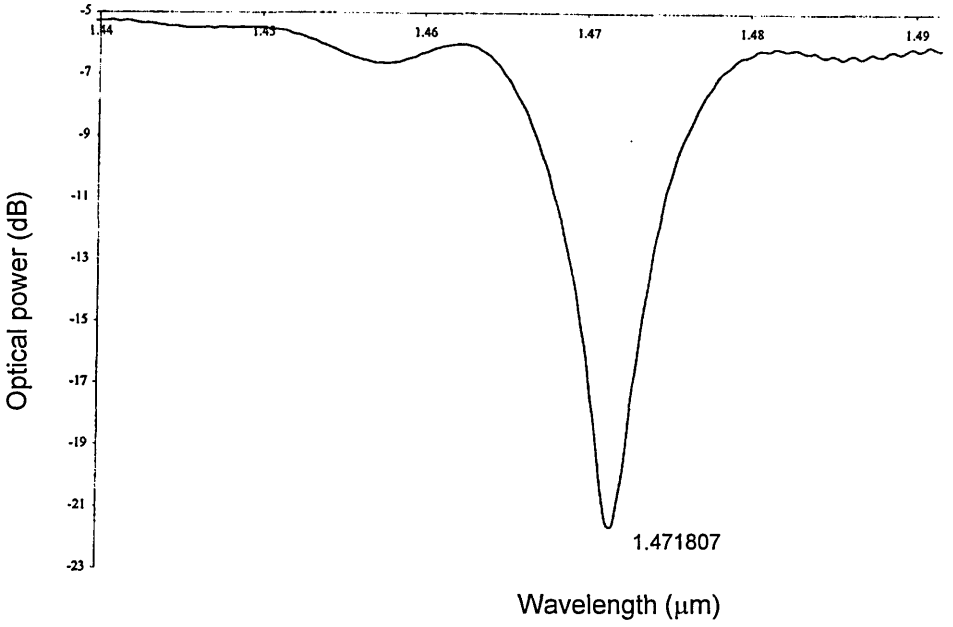

Fig. 4.2 Typical transmission of

4.2. Temperature Sensor

The sensitivity of a long-period grating to temperature can be examined by expanding Eq. 4.2 to yield [Bhatia 1999]:

$$\frac{d\lambda}{dT} = \frac{d\lambda}{d(\delta n_{eff})}\left(\frac{dn_{eff}}{dT} - \frac{dn_{cl}}{dT}\right) + \Lambda\frac{d\lambda}{d\Lambda}\frac{1}{L}\frac{dL}{dT} \tag{4.3}$$

where L is the length of the grating, $dn_{eff} = n_{core} - n_{clad}$ is the differential effective index, and the ordinal m has been dropped for the sake of simplicity.

The two terms on the right hand side of Eq. 4.3 separated by the + sign represent the contributions to the thermal sensitivity of the grating due to the change in the

differential effective index and the grating periodicity, and will henceforth be referred to as the material and waveguide effects, respectively [Bhatia 1996]. The material contribution arises from the change in the indices of refraction of the core and the cladding due to temperature and is a function of the composition of the fibre. The waveguide contribution has its basis in the thermal sensitivity of the grating periodicity and can be negative or positive depending strongly on the slope $d\lambda / d\Lambda$ of the characteristic curve corresponding to the appropriate cladding mode. The wavelength shift due to the material effect can similarly have either polarity and its magnitude is a function of the relative change between the effective indices of the guided and cladding modes. For a standard long-period grating with periodicity of hundreds of micrometers, the material effect typically dominates the waveguide contribution to the temperature - induced shift [Bhatia 1999].

Bhatia [Bhatia and Vengsarkar 1996] showed that the temperature response of LPG can be either positive or negative: with a negative temperature response as low as -0.2 nm $^{o}C^{-1}$ and a positive response reaching +0.15 nm $^{o}C^{-1}$.

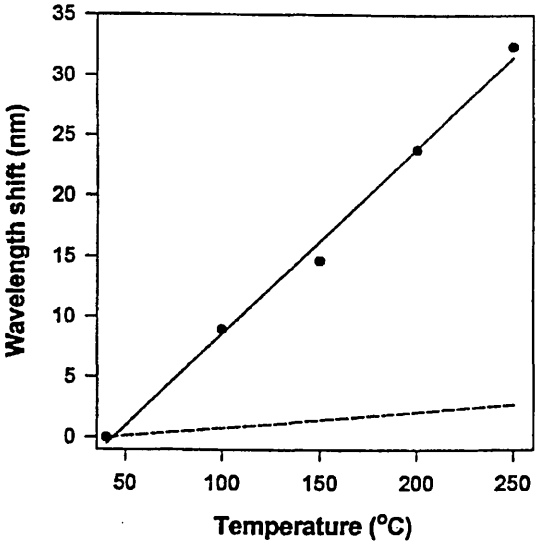

Fig. 4.3. Shift in third-order coupling band width temperature for a long-period grating in 980 nm single-mode fibre (•) and for a conventional Bragg grating (dashed line) [Bhatia and Vengsarkar 1996].

Figure 4.3 shows that the long-period grating temperature sensor is more sensitive than the Bragg gating sensor. This can be seen in the hybrid fibre Bragg grating /long period fibre grating sensor which is presented by Patrick and co-workers in which they use hybrid fibre Bragg grating /long-period fibre grating sensor for simultaneous strain and temperature measurement. They have shown that the LPG wavelength shifts for strain and temperature were 0.5 pm /με and 60 pm/^{o}C, compared with 1 pm/με and 9pm/^{o}C, give a well-conditioned transformation and resulting in strain and temperature errors of ±9με and ±1.5^{o}C, respectively [Patrick *et al* 1996].

The Long period grating has rather different temperature and strain response coefficient compared with the Bragg grating. This is because the Bragg grating wavelength is linearly proportional to the grating period, which is multiplied by the effective refractive index of the core. Whereas the long period grating wavelength is proportional to the grating period multiplied by difference in index of refraction between the core and the cladding [Othonos and Kalli 1999].

4.3. Axial Strain Sensor

The sensitivity of a long-period grating to axial strain ε can be studied by expanding Eq. 4.2 and re-arranging to yield [Bhatia 1999]:

$$\frac{d\lambda}{d\varepsilon} = \frac{d\lambda}{d(\delta n_{eff})}\left(\frac{dn_{eff}}{d\varepsilon} - \frac{dn_{cl}}{d\varepsilon}\right) + \Lambda\frac{d\lambda}{d\Lambda} \tag{4.4}$$

where the two term on the right hand side can again be divided into material (first term) and waveguide (second term) contributions. In this case the two contributions can have either polarity depending on the grating period and the order of the cladding mode. The waveguide effect can be significant and is a function of the local slope $d\lambda / d\Lambda$ for a

particular cladding mode [Bhatia 1996]. Moreover, the two contributions can be equal in magnitude but opposite in polarity, resulting in a strain-insensitive grating that can be employed as a pure temperature sensor [Bhatia *et al* 1997].

Long period grating strain sensor is found to be more sensitive than Bragg grating strain sensor. Fig. 4.4 shows that long period grating has a strain coefficient of $15.21 nm/\%\varepsilon$, which is almost twice that of Bragg grating at the same wavelength $8.3 nm/\%\varepsilon$.

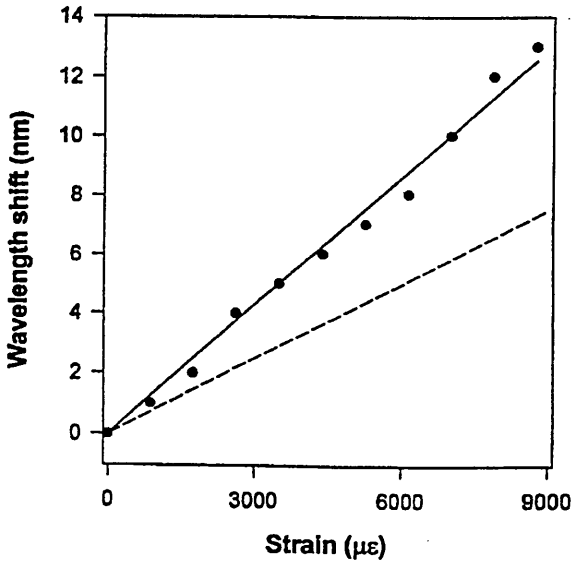

Fig. 4.4. Shift in the fourth-order coupling band with axial strain for long-period grating in fibre (type Corning FLEXCOR) (solid circles) and a Bragg grating fibre (dashed line) [Bhatia and Vengsarkar 1996].

4.4. Index of Refraction Sensor

Fibre Bragg gratings have previously been proposed as refractive index sensors for chemical analysis by etching the cladding of the fibre to within a few micrometers of the core, as introduced in Chapter 3 "Fibre Bragg gratings chemical sensors". The etching of the cladding reduces the strength of the fibre and makes it susceptible to damage under harsh environmental conditions [Bhatia 1996].

It is clear that effective indices of cladding modes are strong function of the surrounding index n_3. Any change in the surrounding refractive index will modulate the propagation constants of cladding modes $\beta^{(n)}{}_{clad}$ and the effective refractive indices of the cladding modes $n_{clad}{}^{(n)}(\lambda_i)$.

From Eq. 4.2 it can be seen that when $n_{clad}{}^{(n)}(\lambda_i)$ changes, the coupling wavelength $\lambda^{(n)}{}_i$ will shift. This is the fundamental theory of the long-period grating index sensor.

The LPG index sensor was first presented by Bhatia [Bhatia and Vengsarkar 1996], who showed that when the surrounding index changes, an LPG shift of 62.4 nm and an average resolution of 7.69×10^{-5} is possible in the 1.404-1.452 index range, as shown in Fig. 4.5.

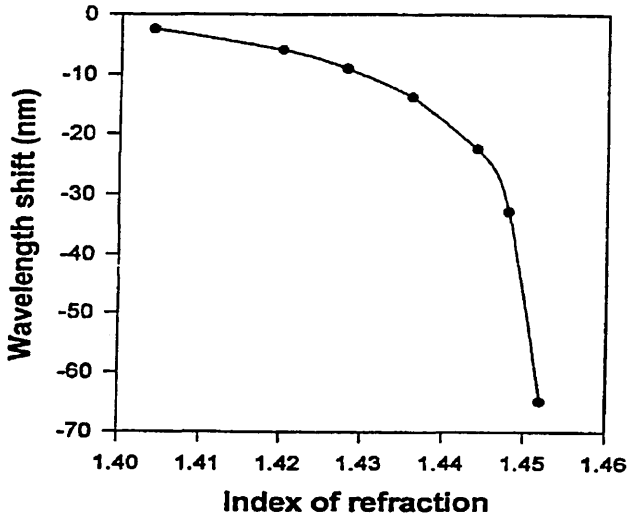

Fig. 4.5. The wavelength shift in the fifth-order coupling band with refractive index of ambient material for a grating in Corning standard 1310 nm fibre. The shift is with reference to the spectral position with air as the surrounding medium.

Patrick and co-workers [Patrick *et al* 1998] have demonstrated the change in coupling wavelength of a long-period grating attenuation band with changes in external

index of refraction, experimentally investigating the spectral response from $n_3 = 1$ to $n_3 = 1.72$. Coupling to seven distinct cladding modes can be seen in the Fig. 4.6. The wavelengths of the attenuation bands at $n_3 = 1$ are indicated by the dotted lines.

As the external index was increased from $n_3 = 1$ to $n_3 = 1.44$, the principle effect was a blue-shift of the centre wavelength of the bands, which was particularly pronounced in the longest wavelength bands. Between $n_3 = 1.45$ and $n_3 = 1.46$, an abrupt change in the spectrum characteristic was observed. At this point the cladding modes would be expected to no longer be discrete guided modes, and the coupling spectrum spreads and the coupling almost disappears for the higher order modes. For $n_3 > 1.46$ coupling to cladding modes structure re-appears, with the highest order bands increasing in strength with increasing index. The shortest wavelength coupling bands remain visible over the full range of indices [Patrick *et al* 1998].

If the surrounding index is higher than the cladding index, $n_3 > n_{clad}$, the propagation constant of the cladding mode becomes complex and the mode becomes a leaky mode. Detailed discussion can be found in Section 5.3 "Modelling of Long-Period Grating Index Sensors".

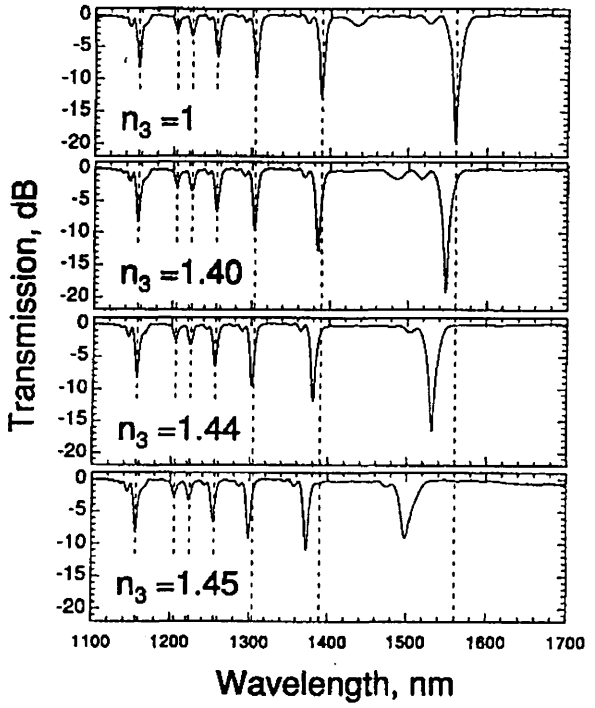

(a)

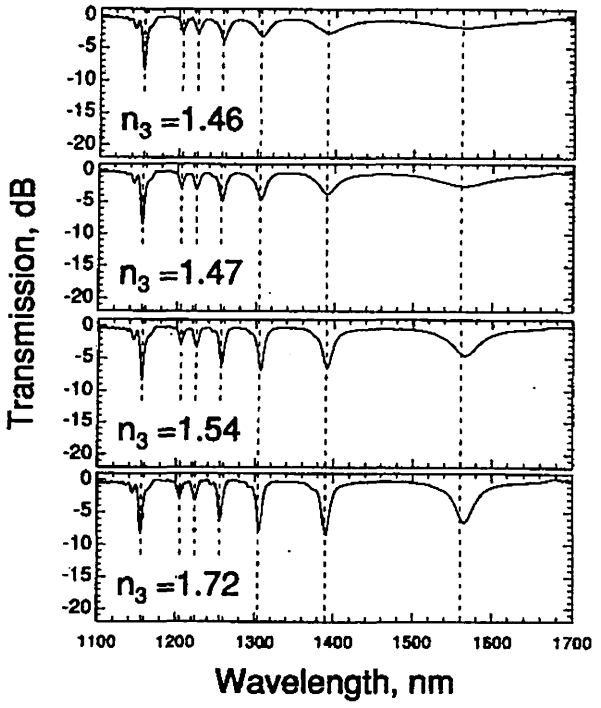

Fig. 4.6. (a) Broad-band transmission spectrum of $\Lambda = 275$ μm LPG for n_3 ranging from $n_3 = 1$ to $n_3 = 1.45$. (b) Broad-band transmission spectrum of $\Lambda = 275$ μm LPG for n_3 ranging from $n_3 = 1.46$ to $n_3 = 1.72$.dotted lines indicate attenuation band wavelength at $n_3 = 1$[Patrick, *et al* 1998].

CHAPTER 5 MATHEMATICAL MODELLING OF LONG-PERIOD GRATING SENSORS

5.1 Foundation of Theory

The concept of a "mode" is the most basic one in the wave theory of optical fibre, and it is also the foundation of the modelling of LPG sensors. This section will provide derivations of the core mode and cladding modes, closely following the work by Okoshi [Okoshi 1982] and Davis [Davis 1996].

5.1.1 Wave Equations in Cartesian Coordinates

When considering an electromagnetic wave having angular frequency ω and propagating in the z direction with phase constant β, the electric and magnetic field can be expressed as:

$$\mathbf{E} = \mathrm{Re}\{ E_0(x,y)\exp[i(\omega t-\beta z)] \}, \tag{5.1}$$

$$\mathbf{H} = \mathrm{Re}\{ H_0(x,y)\exp[i(\omega t-\beta z)] \}, \tag{5.2}$$

where **E** is the electric field,

H is the magnetic field,

β is the propagation constant,

For the Cartesian components of E_0 and H_0, Maxwell's equations are:

$$\mathrm{Curl}\ \mathbf{E} = -i\omega\mu\,\mathbf{H}, \tag{5.3}$$

$$\mathrm{Curl}\ \mathbf{H} = i\omega\mu\,\mathbf{E}, \tag{5.4}$$

Eq. 5.3 becomes:

$$\text{Curl } \mathbf{E} = \nabla \times \mathbf{E} = \begin{vmatrix} \bar{x} & \bar{y} & \bar{z} \\ \partial/\partial x & \partial/\partial y & \partial/\partial z \\ E_x & E_y & E_z \end{vmatrix}$$

$$\text{Curl } \mathbf{E} = \left(\frac{\partial E_z}{\partial y} - \frac{\partial E_y}{\partial z}\right)\bar{x} + \left(\frac{\partial E_x}{\partial z} - \frac{\partial E_z}{\partial x}\right)\bar{y} + \left(\frac{\partial E_y}{\partial x} - \frac{\partial E_x}{\partial y}\right)\bar{z}$$

$$= -i\omega\mu H_x \bar{x} \; -i\omega\mu H_y \bar{y} \; -i\omega\mu H_z \bar{z}\,, \tag{5.5}$$

Since the two sides of the equation are the same, the vector component values are same, thus:

$$\frac{\partial E_z}{\partial y} - \frac{\partial E_y}{\partial z} = -i\omega\mu H_x, \tag{5.6}$$

$$\frac{\partial E_x}{\partial z} - \frac{\partial E_z}{\partial x} = -\mathrm{i}\omega\mu H_y, \tag{5.7}$$

$$\frac{\partial E_y}{\partial x} - \frac{\partial E_x}{\partial y} = -i\omega\mu H_z, \tag{5.8}$$

Eq. 5.1 shows that z dependence on E_y is $\exp[\mathrm{i}(\omega t - \beta z)]$, if not omitted this gives:

$$\frac{\partial E_y}{\partial z} = \frac{\partial E_y \exp[\mathrm{i}(\omega t - \beta z)]}{\partial z} = \frac{E_y \partial \exp[\mathrm{i}(\omega t - \beta z)]}{\partial z} = -i\beta E_y$$

Substituting $-i\beta E_y$ into Eq. 5.6 yields:

$$\frac{\partial E_z}{\partial y} - (-i\beta E_y) = -\mathrm{i}\omega\mu H_x$$

$$\therefore \; \frac{\partial E_z}{\partial y} + i\beta E_y = -\mathrm{i}\omega\mu H_x\,, \tag{5.9}$$

Similarly $\dfrac{\partial E_x}{\partial z} = \dfrac{\partial E_x \exp[\mathrm{i}(\omega t - \beta z)]}{\partial z} = -\beta E_x$

Substitute $-\beta E_x$ into Eq. 5.7 yields:

$$\therefore i\beta E_x + \frac{\partial E_z}{\partial x} = \mathrm{i}\omega\mu H_y, \tag{5.10}$$

Using the same method Eq. 5.4 gives:

$$\frac{\partial H_z}{\partial y} + i\beta H_y = \mathrm{i}\omega\varepsilon E_x, \tag{5.11}$$

$$-i\beta H_x - \frac{\partial H_z}{\partial x} = \mathrm{i}\omega\varepsilon E_y, \tag{5.12}$$

$$\frac{\partial H_y}{\partial x} - \frac{\partial H_x}{\partial y} = \mathrm{i}\omega\varepsilon E_z \tag{5.13}$$

Using Eqs. 5.9, 5.10, 5.11, and 5.12 components E_x, E_y, H_x and H_y can all be expressed in terms of E_z and H_z as follows:

From Eq. 5.10 we get:

$$H_y = (\frac{\partial Ez}{\partial x} + i\beta E_z)/(i\omega\mu) \tag{5.14}$$

Substituting Eq. 5.14 into Eq. 5.11 gives

$$\frac{\partial H_z}{\partial y} + i\beta(\frac{\partial \mathrm{E}z}{\partial \mathrm{x}} + \mathrm{i}\beta E_z)/(\mathrm{i}\omega\mu) = i\omega\varepsilon \mathrm{E}_x,$$

$$\frac{\partial H_z}{\partial y} + \frac{\beta}{\omega\mu}\frac{\partial \mathrm{E}z}{\partial \mathrm{x}} = i\omega\varepsilon \mathrm{E}_x - \mathrm{i}\frac{\beta^2}{\omega\mu}E_x, \text{two side multiplied by } \omega\mu, \text{ using } \varepsilon = \varepsilon_0 n^2,$$

give:

$$\omega\mu\frac{\partial H_z}{\partial y} + \beta\frac{\partial \mathrm{E}z}{\partial \mathrm{x}} = i\omega^2\mu_0\varepsilon E_x - i\beta^2 E_x$$
$$= i(\omega^2\mu_0\varepsilon - \beta^2)E_x = i(\omega^2\mu_0\varepsilon_0 n^2 - \beta^2)E_x$$

$$E_x = \frac{1}{i(\omega^2\mu_0\varepsilon_0 n^2 - \beta^2)}(\beta\frac{\partial E_z}{\partial x} + \omega\mu\frac{\partial H_z}{\partial y}) = \frac{1}{i(k^2 n^2 - \beta^2)}(\beta\frac{\partial E_z}{\partial x} + \omega\mu\frac{\partial H_z}{\partial y}),$$

$$E_x = -\frac{i}{\beta_t^{\,2}}(\beta\frac{\partial E_z}{\partial x} + \omega\mu\frac{\partial H_z}{\partial y}) \tag{5.15}$$

In the same manner:

$$E_y = -\frac{i}{\beta_t^{\,2}}(\beta\frac{\partial Ez}{\partial y} - \omega\mu\frac{\partial Hz}{\partial x}), \tag{5.16}$$

$$H_x = -\frac{i}{\beta_t^{\,2}}(\beta\frac{\partial Hz}{\partial x} - \omega\varepsilon\frac{\partial E_z}{\partial y}), \tag{5.17}$$

$$H_y = -\frac{i}{\beta_t^2}\left(\beta\frac{\partial H_x}{\partial y} + \omega\varepsilon\frac{\partial E_z}{\partial x}\right), \tag{5.18}$$

where

$$\beta_t^2 = k^2 n^2 - \beta^2 \tag{5.19}$$

$$k^2 = \omega^2\varepsilon_0\mu_0, \tag{5.20}$$

and n denotes the refractive index of the medium. The parameter β_t is called the transverse phase constant or transverse wave number.

Substituting Eqs. 5.17 and 5.16 into Eq. 5.13, results in:

$$\frac{\partial H_y}{\partial x} - \frac{\partial H_x}{\partial y} = \frac{\partial}{\partial x}\left(-\frac{i}{\beta_t^2}\left(\beta\frac{\partial Hz}{\partial y} + \omega\varepsilon\frac{\partial E_z}{\partial x}\right)\right) - \frac{\partial}{\partial y}\left(-\frac{i}{\beta_t^2}\left(\beta\frac{\partial H_z}{\partial x} - \omega\varepsilon\frac{\partial E_z}{\partial y}\right)\right)$$

$$= i\omega\varepsilon E_z,$$

$$-\frac{i\beta}{\beta_t^2}\frac{\partial^2 H_z}{\partial x\partial y} - \frac{i}{\beta_t^2}\omega\varepsilon\frac{\partial^2 E_z}{\partial x^2} + \frac{i\beta}{\beta_t^2}\frac{\partial^2 H_z}{\partial x\partial y} - \frac{i}{\beta^2}\omega\varepsilon\frac{\partial^2 E_z}{\partial y^2} = i\omega\varepsilon E_z,$$

$$-\frac{i}{\beta_t^2}\omega\varepsilon\frac{\partial^2 E_z}{\partial x^2} - \frac{i}{\beta_t^2}\omega\varepsilon\frac{\partial^2 E_z}{\partial y^2} = i\omega\varepsilon E_z$$

$$\frac{\partial^2 E_z}{\partial x^2} + \frac{\partial^2 E_z}{\partial y^2} + \beta_t E_z = 0 \tag{5.21}$$

and substituting Eqs. 5.15 and 5.16 into Eq. 5.8 gives:

$$\frac{\partial^2 H_z}{\partial x^2} + \frac{\partial^2 H_z}{\partial y^2} + \beta_t H_z = 0 \tag{5.22}$$

5.1.2 Wave Equation in Cylindrical Coordinates

For the analysis of wave propagation in an optical fibre, which is axially symmetric, the wave equations are rewritten in terms of cylindrical coordinates.

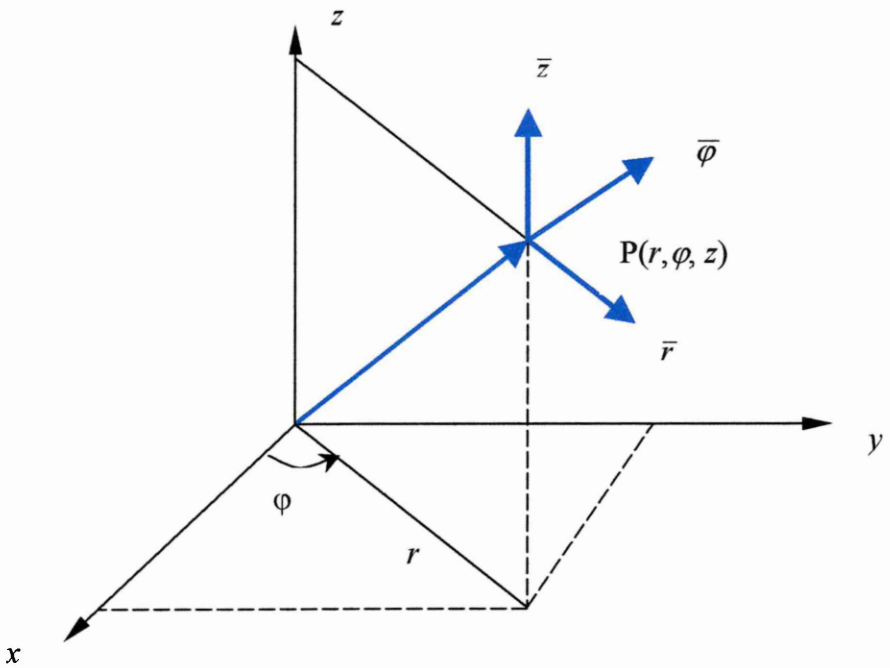

Fig. 5.1. Definition of cylindrical coordinates

The basic relations between the cylindrical and rectangular coordinates are [Wangsness 1979]:

$$x = r\cos\varphi\,, \tag{5.23}$$

$$y = r\sin\varphi, \tag{5.24}$$

$$z = z, \tag{5.25}$$

$$r = (x^2 + y^2)^{1/2}, \tag{5.26}$$

$$\tan\varphi = y/x, \tag{5.27}$$

$$E_r = E_x\cos\varphi + E_y\sin\varphi, \tag{5.28}$$

$$E_\varphi = -E_x\sin\varphi + E_y\cos\varphi, \tag{5.29}$$

From above relations we obtain:

$$\frac{\partial E_z}{\partial x} = \frac{\partial E_z}{\partial r}\frac{\partial r}{\partial x} + \frac{\partial E_z}{\partial \varphi}\frac{\partial \varphi}{\partial x} = \frac{x}{r}\frac{\partial Ez}{\partial r} - \frac{y}{r^2}\frac{\partial E_z}{\partial \varphi}, \tag{5.30}$$

$$\frac{\partial^2 E_z}{\partial x^2} = \frac{\partial}{\partial x}\left(\frac{x}{r}\frac{\partial Ez}{\partial r} - \frac{y}{r^2}\frac{\partial E_z}{\partial \varphi}\right)$$

$$= \frac{\partial}{\partial x}\left(\frac{x}{r}\right)\frac{\partial E_z}{\partial r} + \frac{x}{r}\frac{\partial^2 Ez}{\partial r^2} - \frac{\partial}{\partial x}\left(\frac{y}{r^2}\right)\frac{\partial E_z}{\partial \varphi} - \frac{y}{r^2}\frac{\partial^2 E_z}{\partial \varphi^2}$$

$$= \frac{\frac{\partial x}{\partial x} r - x\frac{\partial r}{\partial x}}{r^2}\frac{\partial Ez}{\partial r} + \frac{x}{r}\frac{\partial^2 Ez}{\partial r^2} - \frac{0 - y2r\frac{1}{2}(x^2+y^2)^{-\frac{1}{2}}2x}{r4}\frac{\partial E_z}{\partial \varphi} - \frac{y}{r^2}\frac{\partial^2 E_z}{\partial \varphi^2}$$

$$= (\frac{1}{r} - \frac{x^2}{r^3})\frac{\partial Ez}{\partial r} + \frac{x}{r}(\frac{\partial^2 Ez}{\partial r^2}\frac{\partial r}{\partial x} + \frac{\partial^2 E_z}{\partial r \partial \varphi}\frac{\partial \varphi}{\partial x}) + \frac{2xy}{r^4}\frac{\partial E_z}{\partial \varphi} - \frac{y}{r^2}(\frac{\partial^2 E_z}{\partial r \partial \varphi}\frac{\partial r}{\partial x} + \frac{\partial^2 E_z}{\partial \varphi^2}\frac{\partial \varphi}{\partial x})$$

$$= (\frac{1}{r} - \frac{x^2}{r^3})\frac{\partial Ez}{\partial r} + \frac{x}{r}(\frac{x}{r}\frac{\partial^2 Ez}{\partial r^2} - \frac{y}{r^2}\frac{\partial^2 E_z}{\partial r \partial \varphi}) + \frac{2xy}{r^4}\frac{\partial E_z}{\partial \varphi} - \frac{y}{r^2}(\frac{x}{r}\frac{\partial^2 E_z}{\partial r \partial \varphi} - \frac{y}{r^2}\frac{\partial^2 E_z}{\partial \varphi^2}),$$

(5.31)

$$\frac{\partial E_z}{\partial y} = \frac{\partial E_z}{\partial r}\frac{\partial r}{\partial y} + \frac{\partial E_z}{\partial \varphi}\frac{\partial \varphi}{\partial y} = \frac{y}{r}\frac{\partial Ez}{\partial r} + \frac{x}{r^2}\frac{\partial E_z}{\partial \varphi}, \tag{5.32}$$

$$\frac{\partial^2 E_z}{\partial y^2} = \frac{\partial}{\partial y}(\frac{y}{r}\frac{\partial Ez}{\partial r} + \frac{x}{r^2}\frac{\partial E_z}{\partial \varphi})$$

$$= \frac{\partial}{\partial y}(\frac{y}{r})\frac{\partial E_z}{\partial r} + \frac{y}{r}\frac{\partial^2 Ez}{\partial r^2} + \frac{\partial}{\partial y}(\frac{x}{r^2})\frac{\partial E_z}{\partial \varphi} + \frac{x}{r^2}\frac{\partial^2 E_z}{\partial \varphi^2}$$

$$= \frac{\frac{\partial y}{\partial x} r - y\frac{\partial r}{\partial x}}{r^2}\frac{\partial E_z}{\partial r} + \frac{y}{r}\frac{\partial^2 Ez}{\partial r^2} + \frac{0 - x*2r*\frac{1}{2}*(x^2+y^2)^{-\frac{1}{2}}*2y}{r4}\frac{\partial E_z}{\partial \varphi} + \frac{x}{r^2}\frac{\partial^2 E_z}{\partial \varphi^2}$$

$$= (\frac{1}{r} - \frac{x^2}{r^3})\frac{\partial Ez}{\partial r} + \frac{y}{r}(\frac{\partial^2 Ez}{\partial r^2}\frac{\partial r}{\partial y} + \frac{\partial^2 E_z}{\partial r \partial \varphi}\frac{\partial \varphi}{\partial y}) - \frac{2xy}{r^4}\frac{\partial E_z}{\partial \varphi} - \frac{x}{r^2}(\frac{\partial^2 E_z}{\partial r \partial \varphi}\frac{\partial r}{\partial y} + \frac{\partial^2 E_z}{\partial \varphi^2}\frac{\partial \varphi}{\partial y})$$

$$= (\frac{1}{r} - \frac{y^2}{r^3})\frac{\partial Ez}{\partial r} + \frac{y}{r}(\frac{y}{r}\frac{\partial^2 Ez}{\partial r^2} + \frac{x}{r^2}\frac{\partial^2 E_z}{\partial r \partial \varphi}) - \frac{2xy}{r^4}\frac{\partial E_z}{\partial \varphi} + \frac{x}{r^2}(\frac{y}{r}\frac{\partial^2 E_z}{\partial r \partial \varphi} + \frac{x}{r^2}\frac{\partial^2 E_z}{\partial \varphi^2}),$$

(5.33)

Maxwell's equations are rewritten in terms of the cylindrical coordinates, substituting Eqs. 5.31 and 5.33 into Eq. 5.21 gives:

$$(\frac{1}{r} - \frac{x^2}{r^3})\frac{\partial Ez}{\partial r} + \frac{x}{r}(\frac{x}{r}\frac{\partial^2 Ez}{\partial r^2} - \frac{y}{r^2}\frac{\partial^2 E_z}{\partial r \partial \varphi}) + \frac{2xy}{r^4}\frac{\partial E_z}{\partial \varphi} - \frac{y}{r^2}(\frac{x}{r}\frac{\partial^2 E_z}{\partial r \partial \varphi} - \frac{y}{r^2}\frac{\partial^2 E_z}{\partial \varphi^2})$$

$$+ (\frac{1}{r} - \frac{y^2}{r^3})\frac{\partial Ez}{\partial r} + \frac{y}{r}(\frac{y}{r}\frac{\partial^2 Ez}{\partial r^2} + \frac{x}{r^2}\frac{\partial^2 E_z}{\partial r \partial \varphi}) - \frac{2xy}{r^4}\frac{\partial E_z}{\partial \varphi} + \frac{x}{r^2}(\frac{y}{r}\frac{\partial^2 E_z}{\partial r \partial \varphi} + \frac{x}{r^2}\frac{\partial^2 E_z}{\partial \varphi^2})$$
$$+ \beta_t E_z = 0$$

$$\frac{2}{r}\frac{\partial Ez}{\partial r}-\frac{r^2}{r^3}\frac{\partial Ez}{\partial r}+\frac{r^2}{r^3}\frac{\partial^2 Ez}{\partial r^2}+\frac{r^2}{r^4}\frac{\partial^2 E_z}{\partial \varphi^2}+\beta_t E_z=0$$

$$\frac{\partial^2 Ez}{\partial r^2}+\frac{1}{r}\frac{\partial Ez}{\partial r}+\frac{1}{r^2}\frac{\partial^2 E_z}{\partial \varphi^2}+\beta_t E_z=0 \tag{5.34}$$

In the same way:

$$\frac{\partial^2 Hz}{\partial r^2}+\frac{1}{r}\frac{\partial Hz}{\partial r}+\frac{1}{r^2}\frac{\partial^2 H_z}{\partial \varphi^2}+\beta_t H_z=0 \tag{5.35}$$

We look for a separable solution of the form:

$$E_z(r,\varphi)=\mathrm{R}(r)\Phi(\varphi) \tag{5.36}$$

The z dependence of E_z is $e^{i\omega t-\beta z}$, as before, but this factor will be omitted for simplicity.

Substituting Eq. 5.36 into Eq. 5.34 gives:

$$\mathrm{r}^2\frac{R''(r)}{R}+r\frac{R'(r)}{R}+\beta_t r^2=\frac{\Phi''(\varphi)}{\Phi} \tag{5.37}$$

For Eq. 5.37 to be satisfied each side is independently equal to a constant, since the left-hand side is only a function of r, and the right-hand side is only a function of φ. The following equation may be derived:

$$r^2\frac{R''(r)}{R}+r\frac{R'(r)}{R}+\beta_t{}^2 r^2=\nu^2 \tag{5.38}$$

which is usually written as:

$$R''+\frac{1}{r}\frac{\partial R}{\partial r}+(\beta_t{}^2-\frac{\nu^2}{r^2})R=0 \tag{5.39}$$

and

$$-\frac{\Phi''}{\Phi}=\nu \tag{5.40}$$

The general solution of Eq. 5.40 is:

$$\Phi(\varphi)=\mathrm{N}\sin(\nu\,\varphi)+\mathrm{M}\cos(\nu\,\varphi) \tag{5.41}$$

ν must be a positive or negative integer, or zero, so that the function $\Phi(\varphi)$ is single valued:

i.e., $\Phi(\varphi+2\pi) = \Phi(\varphi)$.

Eq. 5.39 is called Bessel's equation. Its solutions are Bessel functions, which are the cylindrical geometry equivalents of the real or complex exponential solutions.

In the core region, $r < a$ (a is the radius of fibre core), the general solution of Eq. 4.43 is:

$$R(r) = A\, J_m(\beta_t r) + B\, Y_m(\beta_t r), \quad (\text{where } \beta_t \text{ is real}) \tag{5.42}$$

where $J_m(\beta_t r)$ is the Bessel function of the first kind and $Y_m(\beta_t r)$ is the Bessel function of the second kind(The Bessel function of the second kind $Y_m(\beta_t r)$ is also written as $N_m(\beta_t r)$ in some texts).

In the cladding region, $r > a$, the general solution of Eq. 5.39 is:

$$R(r) = C\, I_m(|\beta_t| r) + D K_m(|\beta_t| r), \quad (\text{Where } \beta_t \text{ is imaginary}) \tag{5.43}$$

Where $I_m(|\beta_t| r)$, $K_m(|\beta_t| r)$ are modified Bessel functions of the first and second kinds respectively. These are monotonically increasing ($I_m(|\beta_t| r)$) and decreasing ($K_m(|\beta_t| r)$) functions of r. In the core, we expect an oscillatory form of the axial field to be appropriate. Since the function $Y_m(\beta_t r) \rightarrow -\infty$ as $r \rightarrow 0$, as shown in Fig. 5.3, we reject $Y_m(\beta_t r)$ as physically unreasonable. Only the $J_m(\beta_t r)$ variation needs to be retained as shown in Fig. 5.2.

The fields in the cladding must decay as we go further away from the core. Since $I_m(|\beta_t| r) \rightarrow \infty$ as $r \rightarrow \infty$, as shown in Fig. 5.4. These functions are rejected since they are physically unreasonable. Only the $K_m(|\beta_t| r)$ variation is reasonable as shown in Fig. 5.5, and needs to be retained.

In these solutions, m is the azimuthal mode number and A, B, C and D are arbitrary constants.

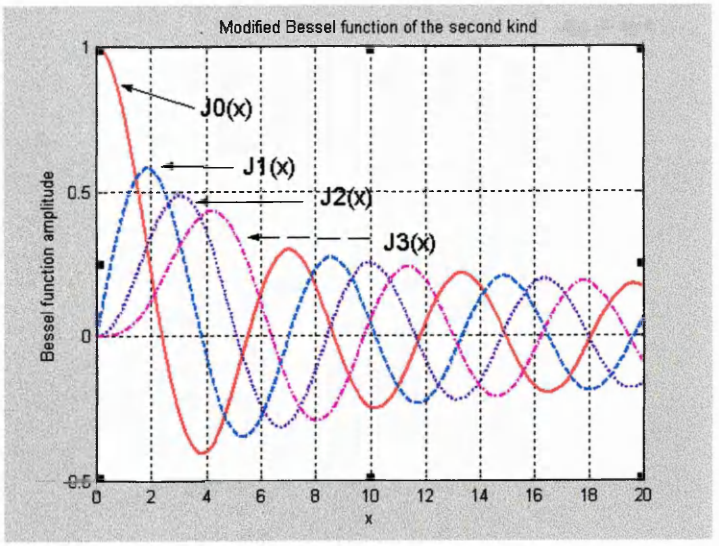

Fig. 5.2. Bessel function of the first kind.

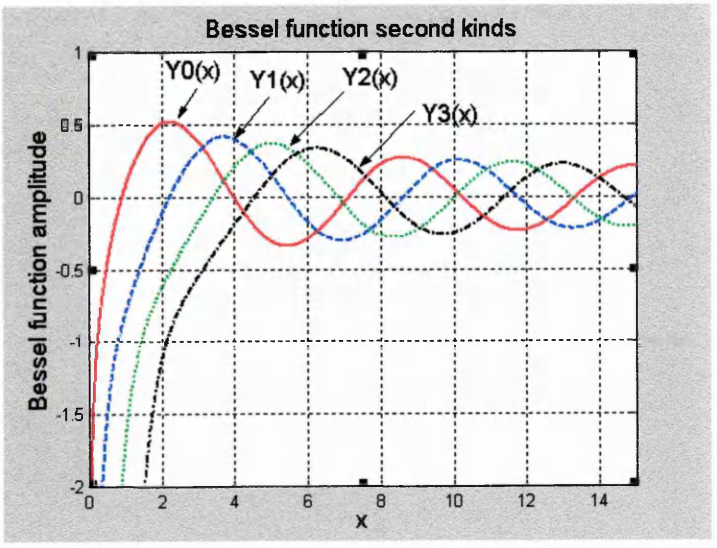

Fig. 5.3. Bessel function of second kind.

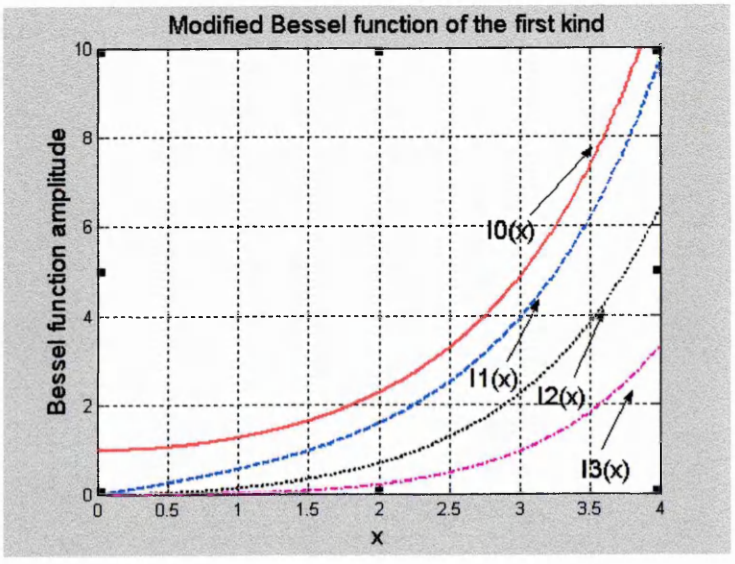

Fig. 5.4. Modified Bessel function of the first kind.

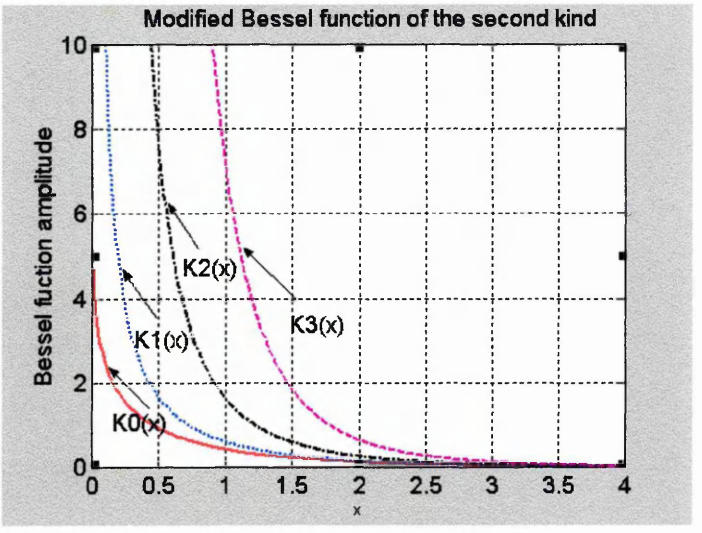

Fig. 5.5. Modified Bessel function of the second kind.

5.1.3 Electromagnetic Field in the Core and Cladding

Assuming temporarily that two sets of solutions (TM-type solutions) are present in which:

$$E_z = \begin{cases} AJ_m(\beta_{t1})\sin n\varphi & (for \quad r \le a), \\ CK_m(|\beta_{t2}|)\sin n\varphi & (for \quad r \ge a), \end{cases} \tag{5.44}$$

$$\tag{5.45}$$

$$H_z = 0 \qquad \text{(throughout)}, \tag{5.46}$$

And (TE-type solutions)

$$H_z = \begin{cases} BJ_m(\beta_{t1})\cos n\varphi & (for \quad r \le a), \\ BK_m(|\beta_{t2}|)\cos n\varphi & (for \quad r \ge a), \end{cases} \tag{5.47}$$

$$\tag{5.48}$$

$$E_z = 0 \qquad \text{(throughout)} \tag{5.49}$$

where suffixes 1 and 2 denote the core and cladding regions, respectively.

5.1.3.1 Field in the Core

Let us write down the full variation of the fields in the core as:

$$E_z = A\ J_m(\frac{ur}{a})\sin m\varphi, \tag{5.50}$$

Substituting Eqs. 5.15, and 5.16 into Eq. 5.17 we get:

$$E_r = E_x\cos\varphi + E_y\sin\varphi$$

$$= -\frac{i}{\beta_t^2}(\beta\frac{\partial E_z}{\partial x} + \omega\mu\frac{\partial H_z}{\partial y})\cos\varphi + (-\frac{i}{\beta_t^2}(\beta\frac{\partial Ez}{\partial y} - \omega\mu\frac{\partial Hz}{\partial x})\sin\varphi)$$

$$= -\frac{i}{\beta_t^2}\beta\frac{\partial E_z}{\partial x}\cos\varphi - \frac{i}{\beta_t^2}\omega\mu\frac{\partial H_z}{\partial y}\cos\varphi - \frac{i}{\beta_t^2}\beta\frac{\partial Ez}{\partial y}\sin\varphi + \omega\mu\frac{i}{\beta_t^2}\frac{\partial Hz}{\partial x}\sin\varphi$$

$$= -\frac{i}{\beta_t^2}\beta(\frac{\partial E_z}{\partial x}\cos\varphi + \frac{\partial E_z}{\partial y}\sin\varphi) - \frac{i}{\beta_t^2}\omega\mu(\frac{\partial H_z}{\partial y}\cos\varphi - \frac{\partial H_z}{\partial x}\sin\varphi)$$

using Eqs. 5.23, 5.24, 5.30 and 5.32 gives:

$$E_r = -\frac{i}{\beta_t^2}\beta\left((\frac{x}{r}\frac{\partial E_z}{\partial r} - \frac{y}{r^2}\frac{\partial E_z}{\partial\varphi})\cos\varphi + (\frac{y}{r}\frac{\partial E_z}{\partial r} + \frac{x}{r^2}\frac{\partial E_z}{\partial\varphi})\sin\varphi)\right)$$

$$-\frac{i}{\beta_t^2}\omega\mu\left((\frac{y}{r}\frac{\partial H_z}{\partial r} + \frac{x}{r^2}\frac{\partial H_z}{\partial\varphi})\cos\varphi - (\frac{x}{r}\frac{\partial H_z}{\partial r} - \frac{y}{r^2}\frac{\partial H_z}{\partial\varphi})\sin\varphi)\right)$$

$$= -\frac{i}{\beta_t^2}\left\{\beta\left(\cos\varphi\frac{\partial E_z}{\partial r}\cos\varphi - \frac{1}{r}\sin\varphi\frac{\partial E_z}{\partial\varphi}\cos\varphi + \sin\varphi\frac{\partial E_z}{\partial r}\sin\varphi + \frac{1}{r}\cos\varphi\frac{\partial E_z}{\partial\varphi}\sin\varphi)\right)\right.$$

$$\left.+\omega\mu\left(\sin\varphi\frac{\partial H_z}{\partial r}\cos\varphi + \frac{1}{r}\cos\varphi\frac{\partial H_z}{\partial\varphi}\cos\varphi - \cos\varphi\frac{\partial H_z}{\partial r}\sin\varphi + \frac{1}{r}\sin\varphi\frac{\partial H_z}{\partial\varphi}\sin\varphi\right)\right\}$$

$$= -\frac{i}{\beta_t^2}(\beta(\cos\varphi\cos\varphi + \sin\varphi\sin\varphi)\frac{\partial E_z}{\partial r} + \omega\mu\frac{1}{r}(\cos\varphi\cos\varphi + \sin\varphi\sin\varphi)\frac{\partial H_z}{\partial\varphi}$$

$$\therefore E_r = -\frac{i}{\beta_t^2}\left(\beta\frac{\partial E_z}{\partial r} + \omega\mu\frac{1}{r}\frac{\partial H_z}{\partial\varphi}\right)$$

using Eq. 5.44 and Eq. 5.47 it gives:

$$E_r = -\frac{i}{\beta_t^2}\left(\beta(AJ_m(\frac{ur}{a})\frac{u}{r}\sin m\varphi) + \omega\mu\frac{1}{r}(BJ_m(\frac{ur}{a})(-\sin m\varphi)m)\right)$$

$$= -\frac{i}{\left(\frac{u}{a}\right)^2}\left(\beta A J_m(\frac{ur}{a})\frac{u}{r}\sin m\varphi - \omega\mu\frac{m}{r}BJ_m(\frac{ur}{a})\sin m\varphi\right)$$

$$E_r = \left[-A\frac{j\beta}{u/a}J'_m(\frac{ur}{a}) + B\frac{j\omega\mu_0}{(u/a)^2}\frac{m}{r}J_m(\frac{ur}{a})\right]\sin m\varphi \tag{5.51}$$

Using the same method the following expressions are derived on:

$$E_\varphi = \left[-A\frac{j\beta}{(u/a)^2}\frac{m}{r}J_m(\frac{ur}{a}) + B\frac{j\omega\mu_0}{u/a}J'_m(\frac{ur}{a})\right]\cos m\varphi \tag{5.52}$$

$$H_z = \mathrm{B}\,J_m(\frac{ur}{a})\cos \mathrm{m}\varphi, \tag{5.53}$$

$$H_r = \left[A\frac{j\omega\varepsilon_1}{(u/a)^2}\frac{m}{r}J_m(\frac{ur}{a}) + B\frac{j\beta}{u/a}J'_m(\frac{ur}{a})\right]\cos m\varphi, \tag{5.54}$$

$$H_\varphi = \left[-A\frac{j\omega\varepsilon_1}{u/a}J_m'(\frac{ur}{a}) + B\frac{j\beta}{(u/a)^2}\frac{m}{r}J_m(\frac{ur}{a})\right]\cos m\varphi, \tag{5.55}$$

where the normalized transverse constant in the core region is given as:

$$u^2 = kn_1^{\,2} - \beta^2, \tag{5.56}$$

5.1.3.2 Field in the Cladding Region

The electronic field propagating is E-direction within the cladding region is given as:

$$E_z = C\,K_m(\frac{wr}{a})\sin m\theta, \tag{5.57}$$

$$E_r = \left[C\frac{j\beta}{w/a}K'_m(\frac{wr}{a}) - D\frac{j\omega\mu_0}{(w/a)^2}\frac{m}{r}K_m(\frac{wr}{a})\right]\sin m\varphi, \tag{5.58}$$

$$E_\varphi = \left[C\frac{j\beta}{(w/a)^2}\frac{m}{r}J_m(\frac{wr}{a}) - D\frac{j\omega\mu_0}{w/a}K'_m(\frac{wr}{a})\right]\cos m\varphi, \tag{5.59}$$

$$H_z = D\,K_m(\frac{wr}{a})\cos \mathrm{m}\varphi, \tag{5.60}$$

$$H_r = \left[-C\frac{j\omega\varepsilon_2}{(u/a)^2}\frac{m}{r}K_m(\frac{wr}{a}) + D\frac{j\beta}{u/a}K'_m(\frac{wr}{a}) \right]\cos m\varphi, \tag{5.61}$$

$$H_\varphi = \left[C\frac{j\omega\varepsilon_2}{w/a}K_m'(\frac{wr}{a}) - D\frac{j\beta}{(u/a)^2}\frac{m}{r}K_m(\frac{wr}{a}) \right]\sin m\varphi, \tag{5,62}$$

where the normalized transverse attenuation constant in the cladding region is given as:

$$w^2 = \beta^2 - kn_2^{\ 2} \tag{5.63}$$

5.1.4 Mode Propagation Constant—Exact Solutions

The propagation constants are determined by the boundary conditions (conditions for the continuity of fields) at the core –cladding boundary (r = a):

$$E_z^{\text{core}} = E_z^{\text{cladding}}, \tag{5.64}$$

$$E_\varphi^{\text{core}} = E_\varphi^{\text{cladding}}, \tag{5.65}$$

$$E_z^{\text{core}} = H_z^{\text{cladding}}, \tag{5.66}$$

$$E_\varphi^{\text{core}} = H_\varphi^{\text{cladding}}, \tag{5.67}$$

$$\varepsilon_1 E_z^{\text{core}} = \varepsilon_2 E_z^{\text{cladding}}, \tag{5.68}$$

$$\mu_1 H_z^{\text{core}} = \mu_2 H_z^{\text{cladding}}, \tag{5.69}$$

where suffixes 1 and 2 again denote the core and cladding regions, respectively. In nonmagnetic material, $\mu_1 = \mu_2 = \mu_0$ as in Eq. 5.69.

Let $r = a$ in Eqs. 5.50 — 5.55, and Eqs. 5.57 — 5.62, and then substituting these into Eqs. 5.64, 5.66, 5.67 and 5.68, the A, B, C and D must satisfy the following:

$$J_m(u) - CK_m(w) = 0, \tag{5.70}$$

$$BJ_m(u) - DK_m(w) = 0, \tag{5.71}$$

$$A\frac{j\beta}{(u/a)^2}\frac{m}{r}J_m(\frac{ur}{a}) - B\frac{j\omega\mu_0}{u/a}J'_m(\frac{ur}{a}) + C\frac{j\beta}{(w/a)^2}\frac{m}{r}J_m(\frac{wr}{a}) - D\frac{j\omega\mu_0}{w/a}K'_m(\frac{wr}{a}) = 0, \tag{5.72}$$

$$A\frac{j\beta\varepsilon_1}{u/a}J_m'(\frac{ur}{a})-B\frac{j\omega\mu_0\varepsilon_1}{(u/a)^2}\frac{m}{r}J_m(\frac{ur}{a})+C\frac{j\beta\varepsilon_2}{w/a}K_m'(\frac{wr}{a})-D\frac{j\omega\mu_0\varepsilon_2}{(u/a)^2}\frac{m}{r}K_m(\frac{wr}{a})=0, \tag{5.73}$$

$$[M]\cdot\begin{bmatrix}A\\B\\C\\D\end{bmatrix}=0 \tag{5.74}$$

For the so-called non-trivial solution to exist for the column vector [*A, B, C, D*]

$$\det[M]=0, \tag{5.75}$$

It can be shown that the use of this relationship yield the following mode condition that determines the propagation constant.

$$\begin{bmatrix} J_m(u) & 0 & -K_m(w) & 0 \\ 0 & J_m(u) & 0 & -K_m(w) \\ \frac{j\beta}{(u/a)^2}\frac{m}{r}J_m(\frac{ur}{a}) & -\frac{j\omega\mu_0}{u/a}J'_m(\frac{ur}{a}) & \frac{j\beta}{(w/a)^2}\frac{m}{r}K_m(\frac{wr}{a}) & -\frac{j\omega\mu_0}{w/a}K'_m(\frac{wr}{a}) \\ \frac{j\beta\varepsilon_1}{u/a}J'_m(\frac{ur}{a}) & -\frac{j\omega\mu_0\varepsilon_1}{(u/a)^2}\frac{m}{r}J_m(\frac{ur}{a}) & \frac{j\beta\varepsilon_2}{w/a}K'_m(\frac{wr}{a}) & -\frac{j\omega\mu_0\varepsilon_2}{(w/a)^2}\frac{m}{r}K_m(\frac{wr}{a}) \end{bmatrix} = 0$$

$$= J_m(u)\begin{bmatrix} J_m(u) & 0 & -K_m(w) \\ -\frac{j\omega\mu_0}{u/a}J'_m(\frac{ur}{a}) & \frac{j\beta}{(w/a)^2}\frac{m}{r}K_m(\frac{wr}{a}) & -\frac{j\omega\mu_0}{w/a}K'_m(\frac{wr}{a}) \\ -\frac{j\omega\mu_0}{(u/a)^2}\frac{m}{r}J_m(\frac{ur}{a}) & \frac{j\beta\varepsilon_2}{w/a}K'_m(\frac{wr}{a}) & -\frac{j\omega\mu_0\varepsilon_2}{(w/a)^2}\frac{m}{r}K_m(\frac{wr}{a}) \end{bmatrix}$$

$$-K_m(w)\begin{bmatrix} 0 & J_m(u) & -K_m(w) \\ \frac{j\beta}{(u/a)^2}\frac{m}{r}J_m(\frac{ur}{a}) & -\frac{j\omega\mu_0}{u/a}J'_m(\frac{ur}{a}) & -\frac{j\omega\mu_0}{w/a}K'_m(\frac{wr}{a}) \\ \frac{j\beta\varepsilon_1}{u/a}J'_m(\frac{ur}{a}) & -\frac{j\omega\mu_0\varepsilon_1}{(u/a)^2}\frac{m}{r}J_m(\frac{ur}{a}) & -\frac{j\omega\mu_0\varepsilon_2}{(w/a)^2}\frac{m}{r}K_m(\frac{wr}{a}) \end{bmatrix}$$

$$= J_m(u)\left(J_m(u)\begin{bmatrix} \frac{j\beta}{(w/a)^2}\frac{m}{r}K_m(\frac{wr}{a}) & -\frac{j\omega\mu_0}{w/a}K'_m(\frac{wr}{a}) \\ \frac{j\beta\varepsilon_2}{w/a}K'_m(\frac{wr}{a}) & -\frac{j\omega\mu_0\varepsilon_2}{(w/a)^2}\frac{m}{r}K_m(\frac{wr}{a}) \end{bmatrix}\right.$$

$$\left. -K_m(\mathrm{w})\begin{bmatrix} -\frac{j\omega\mu_0}{u/a}J'_m(\frac{ur}{a}) & \frac{j\beta}{(w/a)^2}\frac{m}{r}K_m(\frac{wr}{a}) \\ -\frac{j\omega\mu_0}{(u/a)^2}\frac{m}{r}J_m(\frac{ur}{a}) & \frac{j\beta\varepsilon_2}{w/a}K'_m(\frac{wr}{a}) \end{bmatrix}\right)$$

$$-K_m(w)\left(-J_m(u)\begin{bmatrix} \frac{j\beta}{(u/a)^2}\frac{m}{r}J_m(\frac{ur}{a}) & -\frac{j\omega\mu_0}{w/a}K'_m(\frac{wr}{a}) \\ \frac{j\beta\varepsilon_1}{u/a}J'_m(\frac{ur}{a}) & -\frac{j\omega\mu_0\varepsilon_2}{(w/a)^2}\frac{m}{r}K_m(\frac{wr}{a}) \end{bmatrix}\right.$$

$$\left. -K_m(\mathrm{w})\begin{bmatrix} \frac{j\beta}{(u/a)^2}\frac{m}{r}J_m(\frac{ur}{a}) & -\frac{j\omega\mu_0}{u/a}J'_m(\frac{ur}{a}) \\ \frac{j\beta\varepsilon_1}{u/a}J'_m(\frac{ur}{a}) & -\frac{j\omega\mu_0\varepsilon_1}{(u/a)^2}\frac{m}{r}J_m(\frac{ur}{a}) \end{bmatrix}\right)$$

$$= J_m{}^2(u)\left(-\frac{j\beta}{(w/a)^2}\frac{m}{r}K_m(\frac{wr}{a})\frac{j\omega\mu_0\varepsilon_2}{(w/a)^2}\frac{m}{r}K_m(\frac{wr}{a}) + \frac{j\beta\varepsilon_2}{w/a}K'_m(\frac{wr}{a})\frac{j\omega\mu_0}{w/a}K'_m(\frac{wr}{a})\right)$$

$$-J_m(u)K_m(w)\left(-\frac{j\omega\mu_0}{u/a}J'_m(\frac{ur}{a})\frac{j\beta\varepsilon_2}{w/a}K'_m(\frac{wr}{a}) + \frac{j\omega\mu_0}{(u/a)^2}\frac{m}{r}J_m(\frac{ur}{a})\frac{j\beta}{(w/a)^2}\frac{m}{r}J_m(\frac{wr}{a})\right)$$

$$K_m(w)J_m(u)\left(-\frac{j\beta}{(u/a)^2}\frac{m}{r}J_m(\frac{ur}{a})\frac{j\omega\mu_0\varepsilon_2}{(w/a)^2}\frac{m}{r}K_m(\frac{wr}{a}) + \frac{j\beta\varepsilon_1}{u/a}J'_m(\frac{ur}{a})\frac{j\omega\mu_0}{w/a}K'_m(\frac{wr}{a})\right)$$

$$K^2{}_m(w)\left(-\frac{j\beta}{(u/a)^2}\frac{m}{r}J_m(\frac{ur}{a})\frac{j\omega\mu_0\varepsilon_1}{(u/a)^2}\frac{m}{r}J_m(\frac{ur}{a}) + \frac{j\beta\varepsilon_1}{u/a}J'_m(\frac{ur}{a})\frac{j\omega\mu_0}{u/a}J'_m(\frac{ur}{a})\right)=0$$

Since $r = a$, we get:

$$-J_m^2(\mathrm{u})\ K^2{}_m(\mathrm{w})\frac{\omega\mu_0\varepsilon_2 m^2}{w^4} + J_m^2(\mathrm{u})\ K'^2{}_m(\mathrm{w})\frac{\omega\mu_0\varepsilon_2}{w^2}$$

$$+ J_m(\mathrm{u})\ K_m(\mathrm{w})J'_m(\mathrm{u})K'_m(\mathrm{w})\frac{\omega\mu_0\varepsilon_2}{uw}$$

$$-J_m^2(u)\ K_m^2(w)\frac{\omega\mu_0\varepsilon 1 m^2}{u^2w^2} - J_m^2(\mathrm{u})(\mathrm{u})\ K_m^2(\mathrm{w})\frac{\omega\mu_0\varepsilon_2 m^2}{u^2w^2} + J_m(u)K_m(w)J'_m(u)$$

$$K_m'(w)\frac{\omega\mu_0\varepsilon_2}{uw} - J_m^2(u)\ K_m^2\ (w)\frac{\mu_0\varepsilon_1 m^2}{u^4} + J'^2{}_m(u)\ K_m^2\ (w)\frac{\varpi\mu_0\varepsilon_1}{u^2} = 0$$

since $\mu_1 = \mu_2 = \mu_0$ we get:

$$J^2{}_m(u)K'^2{}_m(w)\frac{\varepsilon_2 m^2}{w^2} + J_m(u)\ K_m(w)J'_m(u)K'_m(w)\frac{\varepsilon_2}{uw}$$

$$+ J_m(u)\ K_m(w)J'_m(u)K'_m(w)\frac{\varepsilon_2}{uw} + J'^2{}_m(\mathrm{u})\ K_m^2\ (\mathrm{w})\frac{\varepsilon_1}{u^2}$$

$$= J_m^2(\mathrm{u})\ K_m^2\ (\mathrm{w})\frac{\varepsilon_2 m^2}{w^4} - J_m^2(\mathrm{u})\ K_m^2\ (\mathrm{w})\frac{\varepsilon_1 m^2}{u^2 w^2}$$

$$- J_m^2(\mathrm{u})K_m^2(\mathrm{w})\frac{\varepsilon_2 m^2}{u^2 w^2} + J_m^2(\mathrm{u})K_m^2\ (\mathrm{w})\frac{\varepsilon_1 m^2}{u^4}$$

$$\left[\frac{J_m'(u)}{uJ_m(u)} + \frac{K_m'(w)}{wK_m(w)}\right]\left[\varepsilon_1\frac{J_m'(u)}{uJ_m(u)} + \varepsilon_2\frac{K_m'(w)}{wK_m(w)}\right] = m^2\left(\frac{1}{u^2}+\frac{1}{w^2}\right)\left(\varepsilon_1\frac{1}{u^2}+\varepsilon_2\frac{1}{w^2}\right)$$

or

$$\left[\frac{J_m'(u)}{uJ_m(u)} + \frac{K_m'(w)}{wK_m(w)}\right]\left[\frac{\varepsilon_1}{\varepsilon_2}\frac{J_m'(u)}{uJ_m(u)} + \frac{K_m'(w)}{wK_m(w)}\right] = m^2\left(\frac{1}{u^2}+\frac{1}{w^2}\right)\left(\frac{\varepsilon_1}{\varepsilon_2}\frac{1}{u^2}+\frac{1}{w^2}\right) \tag{5.76}$$

With the refractive index given as:

$$n = \frac{C}{V} = \sqrt{\frac{\varepsilon\mu}{\varepsilon_0\mu_0}}, \tag{5.77}$$

where C and V are the speed of light in vacuum and in a medium, respectively, and ε and μ denote the permittivity and permeability of that medium,

$$\mu_0 = \mu_1 = \mu_2, \tag{5.78}$$

We obtain the following relations:

$$\varepsilon_1 = \varepsilon_0 n_1^2, \tag{5.79}$$

$$\varepsilon_2 = \varepsilon_0 n_2^2, \tag{5.80}$$

Finally:

$$\left[\frac{J_m'(u)}{uJ_m(u)}+\frac{K_m'(w)}{wK_m(w)}\right]\left[\frac{n_1^{\,2}}{n_2^{\,2}}\frac{J_m'(u)}{uJ_m(u)}+\frac{K_m'(w)}{wK_m(w)}\right]=m^2\left(\frac{1}{u^2}+\frac{1}{w^2}\right)\left(\frac{n_1^{\,2}}{n_2^{\,2}}\frac{1}{u^2}+\frac{1}{w^2}\right), \tag{5.81}$$

Eq. 5.81 together with $u=\left(k^2n_1^{\,2}-\beta^2\right)^{\frac{1}{2}}a$ and $w=\left(\beta^2-k^2n_2^{\,2}\right)^{\frac{1}{2}}a$, is a transcendental function of β for each m.

5.1.4.1 Core Mode Propagation Constants-Weakly Guiding Approximation

Under the weakly guiding approximation, determined by $\Delta=\frac{n_1-n_2}{n_1}<<1$ and $n_1\approx n_2$, Eq. 5.81 can be simplified. In view of $\Delta\approx 0$ and $n_1\approx n_2$, the left-hand side of Eq. 5.81 is virtually replaceable by $\left(\frac{J_m'(u)}{uJ_m(u)}+\frac{K_m'(w)}{wK_m(w)}\right)^2$, while its right-hand side is already in the form of square $m^2\left(\frac{1}{u^2}+\frac{1}{w^2}\right)^2$. Taking the square root for both sides result is:

$$\frac{J_m'(u)}{uJ_m(u)}+\frac{K_m'(w)}{wK_m(w)}=\pm m\left(\frac{1}{u^2}+\frac{1}{w^2}\right) \tag{5.82}$$

Even for a simple expression like Eq. 5.82 a further simplification is still possible, as outlined below:

since $J_{m+1}(u)+J_{m-1}(u)=2(m/u)J_m(u)$, (5.83)

$$K_{m+1}(w)-K_{m-1}(w)=2(n/w)K_m(w), \tag{5.84}$$

$$J_{-m}=(-1)^mJ_m, \tag{5.85}$$

$$K_{-m}=K_m, \tag{5.86}$$

$$2J_m' = J_{m-1} - J_{m+1}, \tag{5.87}$$

$$-2K_m' = K_{m-1} + K_{m+1}, \tag{5.88}$$

then the following relations are derived:

$$\frac{J'_m(u)}{uJ_m(u)} = \frac{\frac{1}{2}(J_{m-1}(u) - J_{m+1}(u))}{uJ_m(u)} = \frac{J_{m-1} - \frac{1}{2}(J_{m-1}(u) + J_{m+1}(u))}{uJ_m(u)}$$

$$= \frac{J_{m-1} - \frac{1}{2}(2(\frac{m}{u})J_m(u))}{uJ_m(u)} = \frac{J_{m-1}}{uJ_m} - \frac{m}{u^2}, \tag{5.89}$$

$$\frac{J'_m(u)}{uJ_m(u)} = \frac{\frac{1}{2}(J_{m-1}(u) - J_{m+1}(u))}{uJ_m(u)} = \frac{-J_{m+1} + \frac{1}{2}(J_{m-1}(u) + J_{m+1}(u))}{uJ_m(u)}$$

$$= \frac{-J_{m-1} + \frac{1}{2}(2(\frac{m}{u})J_m(u))}{uJ_m(u)} = -\frac{J_{m+1}}{uJ_m} + \frac{m}{u^2}, \tag{5.90}$$

Using the same method gives:

$$\frac{K'_m(w)}{wK_m(w)} = -\frac{K_{m-1}}{wK_m} - \frac{m}{w^2}, \tag{5.91}$$

$$\frac{K'_m(w)}{wK_m(w)} = -\frac{K_{m+1}}{wK_m} + \frac{m}{w^2}, \tag{5.92}$$

Eq. 5.82 gives two sets of solutions for the positive and negative signs. When the sign is positive, using Bessel formulas, inserting Eq. 5.90 and Eq. 5.92 into Eq. 5.82 gives:

$$\frac{J_m'(u)}{uJ_m(u)} + \frac{K_m'(w)}{wK_m(w)} = -\frac{J_{m+1}}{uJ_m} + \frac{m}{u^2} - \frac{K_{m+1}}{wK_m} + \frac{m}{w^2} = +m\left(\frac{1}{u^2} + \frac{1}{w^2}\right)$$

$$-\frac{J_{m+1}}{uJ_m} = \frac{K_{m+1}}{wK_m} \tag{5.93}$$

Those modes whose propagation constants are given as the solution to this equation are called EH modes.

In a similar way, when consider the negative sign in Eq. 5.82, and inserting Eq. 5.89 and Eq. 5.91 into Eq. 5.82 gives:

$$\frac{J_m'(u)}{uJ_m(u)}+\frac{K_m'(w)}{wK_m(w)}=+\frac{J_{m+1}}{uJ_m}-\frac{m}{u^2}-\frac{K_{m+1}}{wK_m}-\frac{m}{w^2}=-m\left(\frac{1}{u^2}+\frac{1}{w^2}\right)$$

$$\frac{J_{m-1}}{uJ_m}=\frac{K_{m-1}}{wK_m}, \tag{5.94}$$

or $$u\frac{J_m}{J_{m-1}}=w\frac{K_m}{K_{m-1}} \tag{5.95}$$

Those modes whose propagation constants are given as the solution to this equation are called HE modes.

5.1.4.2 Graphical Methods for Solving HE_{11} Core Mode

The basic idea for carrying out a graphics analysis is either to plot two curves in order to search for the cross-over, or to display a single curve against a real axis to produce possible zero-crossings. Here Eq. 5.95 is taken as an example to show how a general strait forward graphics method could be useful for allocating the solution of a transcendental equation like Eq. 5.95

Rewriting Eq. 5.95, and setting $m = 1$ for calculating the HE_{11} core mode, we have:

$$u\frac{J_1(u)}{J_0(u)}=w\frac{K_1(w)}{K_0(w)} \tag{5.96}$$

where $u^2=kn_1^2-\beta^2$, $w^2=\beta^2-kn_2^2$

Eq. 5.96 is evaluated using MATLAB and the results for both the left-hand side and right-hand side are shown in Fig. 5.6.

The parameters used are: $\lambda = 1.550$ μm, $a_1 = 2.635$ μm, $n_1 = 1.458$, $n_2 = 1.45$, and $n_2 k < \beta < n_1 k$. The MATLAB codes used are given in Appendix 3.5.

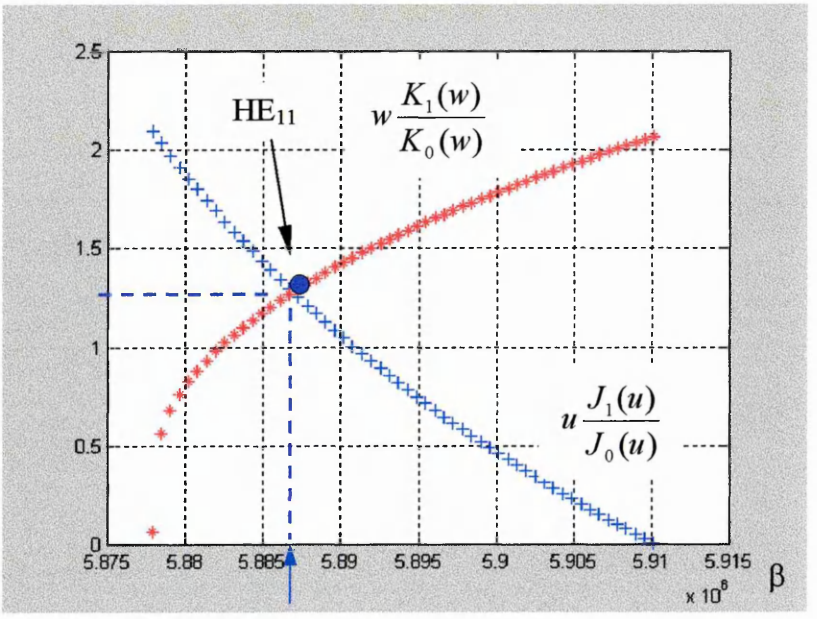

Fig. 5.6. The plot of $uJ_1(u)/J_0(u)$ And $wK(w)/K_0(w)$with the crossing corresponding to the solution HE_{11} mode of Eq. 5.96.

At a point where both curve cross, it corresponds to the HE $_{11}$ core mode, which is equal to 5.887×10^6.

Another Graphical method for solving core HE_{11} mode is outline below.

In order to display a single curve against a real axis to produce possible zero-crossings Eq. 5.99 can be rewritten as

$$f = u\frac{J_1(u)}{J_0(u)} - w\frac{K_1(w)}{K_0(w)} \tag{5.97}$$

A plot of Eq. 5.97 against β is shown in Fig. 5.7. Once again, at $f = 0$, the HE_{11} core mode of 5.887×10^6. is obtained as in above.

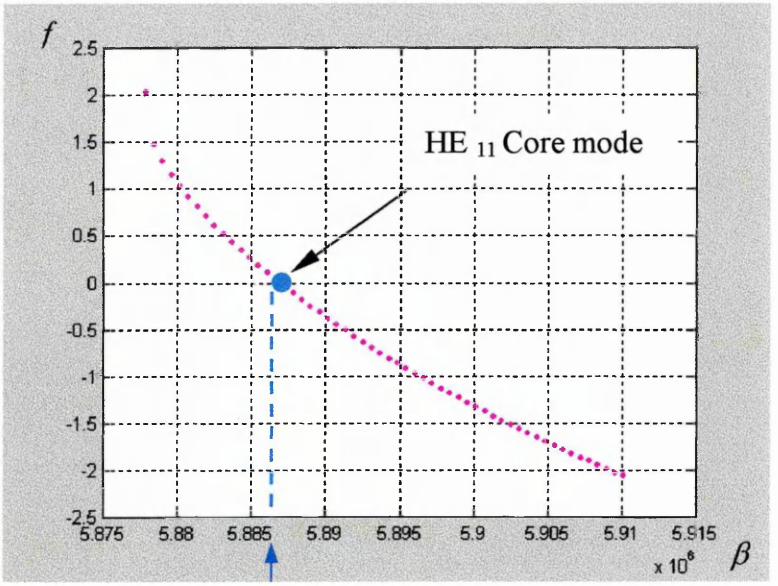

Fig. 5.7. Plot $f = uJ_1(u)/J_0(u) - wK(w)/K_0(w)$ a single curve to produce zero-crossing corresponding to the solution of HE_{11} mode of Eq. 5.97.

The MATLAB codes used are given in Appendix 3.6-1.

MATLAB is also used to calculate the HE_{11} mode and the value obtained is 5886929.131863, which agrees well with the result obtained graphically (see Fig. 5.7), the MATLAB code used is given in Appendix 3.6-2.

The custom that Eq. 4.93 is called EH modes and Eq. 4.95 called HE modes was established as early as the 1930s. There is no strong reason for the terminology. It is worth stating, however, that in EH modes the axial magnetic field H_z is relatively strong, whereas in HE modes the axial electric field E_z is relatively strong [Okoshi 1982]. The designation of HE and EH modes in other textbook is based on the relative contribution of E_z and H_z to a transverse component (e.g. E_r or E_ϕ) of the field [Yariv 1997]. In EH modes, E_z makes the large contribution, while H_z makes the large contribution to the HE modes. The HE_{11} mode can propagate at any wavelength, the

next modes which can propagate are TE_{01} and TM_{01} modes, while EH modes are higher order modes as is shown in Fig. 5.8. In single-mode fibre, only one HE_{11} mode can propagate.

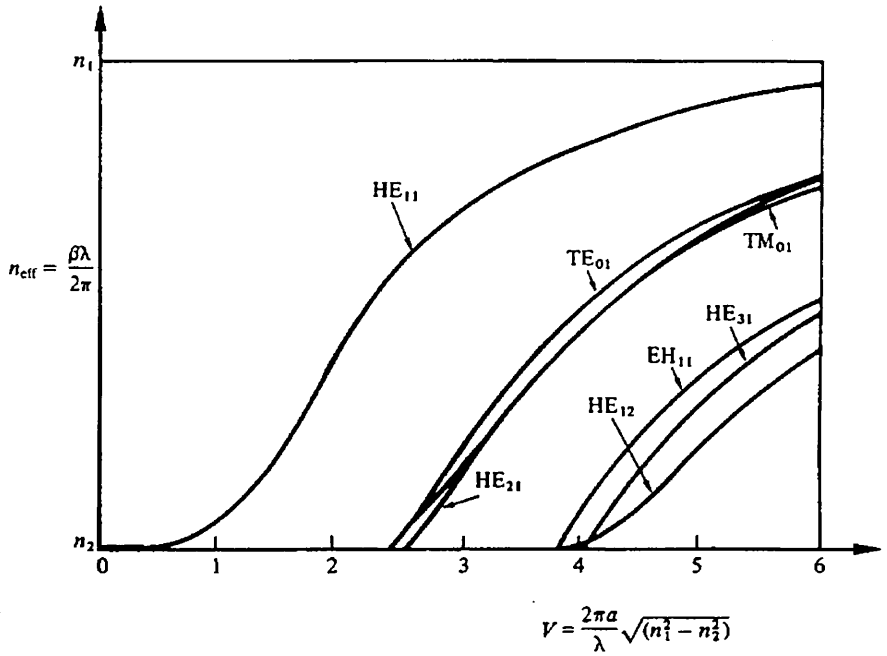

Fig. 5.8. Normalized propagation index, $n_{eff} = \beta\lambda / 2\pi$, as a function of the normalized frequency parameter V, for some of the lowest-order modes of step-index fibre [Gowar 1993].

5.1.4.3 HE Cladding Modes

Eq. 5.81 will yield cladding modes, but using graphical methods to find the HE mode values are not as easy as in the case of core modes. It is necessary therefore to develop another better method to determine the cladding modes. Letting $r = a$ in Eqs. 5.50 — 5.55 and Eqs. 5.57 — 5.62, and substituting into Eqs. 5.64, 5.65, 5.66 and 5.67 then A, B, C and D must satisfy:

$$A J_m(u) - C K_m(w) = 0, \tag{5.98}$$

$$B J_m(u) - D K_m(w) = 0, \tag{5.99}$$

$$A\frac{j\beta}{(u/a)^2}\frac{m}{r}J_m(\frac{ur}{a}) - B\frac{j\omega\mu_0}{u/a}J'_m(\frac{ur}{a}) + C\frac{j\beta}{(w/a)^2}\frac{m}{r}J_m(\frac{wr}{a}) - D\frac{j\omega\mu_0}{w/a}K'_m(\frac{wr}{a}) = 0, \tag{5.100}$$

$$A\frac{j\omega\varepsilon_1}{u/a}J_m'(\frac{ur}{a}) - B\frac{j\beta}{(u/a)^2}\frac{m}{r}J_m(\frac{ur}{a}) + C\frac{j\omega\varepsilon_2}{w/a}K_m'(\frac{wr}{a}) - D\frac{j\beta}{(u/a)^2}\frac{m}{r}K_m(\frac{wr}{a}) = 0, \tag{5.101}$$

$$[M]\cdot\begin{bmatrix} A \\ B \\ C \\ D \end{bmatrix} = 0 \tag{5.102}$$

$$\begin{bmatrix} J_m(u) & 0 & -K_m(w) & 0 \\ 0 & J_m(u) & 0 & -K_m(w) \\ \frac{j\beta}{(u/a)^2}\frac{m}{r}J_m(\frac{ur}{a}) & -\frac{j\omega\mu_0}{u/a}J'_m(\frac{ur}{a}) & \frac{j\beta}{(w/a)^2}\frac{m}{r}K_m(\frac{wr}{a}) & -\frac{j\omega\mu_0}{w/a}K'_m(\frac{wr}{a}) \\ \frac{j\omega\varepsilon_1}{u/a}J'_m(\frac{ur}{a}) & -\frac{j\beta}{(u/a)^2}\frac{m}{r}J_m(\frac{ur}{a}) & \frac{j\omega\varepsilon_2}{w/a}K'_m(\frac{wr}{a}) & -\frac{j\beta}{(w/a)^2}\frac{m}{r}K_m(\frac{wr}{a}) \end{bmatrix} =$$

Using the same method in deriving Eq. 5.81 gives:

$$\left(\frac{J_m'(u)}{uJ_m(u)} + \frac{K_m'(w)}{wK_m(w)}\right)\cdot\left(\frac{n_1^2 J_m'(u)}{uJ_m(u)} + \frac{n_2^2 K_m'(w)}{wK_m(w)}\right) = m^2\left(\left(\frac{1}{u}\right)^2 + \left(\frac{1}{w}\right)^2\right)^2\cdot\left(\frac{\beta}{k}\right)^2, \tag{5.103}$$

Eq. 5.103 together with Eq. 5.56 and Eq. 5.63, are a transcendental function of β for each value of m. Here the integer m denotes the mode order, whereas the parameter β is the propagation constant of the hybrid mode, k stands for the wave number (defined for free space), and u and w are the arguments of the Bessel functions J_m and K_m.

Eq. 4.105 is widely quoted as the eigenvalue equation of the hybrid HE and EH modes, which is accurate for an all-dielectric waveguide, whether weakly guided or not [Tsao 1992]. In the circular waveguide, the solutions are separated into two classes. The two

classes in the solutions can be obtained by noting that Eq. 5.103 is quadratic in $J'_m(u)/uJ(u)$, and when we solve for this quantity, it will yield two different equations corresponding to the two roots of the quadratic equation. The eigenvalues resulting from these two equations yield the two classes of solutions that are designated conventionally as the EH and HE modes.

By solving Eq. 5.103 for $J'_m(u)/uJ(u)$, gives:

$$\frac{J'_m(u)}{uJ(u)} = \left(\frac{n_1^2+n_2^2}{2n_1^2}\right)\frac{K_m'(w)}{wK_m(w)} \pm \left[\left(\frac{n_1^2+n_2^2}{2n_1^2}\right)^2\left(\frac{K_m'(w)}{wK_m(w)}\right)^2 + \frac{m^2}{n_1^2}\left(\frac{\beta}{k}\right)^2\left(\frac{1}{w^2}+\frac{1}{u^2}\right)^2\right]^{\frac{1}{2}}, \tag{5.104}$$

Using the Bessel function relations:

$$J'_m(u) = -J_{m+1}(u) + \frac{m}{u}J_m(u), \tag{5.105}$$

Eq. 5.104 gives the formula for the EH modes:

$$\frac{J_{m+1}(u)}{uJ(u)} = \frac{n_1^2+n_2^2}{2n_1^2}\frac{K_m'(w)}{wK_m(w)} + \left\{\frac{m}{u^2} - \left[\left(\frac{n_1^2-n_2^2}{2n_1^2}\right)^2\left(\frac{K_m'(w)}{wK_m(w)}\right)^2 + \left(\frac{m\beta}{n_1k}\right)^2\left(\frac{1}{w^2}+\frac{1}{u^2}\right)^2\right]^{\frac{1}{2}}\right\}, \tag{5.106}$$

When the Bessel function relation is used

$$J'_m(u) = J_{m-1}(u) - \frac{m}{u}J_m(u), \tag{5.107}$$

The resulting HE modes are [after Yariv1997]:

$$\frac{J_{m-1}(u)}{uJ(u)} = -\frac{n_1^2+n_2^2}{2n_1^2}\frac{K_m'(w)}{wK_m(w)} + \left\{\frac{m}{u^2} - \left[\left(\frac{n_1^2-n_2^2}{2n_1^2}\right)^2\left(\frac{K_m'(w)}{wK_m(w)}\right)^2 + \left(\frac{m\beta}{n_1k}\right)^2\left(\frac{1}{w^2}+\frac{1}{u^2}\right)^2\right]^{\frac{1}{2}}\right\}, \tag{5.108}$$

For a given set of the parameters k_0, a_1, a_2, n_1, and n_2, the eigenvalue equation can be solved numerically to determine the propagation constant β. The factor β is the

z component of the wave propagation constant k and is the main parameter of interest in describing fibre modes (where the free-space wave number k is defined as $k = \omega / c = 2\pi / \lambda$, and λ is the vacuum wavelength of the optical field osillating at the frequency ω) [Agrawal 1997].

For guided modes β can only assume certain discrete values, which are determined from the requirement that the mode field satisfy Maxwell's equations and the electronic and magnetic field boundary conditions at the core -cladding interface [Keiser 1991].

A mode is uniquely determined by its propagation constant β. It is useful to introduce a quantity $n_{eff} = \beta / k$, called mode index or effective index and having the physical significance that each fibre mode propagates with an effective refractive index n_{eff} whose value lies in the range $n_1 > n_{eff} > n_2$. A mode ceases to be guided when $n_{eff} < n_2$. This can be understood by noting that the optical field of guided modes decays exponentially inside the cladding layer [Agrawal 1997].

Eq. 5.108 is evaluated using MATLAB graphical method to obtain the HE cladding modes and the result over HE cladding modes in the range $n_2 k < \beta < n_1 k$ are shown in Fig. 5.9.

The MATLAB codes used are given in Appendix 3.7-1.

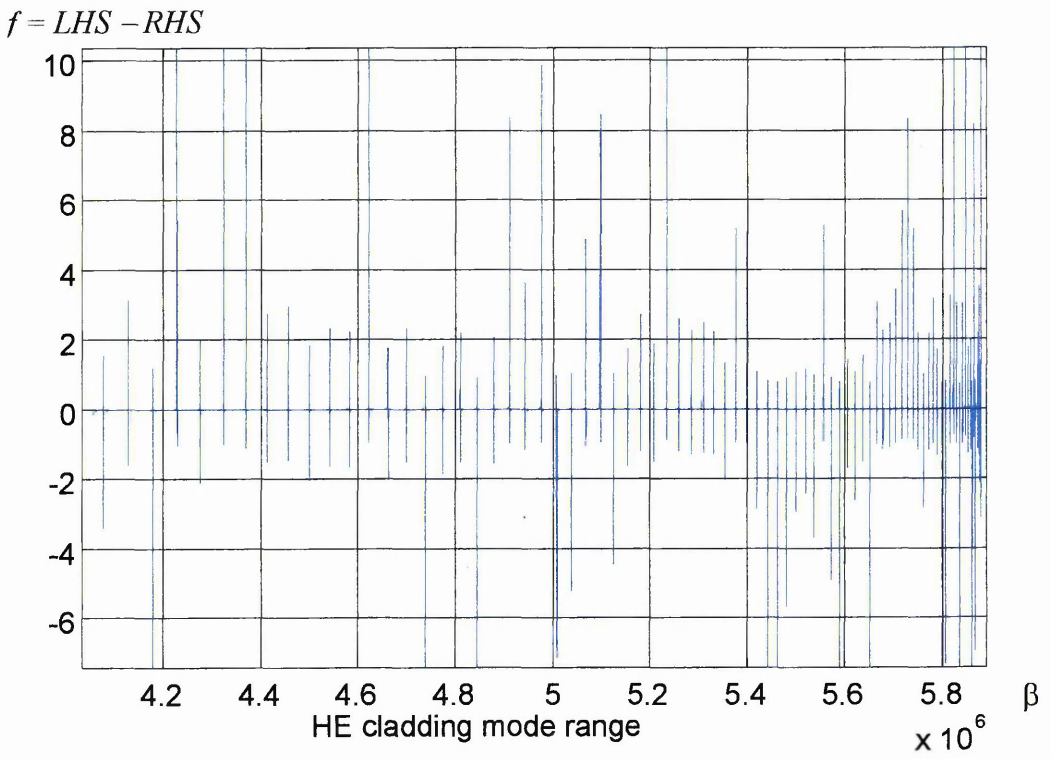

Fig. 5.9. A plot of Eq. 5.108 giving all the HE_{1m} cladding modes.

In LPG sensor most of the time, only the first eight modes are more useful to simulate the coupling wavelength. Fig. 5.10. shows the first eight HE cladding modes.

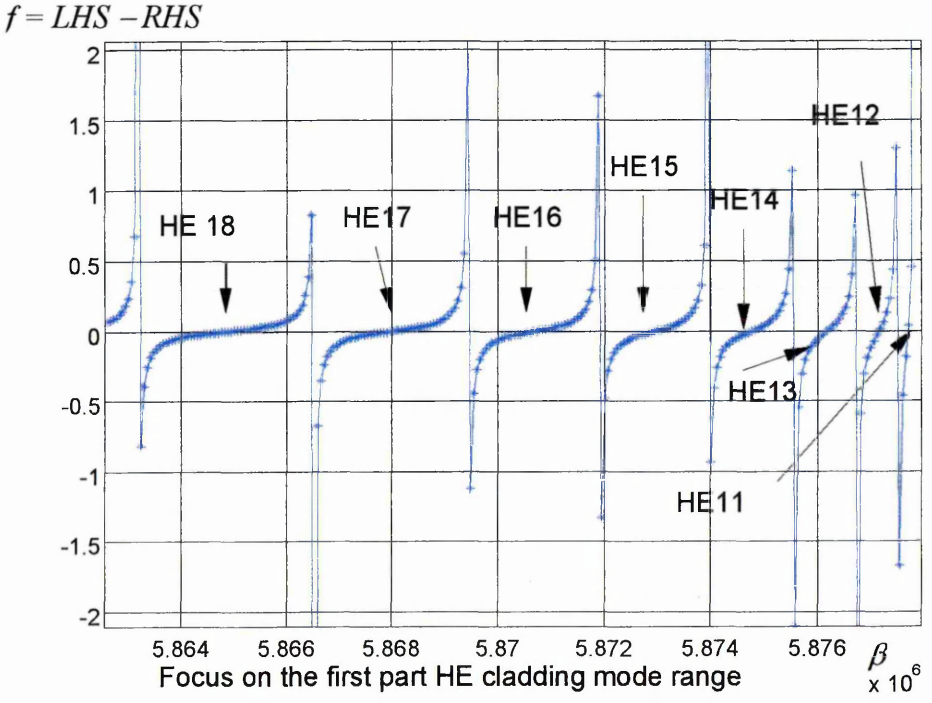

Fig. 5.10. A plot showing the first eight HE cladding modes

A more accurate but time consuming method to exactly determine the β values from the graph is by manually selecting the zero crossing points using the cursor, which the program include and utilising the 'Zoom in' (which gives greater resolution), 'format long' and 'ginput' commands to print these values on screen. It was noteworthy that the first zero crossing point from the right hand side of the graph gives the HE_{11} cladding mode, and the second gives the HE_{12} cladding mode, etc.

MATLAB is used to calculate the HE cladding mode values, as shown below.
HE1,1= 5877693.052145,
HE1,2= 5877157.562610,
HE1,3= 5876194.005741,
HE1,4= 5874801.976170,
HE1,5= 5872980.663165,
HE1,6= 5870729.661358,
HE1,7= 5868048.160015,
HE1,8= 5864935.753771,

The MATLAB codes used to calculate HE cladding mode values are given in Appendix 3.7-2.

5.2 Long-Period Grating Periodicity Prediction

In this section the method of long-period grating periodicity prediction has been presented. From the long-period grating phase matching equation, the relationship between grating periodicity and coupling wavelength can be plotted. Using this result the period required to couple a given wavelength λ can be predicted.

Now one can predict the wavelength at which the mode coupling will be enabled by a particular grating period. The LPG periodicity at different resonance wavelengths can be obtained according to the phase-matching condition given by Eq. 4.1

($\beta_{core} - \beta_{clad}^{(n)} = \frac{2\pi}{\Lambda}$) or Eq. 4.2 $\left(\lambda^{(n)}{}_i = \left(n_{core}(\lambda_i) - n_{clad}^{(n)}(\lambda_i)\right)\Lambda\right)$. Theoretical determination of the relationship between grating periodicity and wavelengths is explained as follows:

1). The first step involves the calculation of the propagation constants of the guided core mode and the various cladding modes of a fibre at a specific wavelength λ_i. Normally it could be sufficient to calculate only the first ten cladding modes.

2). Using the phase matching condition $\beta_{\text{core}}(\text{i}) - \beta_{clad}^{(n)}(i) = 2\pi / \Lambda$, a set of periods $\Lambda^{(n)}$ can be obtained, e.g. from first cladding mode we get the $\Lambda^{(1)}$, and from second cladding mode get $\Lambda^{(2)}$,etc.

3). Step 2 is repeated for several different resonance wavelengths, e.g. 1300 nm, 1400 nm and 1500 nm etc.

4). Using Excel package, the results of coupling wavelength versus LPG periodicity can be plotted as shown in Figs. 5.11 and 5.12.

The MATLAB codes are given in Appendix 3.8.

The fibre is described by the following parameters:

$n_1 = 1.458 + \Delta n/2 = 1.458 + (3.6\times10^{-4})/2$, $n_2 = 1.45$, $n_3 = 1.0$, $a_1 = 2.625$ μm,

$a_2 = 62.5$ μm.

$\Delta = (n_1 - n_2)/n_1 = 0.0055$,

Note: $\Delta n = 3.6\times10^{-4}$ is the peak induced-index change of the LPG.

The results of calculation also are given in Table 5.1 and 5.2.

Table 5.1: The relationship between the grating periodicities and resonance wavelengths (consider the peak induced-index change $\Delta n = 3.6\times10^{-4}$ in the core)

Wavelength, nm	1100	1200	1300	1400	1500	1600	1700
Period (mode 1), μm	262.95	320.41	390.59	476.822	583.4	715.688	880.587
Period (mode 2), μm	260.03	315.74	383.16	465.085	564.86	686.523	834.755
Period (mode 3), μm	257.82	312.07	377.15	455.282	548.97	660.866	793.458
Period (mode 4), μm	252.87	304.33	365.16	436.945	521.2	619.289	732.118
Period (mode 5), μm	249.55	298.86	356.34	422.916	499.17	585.166	680.094
Period (mode 6), μm	243.22	289.25	342	401.88	468.92	542.635	621.805
Period (mode 7), μm	238.75	282.06	330.7	384.515	442.81	504.249	566.822
Period (mode 8), μm	231.67	271.67	315.82	363.729	414.57	467.068	519.503
Period (mode 9), μm	226.13	263.01	302.66	344.299	386.69	428.258	467.134
Period (mode 10), μm	218.85	252.73	288.57	325.583	362.67	398.529	431.749
Period (mode 11), μm	212.4	242.94	274.24	305.302	334.91	361.786	384.751
Period (mode 12), μm	205.36	233.39	261.71	289.467	315.65	339.262	359.438
Period (mode 13), μm	198.18	222.86	246.87	269.306	289.23	305.842	318.591
Period (mode 14), μm	191.69	214.38	236.23	256.466	274.36	289.3	300.889

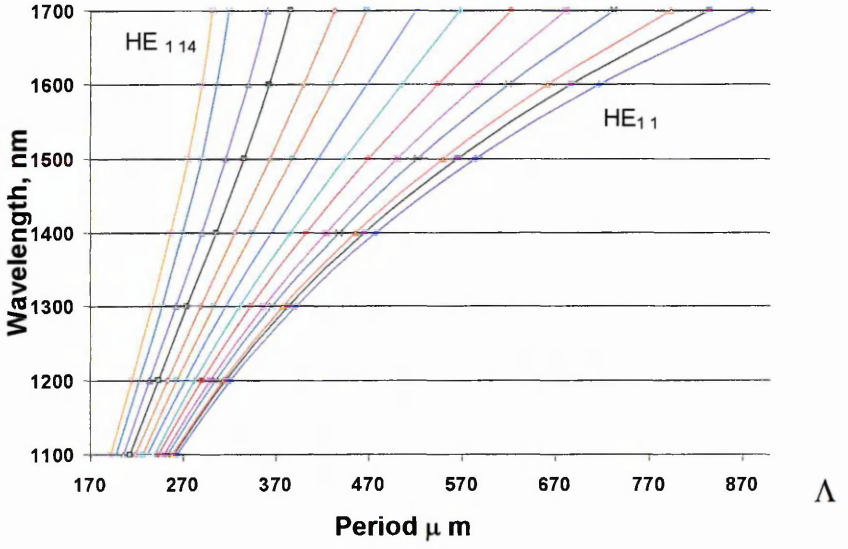

Fig. 5.11. Theoretical determination of the relationship between the grating periodicities and resonance wavelengths, considering the peak induced-index change in the core index.

Table 5.2: The relationship between the grating periodicities and resonance wavelengths (without considering the peak induced-index change in the core index)

Wavelength, nm	1100	1200	1300	1400	1500	1600	1700
Periods(mode 1), μm	272.45	332.74	406.58	497.612	610.46	751.003	926.736
Periods(mode 2), μm	269.33	327.71	398.56	484.843	590.22	718.999	876.178
Periods(mode 3), μm	266.95	323.74	392.02	474.153	572.84	690.734	830.498
Periods(mode 4), μm	261.66	315.43	379.12	454.34	542.72	645.593	763.788
Periods(mode 5), μm	258.08	309.54	369.59	439.131	518.75	608.396	706.955
Periods(mode 6), μm	251.33	299.26	354.21	416.548	486.27	562.725	644.502
Periods(mode 7), μm	246.54	291.53	342.05	397.823	458.08	521.306	585.241
Periods(mode 8), μm	239.01	280.48	326.21	375.702	428.07	481.876	535.251
Periods(mode 9), μm	233.1	271.22	312.12	354.891	398.25	440.428	479.476
Periods(mode 10), μm	225.4	260.34	297.22	335.144	372.96	409.276	442.587
Periods(mode 11), μm	218.53	249.91	281.96	313.581	343.5	370.384	393.032
Periods(mode 12), μm	211.12	239.85	268.8	297	323.42	347.018	366.918
Periods(mode 13), μm	203.49	228.7	253.09	275.705	295.59	311.938	324.203
Periods(mode 14), μm	196.69	219.82	241.98	262.362	280.21	294.914	306.105

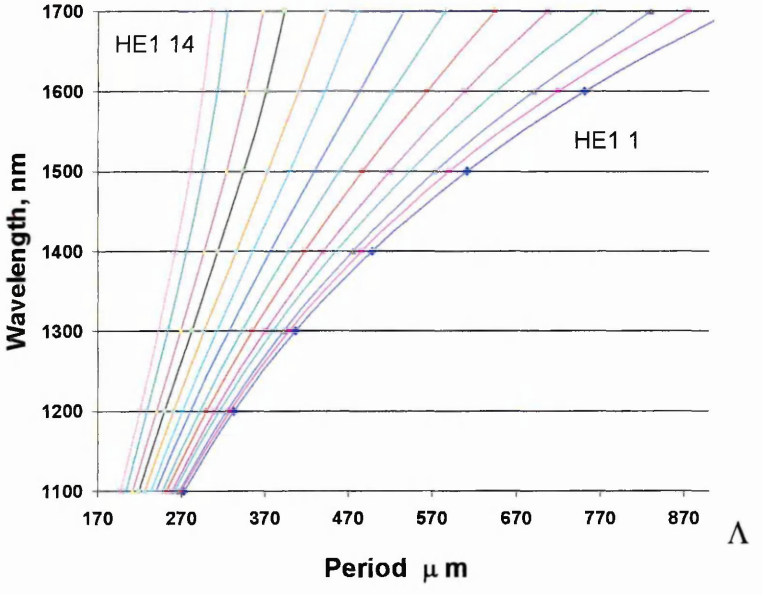

Fig. 5.12. Theoretical determination of the relations between grating periodicities and resonance wavelengths, without considering the peak induced-index change in the core index.

From Fig. 5.11 and 5.12 it can be seen that for a higher core refractive index, the period of LPG needs to be shorter for the same coupling wavelength. For the example given in Fig. 5.11 the core index is 1.45818, for the LPG to couple a wavelength of 1.5 μm, the required period is 499.17 μm. In Fig. 5.12 where the core index is 1.458, the required grating period is 518.75 μm in order to couple the same wavelength.

5.3. Modelling of Long-Period Grating Index Sensors

The long-period grating is a spectral loss element that couples light out of an optical fibre at a particular wavelength based on the grating period, fibre refractive index, and the refractive index of the surrounding environment. The LPG sensor is most sensitive when the refractive index of the surrounding ambient index is close to that of the cladding index. In practical uses, sometimes the refractive index of the surrounding medium is higher than that of the fibre cladding, for example in the chemical concentration sensor and some coating materials used for gas sensors. Thus it is necessary to develop a model to satisfy all possibilities.

5.3.1 LPG Index Sensors in the Literature

There have been a number of published work concerning index sensors in which the surrounding index (n_3) change has been considered but limited to values lower than the LPG cladding index (n_{cl}) [Bhatia 1996, Patrick *et al* 1998, Bhatia 1999].

The case for which $n_3 > n_{cl}$ is referred to as the leaky or hollow dielectrical waveguide [Marcuse 1991]. Previous work for a leaky dielectrical waveguide in a long period grating is summarized as follows:

1) Patrick and his co-works [Patrick, *et al* 1997] have first demonstrated chemical sensors based on a long-period fibre grating response to a change in n_3. They have measured the changes in the loss spectrum of an LPG when the index of refraction of the surrounding medium varied over a range of $n_3 = 1.00$ to 1.72. For $1.47 < n_3 < 1.72$ the transmission of the resonance λ decreased smoothly between the two spectra as shown in Fig. 5.13. They show that an LPG sensor based on this external refractive index response can be used to determine the concentration of antifreeze in water.

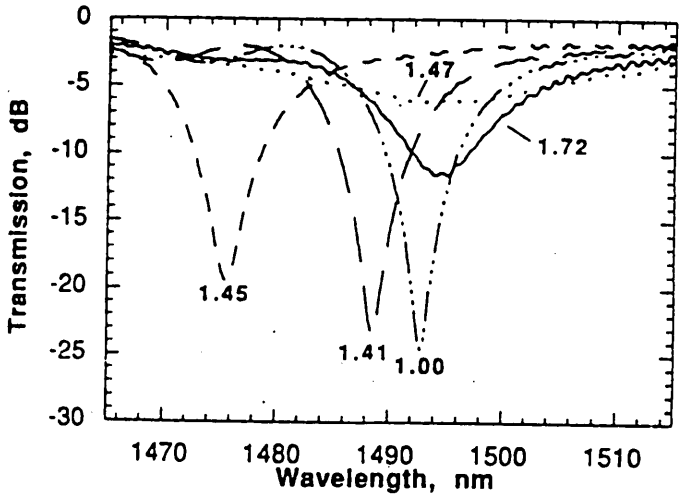

Fig. 5.13. Transmission spectrum of the fifth resonance λ measured for five values of n_3. The value of n_3 is indicated next to each line of the spectra [Patrick, et al 1997].

2) Lee and co-works [Lee *et al* 1997] have presented a graphical method for the analysis of the displacement of the resonant peaks of a long-period fibre grating induced by a change of ambient index. They stated that for ambient index near the refractive index of the cladding all modes disappear or weaken greatly. With an ambient index larger than the cladding index, the resonance peaks re-appear at wavelengths slightly longer than those measured in ambient air. The wavelength of the re-appearing peak has no further dependence on the ambient index.

3) In a paper entitled "Demonstration of long-period-grating efficient couplings with an external medium of a refractive index higher than that of silica". Duhem and co-works have discussed the experimental results of the LPG's response to different media of refractive index higher than that of silica [Duhem *et al* 1998]. They have evaluated the features of LPG's surrounded by several liquid media for several kinds of fibre. The study was focused on the determination of the coupling intensities in different types of fibre.

4) Stegall and Erdogan have published two papers, "Long-Period Fibre-Grating Devices Based on Leaky Cladding Mode Coupling"[Stegall and Erdogan 1997], and "Leaky Cladding Mode Propagation in Long-Period Fibre Grating Devices" [Stegall and Erdogan 1999]. They have investigated leaky-mode propagation of the cladding modes of an optical fibre through coupling with a long-period fibre grating [1999, 1997]. A one-dimensional ray propagation model was applied. Where the

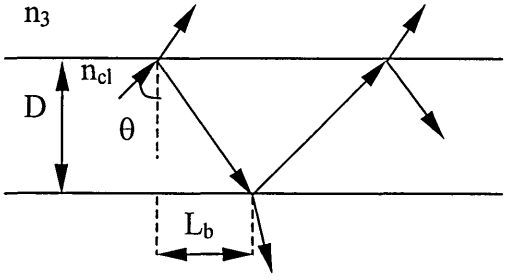

Fig. 5.14. Ray picture of leaky mode in a "hollow" dielectric waveguide [Stegall and Erdogan 1999].

leaky propagation can be approximated using a ray model in a one-dimensional (planar) waveguide, as depicted in Fig. 5.14. Since untitled, transversely uniform fibre gratings permit significant coupling to occur only between modes of the same azimuthal symmetry (here HE_{1v} and EH_{1v} which have a circularly symmetric intensity distribution), they were able to model these fairly accurately using a planar-waveguide

model of a single polarisation (here TE polarisation). The essence of this model is that the mode experiences Fresenel reflection at the interface between the cladding and the surrounding. For the leaky waveguiding situation, the dispersion relation no longer has purely real solutions. One way to determine the real portion of the mode propagation constants is to restrict the transverse propagation constants to correspond to constructive interference for a plane wave propagating down the waveguide. Mode-like propagation is then described by plane waves associated with the rays that have incident angles θ_m given by $\cos(\theta_m) = m\lambda / 2Dn_{cl}$, where m is as an integer, D is the waveguide width (corresponding to the fibre diameter).The associated transverse propagation constant β_m is then given by:

$$\beta_m = \sqrt{(n_{cl}k)^2 - \left(\frac{m\pi}{D}\right)^2}\ ,\ m = 1,2,3,\cdots. \tag{5.109}$$

where k is the free-space wave number.

As the ray bounces at the interface, some leak of the light occurs as described by the field reflection coefficient:

$$r = \frac{\cos(\theta) - \sqrt{\left(\frac{n_3}{n_{cl}}\right)^2 - \sin^2(\theta)}}{\cos(\theta) + \sqrt{\left(\frac{n_3}{n_{cl}}\right)^2 - \sin^2(\theta)}} \tag{5.110}$$

with θ being the angle of incidence.

An intuitive method for defining the loss that results from this leakage is to determine the distance L that the mode propagates before the power drops by a factor of $1/e^2$, yielding

$$L = -\frac{1}{2}\left(1 + \frac{1}{\ln|r|}\right)L_b \tag{5.111}$$

which is valid for $1/e < r < 1$. Here L_b is the longitudinal distance separating successive bounces, or $L_b = D\tan(\theta)$. The experimental measurements were compared to a transfer-matrix model to estimate the cladding mode losses. Losses are measured using an all-fibre Mach-Zehnder mode interferometer. Stegall and Erdogan [1999] stated that the measured losses are somewhat greater than predicted by the simple theory.

5) Duhem and co-workers [Duhem *et al* 2000] state that the resonant wavelength in leaky configuration is independent on the external index, and that the operation principles of a LPG sensor can only be based on the coupling intensity variations with the external index.

5.3.2 Methods of Modelling Long-Period Grating Index Sensor

This subsection focuses on the study of an LPG coupling wavelength shift when the surrounding index changes to values even greater than the cladding index. It presents a numerical method to calculate the leaky HE cladding modes, in which the results agree with the published experimental data.

The first step when modelling the refractive index sensors is to calculate the refractive index of the core and the refractive index of cladding, respectively. The core mode is not affected by the surrounding index change, so at a specific wavelength λ_i, the HE core mode is obtained by using Eq. 5.96. For HE_{11} core mode $m = 1$,

$u_1 = a_1\left(k^2 {n_{co}}^2 - \beta^2{}_{core}\right)^{1/2}$ is the normalized transverse phase constant in the core and

$w_1 = a_1\left(\beta^2{}_{core} - k^2 {n_{cl}}^2\right)^{1/2}$ is the normalized transverse attenuation constant in the core,

where $k = 2\pi / \lambda_i$, a_1 is the core radius and β_{core} is the propagation constant of the core

mode. The core effective index is obtained using $n_{core}(\lambda_i) = \frac{\beta_{core}}{k}$.

For calculation of the cladding modes, the standard multimode waveguide formula is used ignoring the effect of the core, treating the cladding as a core of multimode fibre and the ambient or coating material as a fibre cladding in the LPG region. Cladding modes classification are as follows:

5.3.2.1 Case 1: $n_3 < n_{cl}$

When $n_3 < n_{cl}$, this is a total internal reflection condition. The HE cladding mode expression is obtained from the well-known eigenvalue equation Eq. 5.108.

For HE_{1n} cladding modes, $m = 1$, where $u_2 = a_2\left(k^2 {n_{clad}}^2 - {\beta^2}_{clad}\right)^{1/2}$ is the normalized transverse phase constant of the cladding, $w_2 = a_2\left({\beta^2}_{clad} - k^2 {n_3}^2\right)^{1/2}$ is the normalized transverse attenuation constant, $v = ({u_2}^2 + {w_2}^2)^{1/2}$ is the normalized frequency and a_2 is the cladding radius. The cladding effective indices are obtained from the equation Eq. 5.112:

$$ {n^{(n)}}_{clad}(\lambda_i) = \frac{{\beta^{(n)}}_{clad}}{k}. \qquad (5.112) $$

5.3.2.2 Case 2: $n_3 \cong n_{cl}$

When the surrounding index is approximately equal to the cladding index $n_3 \cong n_{cl}$, the distinct loss bands disappear since the cladding modes get converted to radiation mode loss [Vikram and Vengsarkar 1996]. There are a few dB of broadband radiation-mode coupling losses, but no distinct resonance [Stegall 1999].

5.3.2.3 Case 2: $n_3 > n_{cl}$

For the case $n_3 > n_{cl}$, the cladding modes no longer experience total internal reflection and are referred to as leaky modes. Now we treat the fibre waveguide as a hollow circular dielectric waveguide, the cross-section of which is illustrated in Fig. 5.15. Here a_2 is the radius of the hollow guide (corresponding to the fibre cladding radius), n_{cl} is the hollow index (corresponding to the fibre cladding index) and n_3 is corresponding to the index of the surrounding medium or coating material.

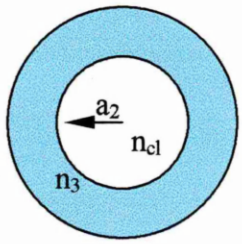

Fig. 5.15. Cross-section of a hollow circular waveguide where $n_3 > n_{cl}$

In this case Eq. 5.108 is still valid provided we take into consideration that the quantities β_{clad}, u_2, w_2 and v have complex values and the Bessel functions may have complex arguments [Adams 1981]. If the propagation constant β_{clad} becomes complex, then it is necessary to consider lossy or leaky modes. For complex β_{clad}, its real part β_r equals the phase velocity of the specified mode, whereas the imaginary part β_i represents its loss rate [Tsao 1992]. Using MATLAB, both graphical and numerical methods can calculate the real and imaginary parts of the propagation constant of the leaky cladding modes.

However, for circular waveguides, Adams [Adams 1981] has shown that, by making

certain approximations, β_{clad} can be expressed in terms of a real part and a power attenuation coefficient α as given by:

$$\beta_{clad} = \beta_r - \frac{i\alpha}{2} \tag{5.112}$$

where

$$\beta_r = kn_{cl}\left[1 - \frac{1}{2}\left(\frac{(l+0.25)\pi}{akn_{cl}}\right)^2\right] \tag{5.113}$$

and

$$\alpha \cong \frac{\left(n_3{}^2 + n_{cl}{}^2\right)}{akn_{cl}{}^3\sqrt{n_3{}^2 - n_{cl}{}^2}}\left(l + \frac{1}{4}\right)\pi \qquad \text{for HE modes} \tag{5.114}$$

where $l = 1,2,3,.....$

Typically in a single mode fibre, a long-period grating couples the fundamental core mode to a co-propagating cladding mode at coupling wavelengths given by Eq. 4.2. $\lambda_i^{(n)} = \left(n_{core}(\lambda_i) - n_{clad}{}^{(n)}(\lambda_i)\right)\Lambda$, where $\lambda_i^{(n)}$ is the n^{th} coupling wavelength, $n_{core}(\lambda_i)$ is the effective index of the core, $n_{clad}{}^{(n)}(\lambda_i)$ is the effective index of the n^{th} cladding mode and Λ is the pitch of the LPG period. It is clear from this equation that when n_3 changes, the propagation constant of cladding modes $\beta^{(n)}{}_{clad}$ and the effective refractive index of cladding modes $n_{clad}{}^{(n)}(\lambda_i)$, will change also, and as the $n_{clad}{}^{(n)}(\lambda_i)$ changes, the coupling wavelength $\lambda^{(n)}{}_i$ will shift. According to this theory the long-period grating index sensor can be modeled,

Eqs. 4.2, 5.96 and 5.108 are used to obtain a simulation results for the LPG resonance wavelength shift versus the surrounding refractive index. This is obtained for the 7^{th} cladding mode, as shown in Figs. 5.16 and 5.17. The parameters are: core index $n_1 = 1.458$, cladding index $n_2 = 1.45$, the core and cladding radii are 2.625 μm and

shift versus. the refractive index of the surrounding refractive is shown in Fig. 5.16. The MATLAB codes are given in Appendix 3.9.

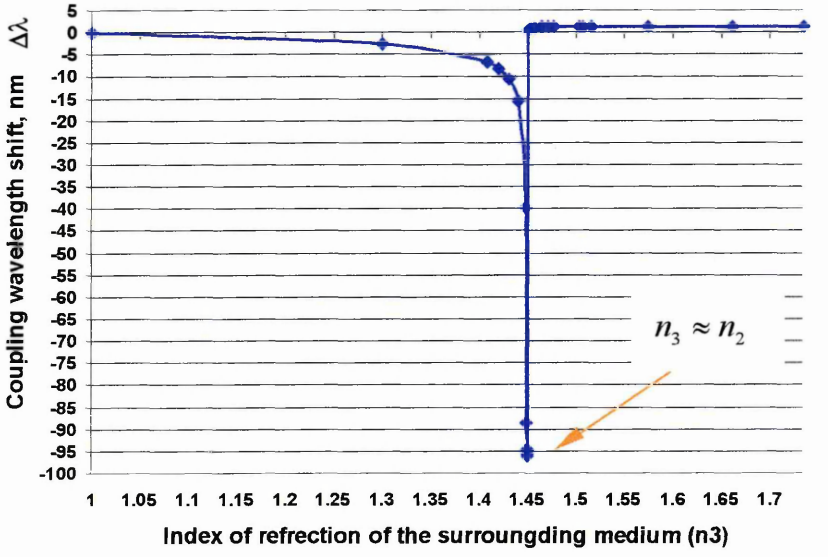

Fig. 5.16. Simulation results obtained for long-period grating coupling wavelength shift of the 7th resonance mode versus n_3 on a wide range of refractive index.

It can be seen from Fig. 5.16, for $n_3 > n_2$, the shift in coupling wavelength is large and negative, whereas at $n_3 \approx n_2$, the $\Delta\lambda$ is very large.

Fig. 5.16 shows that the very sensitive region occurs when n_3 is close to the cladding index n_{cl} and when the n_3 changes from 1.4499965 to 1.449997 (i.e. $\Delta n = 5 \times 10^{-7}$). The coupling wavelength shift shows a dramatic change from a sharp decrease to a value slightly higher than the coupling wavelength in air, with $\Delta\lambda$ values ranging from -96.10 nm to + 0.45 nm. The "switching properties" in this sensitive region have a potential application in the communications and sensor fields. When $n_3 > n_{cl}$, the leaky cladding modes coupling wavelengths are slightly longer than initial coupling wavelength when the index of surrounding material $n_3 = 1$ (in air). It was shown that when $n_3 > n_{cl}$, the theoretical leaky coupling wavelengths shift smoothly, but when n_3

is higher than a critical value which is around 1.486, the coupling wavelength is decreased. Fig. 5.17 shows the enlarged section of Fig. 5.16 for the range of index values $n_3 \geq 1.45$. When the surrounding index n_3 is higher than that of cladding ($n_3 > n_2$), the LPG coupling wavelength λ_i will experience a shift. For $n_3 = 1.7$, the shift in the wavelength is 1.3 nm as compared to the case when $n_3 = 1$. This spectral shift is very small but is still measurable using a spectrum analyser with sufficiently high resolution.

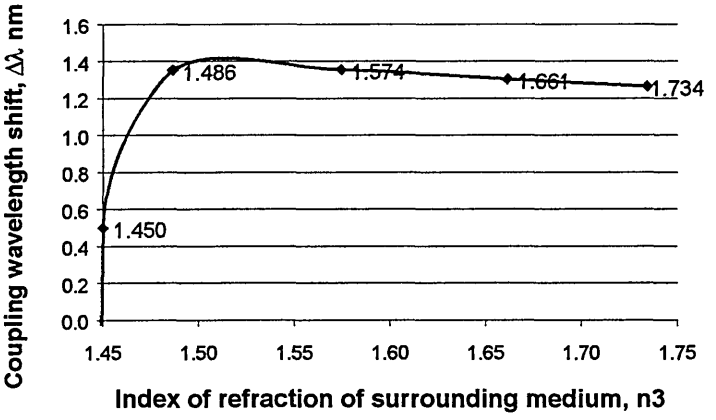

Fig. 5.17. Theoretical results revealing that when the surrounding index is higher than cladding index, the LPG resonance wavelength will still shift.

This result shows a good agreement with the experimentally measured data as shown in Fig. 5.18.

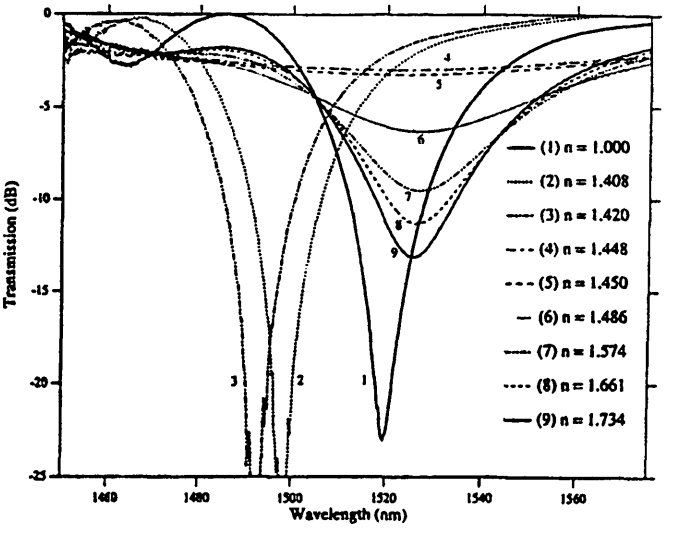

Fig. 5.18. Experimentally measured LPG transmission spectra for several surrounding indices [Stegall and Erdogan 1999].

The following is a flow chart, which shows the process of calculating the value of the wavelength shift when n_3 changes (using two layers HE cladding modes equation).

The parameters used are:

Flexcor 1060 Fibre data (Bhatia, 1996):

Difference in index of refraction Δ: 0.45 %,

Numerical aperture NA: 0.14,

Core radius: 2.5 μm and $n_2 = 1.45$,

Cladding diameter: 125 ± 2 and $n_1 = 1.45656937670071$,

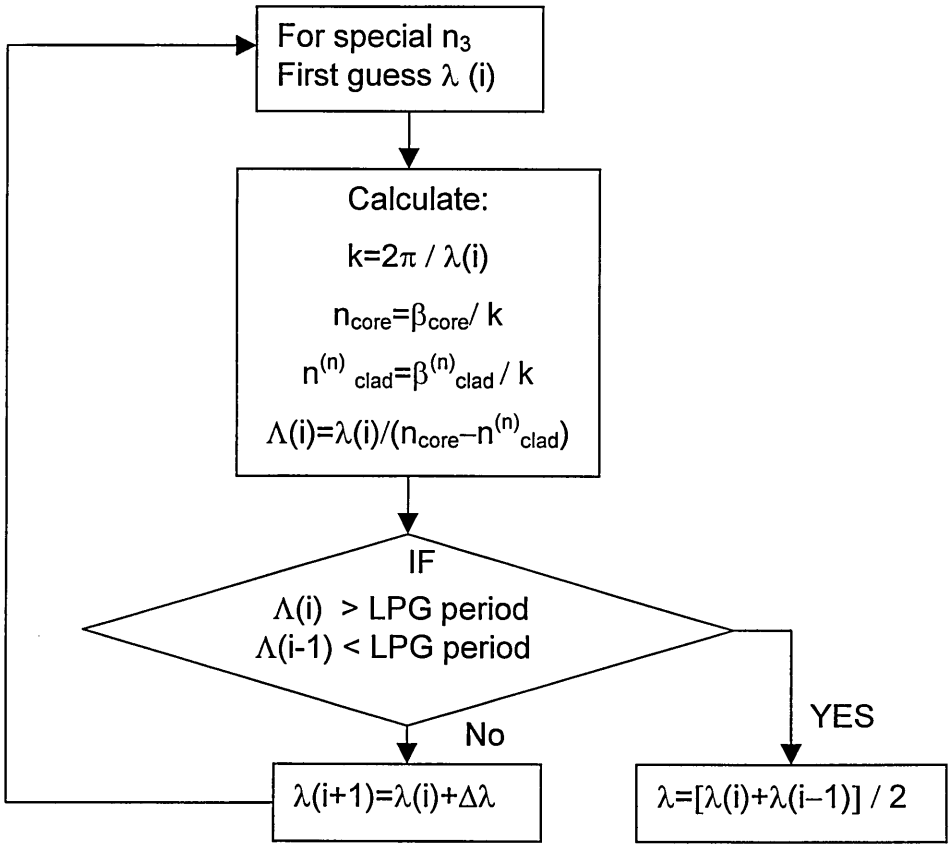

Fig. 5.19. A flow chart showing the calculation process associated with the modelling of LPG index sensor.

5.3.3 Results and Discussion

This section gives the detailed modelling method of the long period grating index

sensor. Using this model it is possible to simulate the long period grating coupling wavelength shift when the ambient index changes from 1 to 1.74 (see Fig. 5.16) and possibly higher values. These results reveal that when the surrounding index is higher than that of the LPG cladding, i.e., $n_3 > 1.45$, the coupling wavelength will still experience a measurable spectral shift. This is the first time that such results have been obtained through mathematical modelling, while previous literature has tackled the problem on an experimental basis only. Some published data also state that the wavelength has no further dependence on the ambient index when $n_3 > n_{cl}$ [Lee, *et al* 1997] and that the resonance wavelengths do not shift when the value of the external refractive index is changed [Duhem, *et al* 1998]. This new result can be applied to the modelling of chemical gas sensors, since in most gas sensors, the index of refraction of the coating material is higher than the cladding index.

For the same LPG sensor element the higher modes show greater coupling wavelength shifts than the lower modes, as Fig. 5.20 shows.

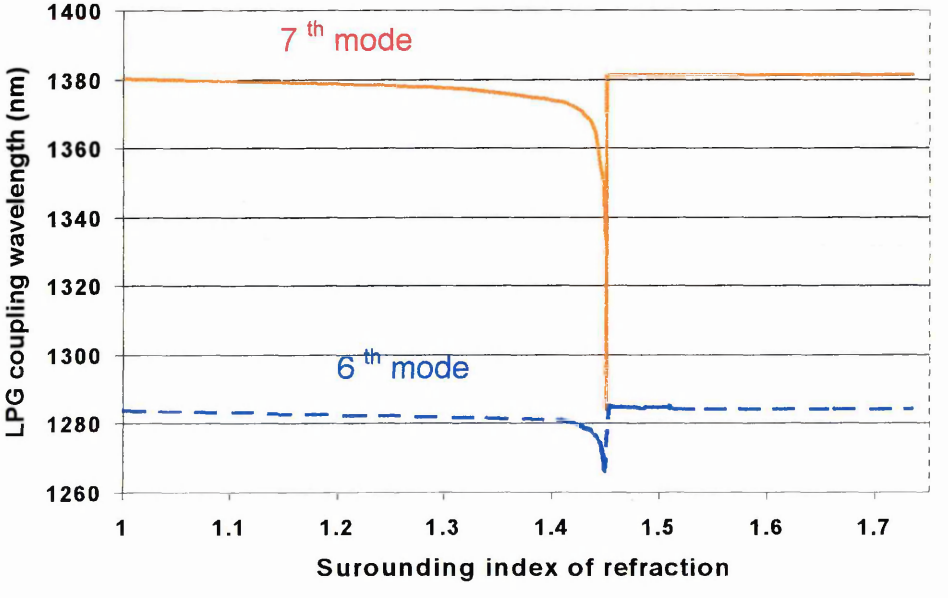

Fig. 5.20. LPG coupling wavelength shift as a function of the surrounding index of refraction, showing that the 7^{th} mode shift is larger than the 6^{th} mode shift.

From Fig. 5.21 it can be seen that the sensitivity $d\lambda / dn_3$ changes with the different refractive index values n_3. The 7^{th} mode (λ_7) is more sensitive than the 6^{th} mode (λ_6) when the surrounding index of refraction changes. This is due to the fact that the separation between higher mode values is larger than that between lower modes (see Fig. 5.10), thus when n_3 changes, the higher mode coupling wavelength shift is greater than that for the lower mode.

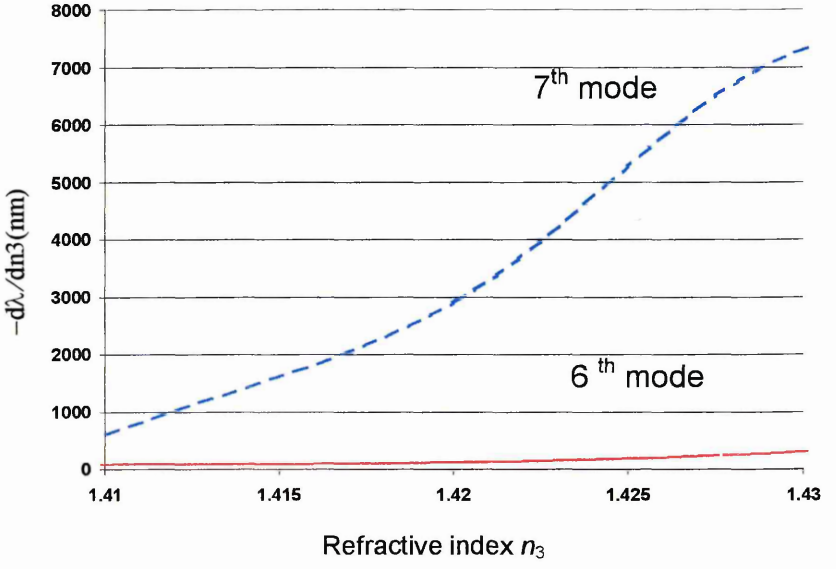

Fig. 5.21. Sensitivity $d\lambda / dn_3$ as a function of index of refraction n_3.

When $n_3 > n_{cl}$ the coupling wavelength shift for the higher mode is larger than that for the lower mode, a result that can be seen in Fig. 5.22.

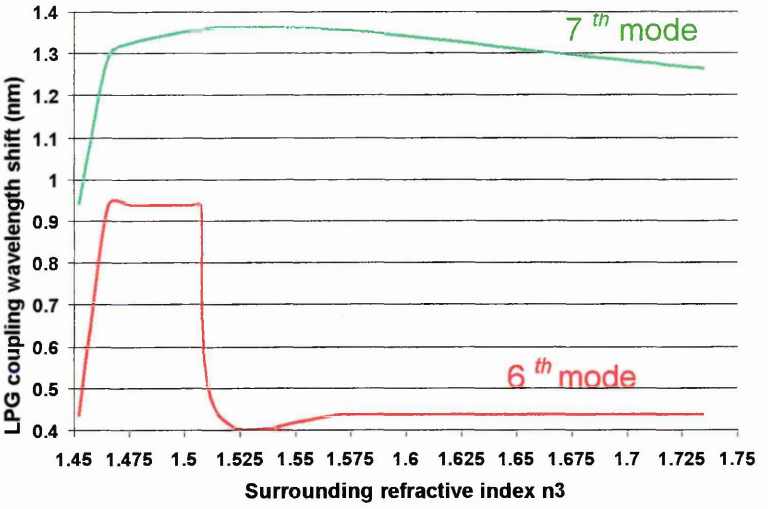

Fig. 5.22. A diagram showing that the 7^{th} mode coupling wavelength shift is larger than that of the 6^{th} mode.

5.4 Modelling of Long-Period Grating Gas Sensors

Since the refractive indices of all gases are smaller than that of the cladding, and are approximately equal to1, it was necessary to select affinity coating materials or polymer films to be coated onto the fibre cladding. As the coating absorbs target molecules, its index of refraction changes, causing a shift in the wavelength of the coupled light. This wavelength change is demodulated to determine the target gas concentration and enabling a real-time monitoring of the environmental conditions. For most coating materials, refractive index values are higher than that of the cladding ($n_3 > 1.45$).

5.4.1 Modelling of Toluene Gas Sensor Based on Long-Period Gratings

Most fibre grating-based sensors are used for strain and temperature sensing. Recently efforts has been focused on modelling novel sensors for gas detection based on long-

period fibre gratings, where the fibre cladding can be coated with an organic material that changes its refractive index on exposure to an external agent. The change in the coating refractive index will result in a change in the effective refractive index of the fibre cladding. This in turn will affect the higher order modes, which are travelling at the core-cladding interface. The effect would be a shift in the wavelength and amplitude of the transmission, especially in the higher order modes. This can be monitored by observing the transmission spectrum of the LPG. A mathematical modelling will be used in order to fully investigate this sensor.

The principle of operation of long period gratings when used as gas sensing elements is based on index of refraction changes of the coating material (n_3) due to adsorption of target gas molecules. As a result the cladding modes and coupling coefficients will change, with the former causing the attenuation bands to shift, while the latter results in different peak losses in the fibre transmission spectrum, as shown in Fig. 5.23.

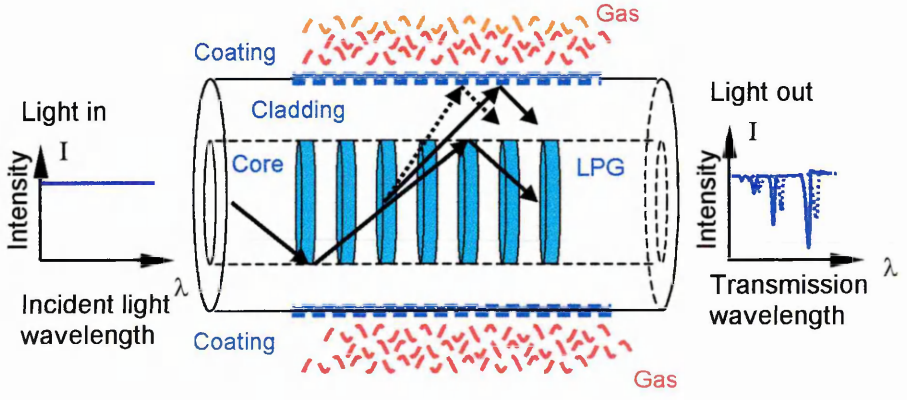

Fig. 5.23. Optical fibre long-period grating gas sensing element and the associated LPG transmission shift.

The most common air pollutants are NO_x, CO, SO_2, alkanes, and volatile organic compounds (e.g., benzene, toluene, and xylene) [Boisde' and Harner 1996].

The above model can be used to simulate the LPG gas sensor in which the coating material index is higher than that of the cladding. The coating material proposed to be used here is phosphorilated calix-4-resorcinarene (PC [4] RA) prepared by Langmuir-Blodgett (LB) method. This material has been the subject of refractive index measurements using surface plasmon resonance (SPR) technique and published recently by Nabok and co-workers [Nabok, *et al* 1997].

The values of both the thickness and the refractive index (n_{eff}) of PC [4] RA LB films are obtained by fitting the measured SPR curves to Fresnel reflection formula and are given in Table 5.3.

Table 5.3: Values of the thickness and effective refractive index (n_{eff}) of PC [4] RA LB films on exposure to toluene gas as obtained from SPR data fitting.

Number of LB layers	**Initial state n_{eff}**	**Post adsorption n_{eff}**	**Post recovery n_{eff}**
2 (Test1)	1.457	1.507	1.465
4 (Test2)	1.452	1.503	1.476
8 (Test3)	1.464	1.515	1.470
Mean values	1.458	1.508	1.470

The above data was used in this model to calculate the LPG coupling wavelength of the 7^{th} leaky mode shift, and the results are shown in Fig. 5.24.

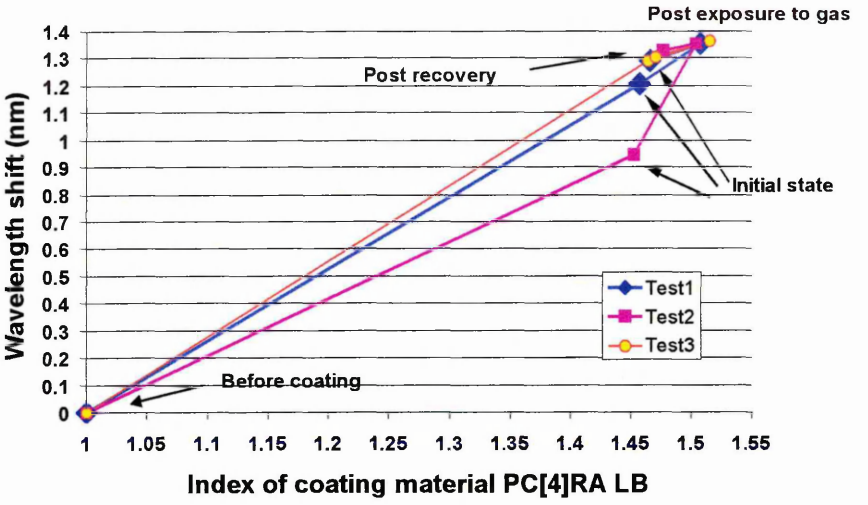

Fig. 5.24. Simulation results of the 7^{th} leaky mode shift when PC[4]RA LB films were exposed to toluene gas using test1, test 2 and test 3 data.

The data given in Table 5.3 shows that the index of refraction of the coating material is higher than that of the cladding (n_{cl}). However this method is capble of calculating the wavelength shift for each one of the given tests. The experimentally measured index changes of the coating material on expoure to toluene vapour is shown to agree well with those predicted by the current model.

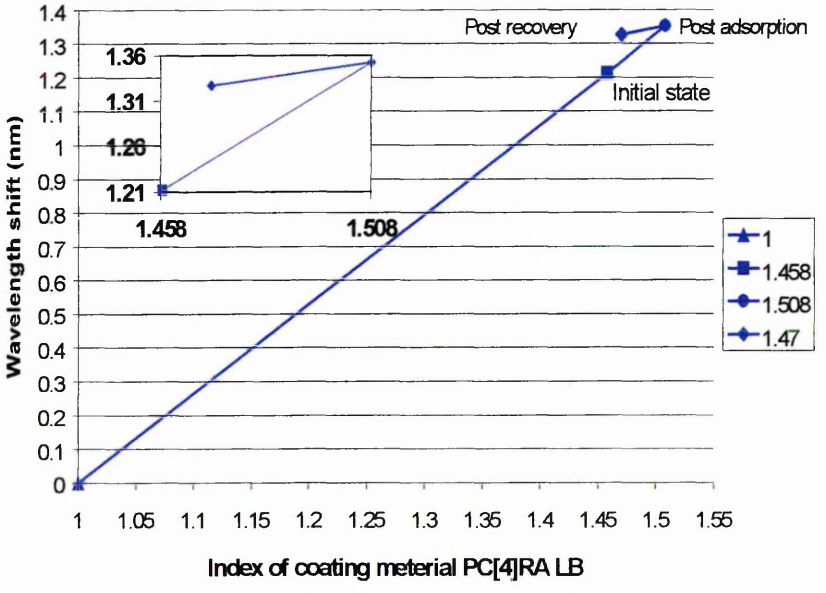

Fig. 5.25. Simulation results of the 7^{th} leaky mode shift when the PC[4]RA LB films were exposed to toluene vapour using mean values of Table 5.3 data. Coupling wavelength shift versus LB film index changes is further enlarged in the inset.

From Fig. 5.25, the obtained values of the wavelength shift appeared to be small (about $0.02-0.14\,nm$), but it can still be detected by using an optical spectrum analyser of sufficient resolution. Research is currently underway in order to perform coating of different materials for long-period grating gas sensors.

5.4.2 Modelling of NO_2 Gas Sensor Based on Long-Period Gratings

An optical sensor based on reflectometric measurements using polysiloxane with azo dye side-chains as the sensing layer for the detection of NO_2 gas, has been developed at the Centre for Molecular and Biomolecular Electronics (CMBE) in Coventry University. A value of index of refraction in air of about 1.575 has been found at wavelength $\lambda = 800\,nm$ (see Fig. 5.26).

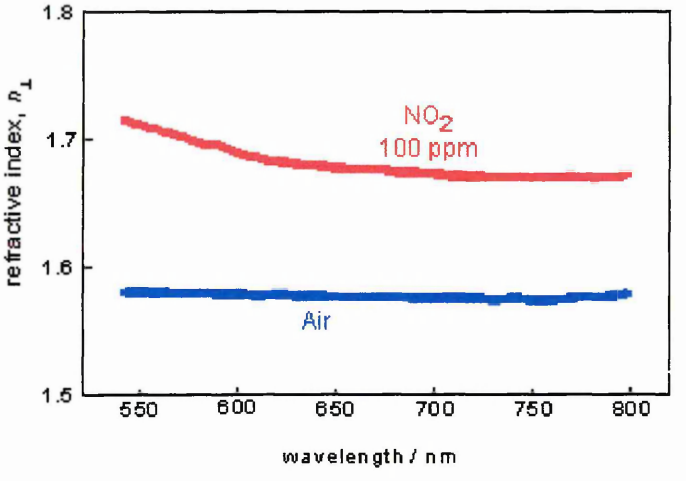

Fig. 5.26. Dispersion curves of refractive index for polysiloxane LB film with and without NO_2 [2000, URL: http://www.nes.cov.ac.uk/Research/CMBE/gassens.htm]

Employing the model developed for the LPG chemical sensor and by using the data from Fig. 5.26 for the surrounding refractive index n_3, the shift in the wavelength is simulated and the results are shown in Fig. 5.27. For an index change of 0.095, a resonance shift of about 0.1 nm can still be detected using spectrum analysers of high

resolution (see Fig. 5.27).

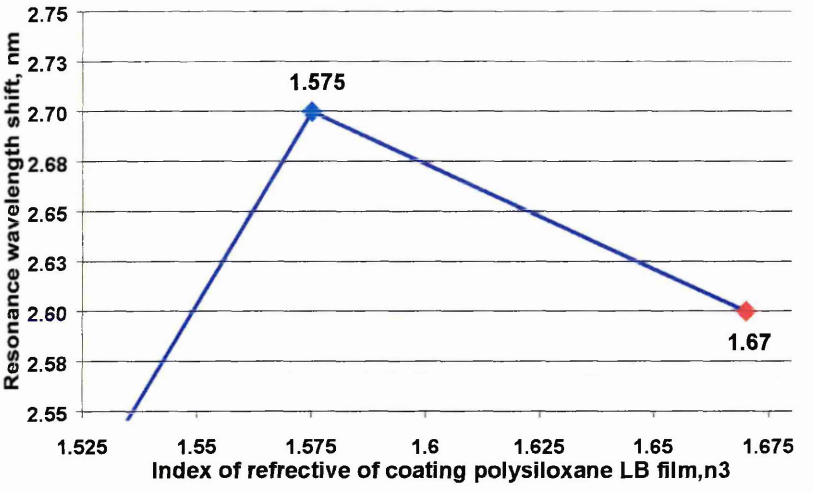

Fig. 5.27. Simulation results for an NO_2 gas sensor based on long-period gratings showing a coupling wavelength shift when the coating material is exposed to 100 ppm NO_2 gas.

The above two examples show that the model can be used to assist in the development of an environmental monitoring chemical sensor based on long-period gratings, with the chemical coating material refractive index being higher than that of the index of cladding (n_3).

5.4.3 Discussion of Simulation Results of LPG Gas Sensors

It has been shown that the developed model of long-period grating index sensor can be used to simulate gas sensors with different coating materials. Generally speaking, the shift in the higher mode-coupling wavelength is found to be greater than that for the lower modes when the ambient index n_3 changes. This is due to the fact that the separation between the higher mode values is larger than that between the lower modes, as was shown in Fig. 5.10. For example the shift of 7^{th} mode coupling wavelength is found to be larger than the calculated shift of the 6^{th} mode, as was shown in Fig. 5.20.

However, when the period of LPG is increasing, the lower mode-coupling wavelength shift $(\Delta\lambda)$ is found to increase when n_3 changes. This means that lower leaky modes such as the 6^{th} mode can still be employed to simulate a gas sensor, as demonstrated by the following example:

The calculation of the LPG coupling wavelength of the 6^{th} leaky mode demonstrates a wavelength shift of about 0.32 nm and 0.08 nm, for LPG fibre with grating periods of 570 μm and 290 μm, as shown in Figs. 5.28 and 5.29 respectively. From these results it can be seen that a fibre grating of the same characteristics but with different periods, will show a different degree of shift in the coupling wavelengths as a result of using the same coating material on exposure to the same analyte. In other words, the longer the period, the greater the shift of the wavelength (fibre data used are: $a_1=2.5\times10^{-6}$, $a_2=62.5\times10^{-6}$, $n_1=1.45657$, $n_{cl}=1.45$, and $\Lambda=570\,\mu m$ and $290\,\mu m$). From Fig. 5.28, it can be seen that the calculated values of the wavelength shift are small (about 0.32 nm – 0.19 nm). However such values can still be detected when an optical spectrum analyser of sufficient resolution (about 0.01 nm) is employed.

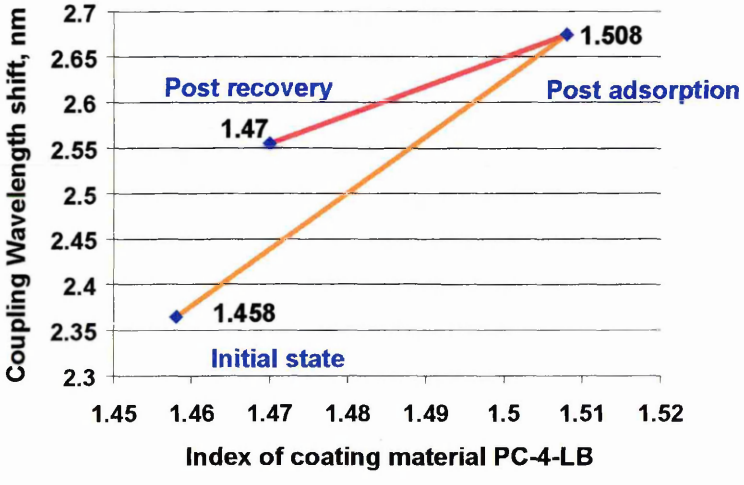

Fig. 5.28. Simulated results of the 6^{th} LPG coupling wavelength shift when PC[4]RA LB films are exposed to toluene vapour; period of grating is 570 μm.

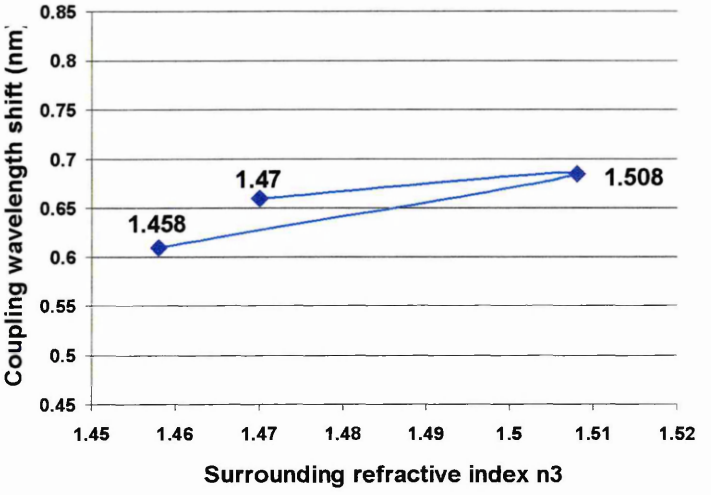

Fig. 5.29. Simulated 6^{th} LPG coupling wavelength shift when PC[4]RA LB films are exposed to toluene vapour; period of grating is 290 μm.

Figs. 5.28 and 5.29 show that when n_3 is slightly greater than n_{cl}, the coupling wavelengths will shift to longer values as n_3 increases.

5.5 Modelling of Long-Period Grating Transmission Spectrum as a Function of Surrounding Index of Refraction

When the surrounding index of refraction n_3 changes not only does the LPG coupling wavelength shift, but there is also a variation in the LPG transmission amplitude. This subsection will introduce a model for calculating the amplitude changes and plotting the LPG transmission spectra.

Erdogan introduced the equations to calculate the three layer cladding modes (considering the core, cladding and surrounding indices) which are expressed as [Erdogan 1997b]:

$$\xi_0 = \xi_0' \tag{5.115}$$

where

$$\xi_0 = \frac{1}{\sigma_2}\frac{u_2\left(JK + \frac{\sigma_1\sigma_2 u_{21}u_{32}}{n_2^{\,2}a_1a_2}\right)p_l(a_2) - Kq_l(a_2) + Jr_l(a_2) - \frac{1}{u_2}s_l(a_2)}{-u_2\left(\frac{u_{32}}{n_2^{\,2}a_2}J - \frac{u_{21}}{n_1^{\,2}a_1}K\right)p_l(a_2) + \frac{u_{32}}{n_1^{\,2}a_2}q_l(a_2) + \frac{u_{21}}{n_1^{\,2}a_1}r_l(a_2)} \tag{5.116}$$

$$\xi_0{}' = \sigma_1\frac{u_2\left(\frac{u_{32}}{a_2}J - \frac{n_3^{\,2}u_{21}}{n_2^{\,2}a_1}K\right)p_l(a_2) - \frac{u_{32}}{a_2}q_l(a_2) - \frac{u_{21}}{a_1}r_l(a_2)}{u_2\left(\frac{n_3^{\,2}}{n_2^{\,2}}JK + \frac{\sigma_1\sigma_2 u_{21}u_{32}}{n_2^{\,2}a_1a_2}\right)p_l(a_2) - \frac{n_3^{\,2}}{n_1^{\,2}}Kq_l(a_2) + Jr_l(a_2) - \frac{n_2^{\,2}}{n_1^{\,2}u_2}s_l(a_2)} \tag{5.117}$$

The following definitions have been used in Eqs. 5.116 – 5.117:

$$\sigma_1 \equiv i\,l\,n_{eff}/Z_0 \tag{5.118}$$

$$\sigma_2 \equiv i\,l\,n_{eff}Z_0 \tag{5.119}$$

$$Z_0 = \sqrt{\mu_0/\varepsilon_0} = 377\Omega \tag{5.120}$$

$$u_{21} \equiv \frac{1}{u_2^{\,2}} - \frac{1}{u_1^{\,2}}, \tag{5.121}$$

$$u_{32} \equiv \frac{1}{w_3^{\,2}} + \frac{1}{u_2^{\,2}}, \tag{5.122}$$

$$u_1^{\,2} \equiv (2\pi/\lambda)^2(n_1^{\,2} - n_{eff}^{\,2}), \tag{5.123}$$

$$u_2^{\,2} \equiv (2\pi/\lambda)^2(n_2^{\,2} - n_{eff}^{\,2}), \tag{5.124}$$

$$w_3^{\,2} \equiv (2\pi/\lambda)^2(n_{eff}^{\,2} - n_3^{\,2}), \tag{5.125}$$

$$J \equiv \frac{J_l'(u_1a_1)}{u_1J_l(u_1a_1)}, \tag{5.126}$$

$$K \equiv \frac{K_l'(w_3a_2)}{w_3K_l(w_3a_2)}, \tag{5.127}$$

$$p_l(r) \equiv J_l(u_2r)N_l(u_2a_1) - J_l(u_2a_1)N_l(u_2r), \tag{5.128}$$

$$q_l(r) \equiv J_l(u_2r)N_l'(u_2a_1) - J_l'(u_2a_1)N_l(u_2r), \tag{5.129}$$

$$r_l(r) \equiv J_l'(u_2r)N_l(u_2a_1) - J_l(u_2a_1)N_l'(u_2r), \tag{5.130}$$

$$s_l(r) \equiv J_l'(u_2 r)N_l'(u_2 a_1) - J_l'(u_2 a_1)N_l'(u_2 r)\,, \tag{5.131}$$

where l is an azimuthal number, J_l, Y_l denote the l^{th}-order Bessel functions of the first and second kinds respectively, and I_l and K_l denote the l^{th}-order modified Bessel functions of the first and second kinds, respectively.

The following are recursive relations governing Bessel and modified Bessel functions [Tsao 1992]:

$$J_{l+1}(u_i r) = -J'_l(u_i r) + (l/u_i r)J_l(u_i r), \tag{5.132}$$

$$J_{l-1}(u_i r) = J'_l(u_i r) + (l/u_i r)J_l(u_i r), \tag{5.133}$$

$$Y_{l+1}(u_i r) = -Y'_l(u_i r) + (l/u_i r)Y_l(u_i r,) \tag{5.134}$$

$$Y_{l-1}(u_i r) = J'_l(u_i r) + (l/u_i r)J_l(u_i r), \tag{5.135}$$

$$I_{l+1}(w_i r) = I'_l(w_i r) - (l/w_i r)I_l(w_i r), \tag{5.136}$$

$$I_{l-1}(w_i r) = I'_l(w_i r) + (l/w_i r)I_l(w_i r), \tag{5.137}$$

$$K_{l-1}(w_i r) = -K'_l(w_i r) - (l/w_i r)K_l(w_i r)\,, \tag{5.138}$$

$$K_{l+1}(w_i r) = -K'_l(u_i r) + (l/w_i r)K_l(w_i r), \tag{5.139}$$

Equation 5.117 for ξ_0' as appeared in Erdogan's article [Erdogan 1997, Eq. (7)] contains an error, as was confirmed by the author himself [E-mail from Prof. Erdogan of the University of Rochester, USA, and Dr. Allsop of Aston University, UK]. The last two terms in the numerator of the equation (Eq. 7 as appeared in Erdogan 1997] should be preceded by minus signs instead of positive signs.

Using the above cladding and core mode equations, the MATLAB model for calculating the coupling wavelength shift when surrounding index n_3 changes can be developed.

These MATLAB results show that when $n_3 = 1$, the coupling wavelength is $\lambda_5 = 1.5669\,\mu$m (core mode coupling to the 5^{th} cladding mode) and when $n_3 = 1.447$, the value of the coupling wavelength is $\lambda_5 = 1.539\,\mu$m. The specifications of the LPG fibre used are listed in Table 5.3.

Table 5.3 LPG fibre specifications

Parameter	Value
a core index	1.458
a cladding index	1.45
a value of peak induced-index change in the core	1×10^{-4}
core radius	2.625 μm
cladding radius	62.5 μm
a grating pitch	570 μm

The following equation is used to directly calculate the coupling constant [Erdogan 1997b]:

$$k_{1v-01}^{cl-co}(z) = \sigma(z)\frac{2\pi}{\lambda}\left(\frac{\pi b}{Z_0 n_2\sqrt{1+2b\Delta}}\right)^{1/2}\frac{n_1^{\,2}u_1}{u_1^{\,2}-V^2(1-b)/a_1^{\,2}}\left(1+\frac{\sigma_2\xi_0}{n_1^{\,2}}\right)E_{1v}^{\,cl}$$

$$\times\left[u_1J_1(u_1a_1)\frac{J_0(V\sqrt{1-b})}{J_1(V\sqrt{1-b})}-\frac{V\sqrt{1-b}}{a_1}J_0(u_1a_1)\right] \qquad (5.140)$$

where $E_{1v}^{\,cl}$ is the field normalization constant (for detailed calculation of $E_{1v}^{\,cl}$, see Erdogan 1997b). The coupling constant can be calculated for particular set of parameters. The total power (P) carried by the cladding mode is the sum of the power carried by the core (P_1), cladding (P_2) and the surrounding region (P_3), i.e., $P = P1 + P2 + P3 = 1W$. The results are shown in Fig. 5.30.

Equation 5.140 is used in the MATLAB code without the inclusion of its detailed derivation in this thesis. The following section shows the development of a model to

calculate and plot the LPG transmission amplitude changes for different values of ambient index (n_3).

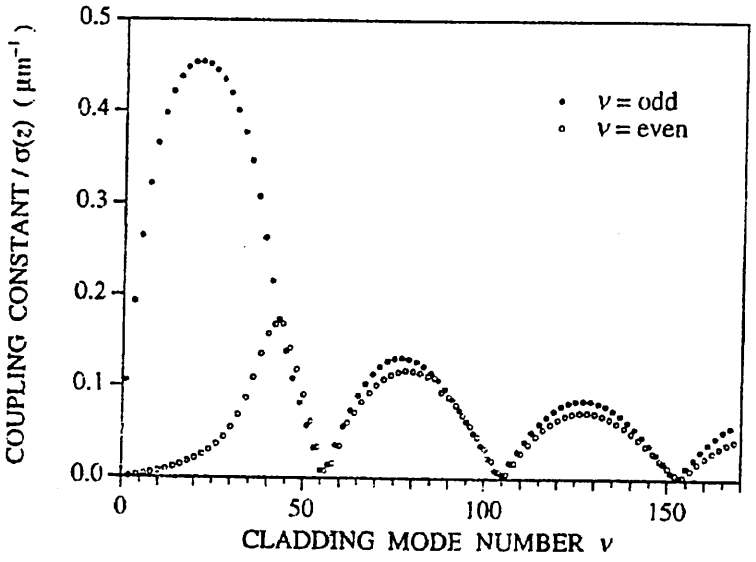

Fig. 5.30. Coupling constant $k_{1\nu-01}^{cl-co}$ divided by $\sigma(z)$ for the 168 cladding modes in a typical fibre, showing odd and even modes separately [Erdogan 1997 b].

The MATLAB code used to determine the coupling constant (Eq. 5.140) is given in Appendix 3.12. The parameters used are shown in Table 5.4

Table 5.4 Data used for LPG transmission spectrum calculation.

Parameter	Value
a core index	1.458
a cladding index	1.45
a value of peak induced-index change in the core	1×10^{-4}
core radius	2.625 μm
cladding radius	62.5 μm
a grating pitch	570 μm
For n_3	1
Coupling wavelength	1.5669 μm
Coupling constant $k_{1\nu-01}^{cl-co}(z)$	0.4725×10^{6}
For n_3	1.447
Coupling wavelength	1.539μm
Coupling constant $k_{1\nu-01}^{cl-co}(z)$	0.4262×10^{6}

Using the above data and Eq. 2.51 a plot of the LPG transmission spectrum for different values of n_3 is shown in Fig. 5.31. The MATLAB codes for the plots shown in Fig. 5.31. are given in Appendices10, 11 and 12.

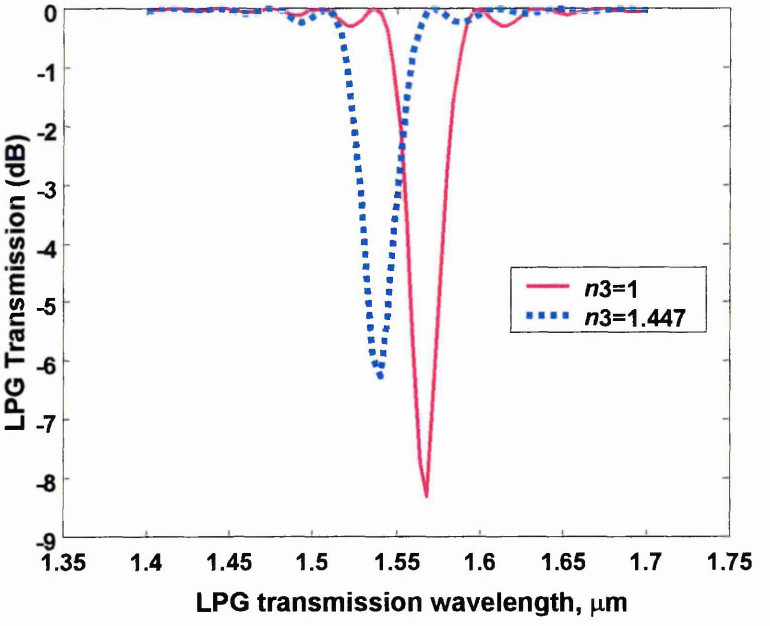

Fig. 5.31. Long-period grating transmission spectra which show that when surrounding index n_3 is changed, the coupling wavelength shifts, and the transmission amplitude also changes.

Figure 5.31 shows that when the surrounding index of refraction n_3 is increased without exceeding the cladding index (n_{cl}) value, the long-period grating coupling wavelength shifts to a shorter wavelength and the LPG transmission amplitude also decreases.

CHAPTER 6 CONCLUSION AND FUTURE WORK

6. 1 Conclusion

The main realisation of this project has been the establishment of a model for index sensors using the long-period fibre grating. This model can assist the development of LPG chemical concentration and gas sensors. This thesis has introduced the general fibre grating theory and also presented the recent fibre Bragg grating and long-period grating applications in the sensing and communications fields. Fibre grating sensors have many practical applications. This thesis focuses on temperature, strain and index sensing applications.

The historical development of the fibre Bragg grating has been introduced in Chapter 1, especially the long-period grating, and the recent progress made in its use in connection with applications for both sensing and communications.

In Chapter 2 the photosensitivity in fibre grating technology has been reviewed and the colour centres and permanent electric dipole models have been introduced and used to explain the physical mechanism behind photosensitivity. Three LPG fabrication methods, *viz.*, holographic interferometer, phase-mask and point by point, have been discussed and finally the diffraction grating principles have been discussed in order to give a better understanding of the fibre Bragg grating (short period grating) and long-period grating phenomena.

Recent applications of fibre Bragg grating in both sensing and communications fields have been the subject of Chapter 3. In the sensing field, temperature, strain, index of refraction and chemical sensing have been highlighted, whereas in communications

applications emphasis has been placed on fibre amplifiers, dispersion compensation, filters and wavelength division multiplexing.

Chapter 4 has mainly presented the development of long-period gratings in the field of sensors. It covered long-period grating temperature, axial strain and index of refraction sensors.

The foundations of modelling of LPG sensor theory is presented in Chapter 5, which included the propagation constants and effective indices of the fibre core and cladding equations, and utilising both graphical and numerical methods in details. The method of long-period grating periodicity prediction has been presented. It gives the detailed modelling method of the coupling wavelength calculation and the use of MATLAB codes for the long period grating index sensor. A flow chart for the calculation methods has also been given. Using this method it is possible to simulate the long period grating coupling wavelength shift when the ambient index changes over a wide range. It was demonstrated that even for surrounding index of refraction higher than that of the fibre cladding, the long-period grating sensor coupling wavelength will still shift and can be measured. These new results can be applied to the modelling of the chemical sensors, since in most cases, the index of refraction of the coating material is higher than the cladding index. Modelling and simulation of the long-period grating transmission spectrum and the effect of index of refraction changes have been discussed in a great detail. Using this method, the results have shown that attenuation bands did change when the surrounding index of refraction was lower than the fibre cladding refractive index.

The modelling results obtained throughout this thesis were compared with the reported work and have shown a close agreement. The model developed is viewed a powerful

tool in analysing and designing optical sensors based on long-period fibre gratings.

6. 2 Future Work

The work presented in this thesis has demonstrated the potential of long period fibre gratings (LPG) as sensing elements to determine changes in the surrounding ambient index of refraction, and can therefore be used as environmental monitoring system. The work, which is based on the mathematical modelling of the behaviour LPG-based sensing elements, has extended the range of operation of such a system by incorporating coating materials with index of refraction higher than that of the LPG cladding. It has been shown that LPG transmission spectral shift as well as variation in its intensity can be measured which reflects the index changes of the surrounding ambient.

The coupling constant k_{1v-01}^{cl-co} introduced in Eq. 5.140 has been restricted to the condition $n_3 < n_{cl}$. However, changes in LPG transmission attenuation bands have been found to be more sensitive than the LPG coupling wavelength shifts when $n_3 > n_{cl}$. Since the latter represents the condition found in most practical situations, it is therefore necessary to continue the development of models for simulating LPG index sensors which take into account coating materials with index of refraction higher than that of the cladding.

It is also noteworthy that the developed model only considers the changes in the index of refraction of the coated materials irrespective of its thickness. However it is desirable to further investigate how the refractive index changes with the thickness of the coating layers. The model can therefore be developed to take into account both the thickness and index of refraction of the coated materials and their corresponding effects on the LPG transmission spectrum.

REFERENCES

Adams, M. J., An Introduction to Optical Waveguides, John Wiley & Sons Inc., New York, 1981.

Agrawal, G. P., Nonlinear Fibre Optics Academic Press, San Diego, 1995.

Agrawal, G. P., Fibre -Optic Communication Systems, John Wiley & Sons Inc., New York, 1997.

Andreas, O. and Kalli, K., Fibre Bragg Gratings Fundamentals and Applications in Telecommunications and Sensing, ARTECH HOUSE, INC., 1999.

Archambault, J. L., Photorefractive Grating in Optical Fibres, Thesis of Doctor of Philosophy, Faculty of Engineering and Applied Science, Department of Electronics and Computer Science, University of Southampton, UK, Nov.1994.

Appell, D., Cladd, Fibre Detects Biological Agents Fast, *Laser Focus World,* Vol.34, pp.26-28, 1998.

Bethuys, S , Lablonde, L , Rivoallan, L , Bayon, JF , Brilland, L , and Delevaque, E., Optical Add/Drop Multiplexer Based on UV-Written Bragg Gratings in Twin-Core Fibre Mach-Zehnder Interferometer, *Electronics Letters,* Vol.34, pp.1250-1251, 1998.

Bhatia, V., Properties and Sensing Applications of Long-Period Gratings, Doctor of Philosophy, Virginia Polytechnic Institute and State University, USA. Nov.1996.

Bhatia, V. and Vengsarkar, A., Optical Fibre Long-Period Grating Sensors, *Optical Letters,* Vol.21, No.9, pp.692-694, 1996.

Bhatia, V., Campbell, D. K., Sherr, D., D'Alberto, T. G., Zabaronick, N. A., TenEyck, G. A., Murphy, K. A., and Claus, R. O., Temperature-Insensitive and Strain-Insensitive Long-Period Grating Sensors for Smart Structures, *Opt. Eng.* 36, 1872, 1997.

Bhatia, V., Applications of Long-Period Grating to Single and Multi-Parameter Sensing, *Optics Express,* Vol.4, No.11, pp.457-466, 1999.

Cohen, L. G. and Lin, C., *IEEE Journal of Quantum Electron.* QE-14, 347, 1978.

Davis, C. C., Lasers and Electro-Optics: Fundamentals and Engineering, Cambridge University Press, 1996.

Dianov, E. M., Abramov A. A., Bubnov M. M., Shipulin A. V., Prokhorov A. M., Semjonov S. L., and Schebunjaev, Demonstration of 1.3 μm Raman Fibre Amplifier Gain as 25 dB at a Pumping Power of 300 mW, *Opt. Fib Technol.* **1**, 236-238, 1995.

Duhem, O., Henninot, J. F., Warenghem, M. and Douay, M., Demonstration of Long-Period-Grating Efficient Couplings With an External Medium of a Refractive Index Higher than That of Silica, *Applied Optics,* Vol.37, No.31, pp.7223-7228, 1998.

Duhem, O., Henninot, J. F. and Douay, M., Study of in Fibre Mach-Zehnder Interferometer Based on Two Spaced 3-dB Long-period Gratings Surrounded by a Refractive Index Higher than That of Silica, *Optics Communications*, 180, pp.255-262, 2000.

Erdogan, T., Fibre Grating Spectra, *Journal of Lightwave Technology, Vol. No. pp.* 1997 a.

Erdogan, T., Cladding Mode Resonances in Short-and Long-Period Fibre Grating Filters, *Journal of the Optical Society of American,* Vol.14, No.8, 1997 b.

Eugene, H., Optic (Third Edition), Addison-Wesley, 1998.

Giles, C. R., Lightwave Applications of Fibre Bragg Gratings, *Journal of Lightwave Technology,* Vol.15, No.8, 1997.

Glass, A. M., The Photorefractive Effect, *Opt. Eng.*, 17, pp.470-479, 1978.

Gowar, J., Optical Communication Systems Prentice Hall International (UK) Ltd, London, 1993.

Grattan, K. T. V. and Sun, T., Fibre Optical Sensor Technology: An Overview, *Sensors and Actuators,* 82, pp.40-61, 2000.

Grubb, S. G., Erdogan, T., Mizrahi, T., Strasser, T., Cheung, W. Y., Reed, W. A., Lemarjire, P. J., Miller, A. E., Kosinski, S. G., Nukolak, G., and Becker, P. C., 1.3 μm Cascaded Raman Amplifier in Germanosolicate Fibres, in: Proc. of OAA'94, paper PD3, 1994.

Hahn, B. D., Essential MATLAB for Scientists and Engineers. John Wiley & Sons Inc., New York, 1997.

Hall, D. G., Theory of Waveguide and Devices, in: Integrated Optical Circuits and Components, L.D. Hutcheson, Ed. New York: Marcel-Dekker, 1987.

Hall, D.G., Selected Papers on Coupling-Mode Theory in Guided-Wave optics, SPIE Optical Engineering Press, 1993.

Hill, K. O., Fujii, Y., Johnson, D. C. and Kawasaki, B. S., Photosensitivity in Optical Fibre Waveguides: Application to Reflection Filter Fabrication, *Applied Physics Letters,* Vol.32, pp.647-649, 1978.

Hill, K. O. and Meltz, G., Fibre Bragg Grating Technology Fundamentals and Overview, *Journal of Lightwave Technology,* Vol.15, No.8, pp.1263-1276, 1997.

Hotate, K., Fibre Sensor Technology Today, *Optical Fibre Technology,* 3, pp.456-402, 1997.

Huang, H. C., Coupled Mode Theory as applied to microwave and optical transmission, VNU Science Press, 1986

Ibsen, M., Durkin, M. K., Cole, M. J., Zervas, M. N. and Laming, R. I., Recent Advantages in Long Dispersion Compensating Fibre Bragg Gratings, *IEE Electronics & Communications,* Colloquium, Optical Fibre Gratings, Aston University, UK., 1999.

Juma, S. K., Bragg Gratings Boost Data Transmission Rates, *Laser Focus World*, Nov. 1996.

Kartalopoulos, S. V., Introduction to DWDM technology Data in a Rainbow, 2000 Lucent Technology, 2000.

Kashyap, R., Fibre Bragg Gratings, Academic Press, London, 1999

Kersey, A. D., A Review of Recent Developments in Fibre Optical Sensor Technology, *Optical Fibre Technology,* 2, pp.291-317, 1996.

Kersey, A. D., Davis, M, A. Patrick, H, J. LeBlanc, M., Koo, K. P. Askins, C. G., Putnam, M. A. and Friebele. E. J., Fibre Grating Sensors, *Journal of Lightwave Technology,* Vol.15, No.8, pp.1442-1463, 1997.

Keiser, G., Optical Fibre Communications, McGraw-Hill Inc., Singapore, 1991.

Lee, B. H. Liu, Y., Lee, S. B. and Choi, S. S., Displacements of the Resonant Peaks of a Long-Period Fibre Grating induced by a Change of Ambient Refractive Index, *Optics Letters,* Vol.22, pp.1769-1771, 1997.

Lemaire, P. J., Atkins, R. M., Mizrahi, V. and Reed, W. A., High-Pressure H_2 Loading as a Technique for Achieving Ultrahigh UV Photosensitivity and Thermal Sensitivity in GeO_2 Doped Fibres, *Electronics Letters,* Vol.29, pp.1191-1193, 1993.

Marcuse, D., Theory of Dielectric Optical Waveguides, Bonston. M A. Academic, 1991.

Meltz, G., Morey, W. W. and Glenn, W. H., Formation of Bragg Gratings in Optical Fibres by a Transverse Holographic Methods, *Optics Letters*, Vol.14, pp.823-825, 1989.

Meltz, G., Hewlett, S. J., and Love, J. D., Fibre Grating Evanescent-Wave Sensors, Proc. SPIE, 2836, pp.342-350, 1996.

Morey, W. W, Meltz, G. and Glenn, W. H., Fibre Optic Bragg Grating Sensors Proc.SPIE, 1169, pp.98-107, 1998.

Nabok, A. V., Hassan, A. K., Ray, A. K., Omar, O. and Kalchenko, V. I., Study of Adsorption of Some Organic Molecules in Calix [4] resorcinolarene LB Films by Surface Plasmon Resonance, Sensors and Actuators B45, 1997.

Nutyt, R. J., Park, Y. K. and Gallion, P., Dispersion Equalization of a 10 Gb/s Repeater Transmission Systems Using Dispersion Compensating Fibre, *Journal of Lightwave Technology,* Vol.15, pp.31-42, 1997.

Okoshi, T., Optical Fibres, New York: Academic Press Inc., 1982.

Ohn, M. and Donohue J. E., Combating Dispersion Effects With Linearly Chirped Fibre Bragg Gratings, http://www.e-tek.com/products/article/article4.htm, Oct. 2000.

Onaka, H., 1.1 Tb/s WDM Transmission Over a 150km 1.3μm Zero-Dispersion Signal-Mode Fibre, in: Proc.OFC'96, San Jose, CA paper PD19, 1996.

Othonos, A. and Kalli, K., Fibre Bragg Gratings Fundamentals and Applications in Telecommunications and Sensing, Artech House Inc., 1999.

Patrick, H. J., Williams, G. M. Kersey, A. D., Pedrazzani, J. R., and Vengsarkar, A. M., Hybrid Fibre Bragg Grating/Long Period Fibre Grating Sensor for Strain/Temperature Discrimination, *IEEE Photonics Technology Letters,* Vol.8, No.9, 1996.

Patrick, H. J., Kersey, A. D. and Bucholtz, F., Ewing, K. J., Jukins, J. B. and Vengsarkar, A.M., Chemical Sensors Based on Long-Period Fibre Grating Response to Index of Refraction, presented at the *Conf. Lasers and Electro-Optics,*. Baltimore, MD, May paper CThQ5, pp420-421, 1997.

Patrick, H. J., Kersey, A. D. and Bucholtz, F., Analysis of the Response of Long Period Fibre Grating to External Index of Refraction, *Journal of lightwave technology*, Vol.16, No.9, 1998.

Rao, Y. J, Lobo Ribeiro, A. B., Jackson, D. A., Zhang, L., and Bennion, I., Combined Spatial-and Time-Division-Multiplexing Scheme for Fibre Grating Sensors with Drift-Compensated Phase-Sensitive Detection, *Optics letters*, Vol.20, pp.2149-2151, 1995.

Rao, Y. J., In-fibre Bragg Grating Sensors, Meas. *Sci. Technol.,* Vol.8, pp.355-375, 1997.

Rao, Y. J., Recent Progress in Applications of In-Fibre Bragg Grating Sensors, *Optical and Lasers in Engineering*, 31, pp.297-324, 1999.

Rastogi, P. K., Optical Measurement Techniques and Applications, Artech House Inc., Boston, 1997.

Saleh, B. E. A. and Teich, M. C., Fundamentals of Photonics, John Wiley & Sons Inc., 1991.

Stegall, D. B. and Erdogan, T., Leaky Cladding Mode propagation in Long-Period Fibre Grating Devices, *IEEE Photonics Technology Letters,* Vol.11, No.3, pp.343- 345, 1999.

Tolpegin, B., Long-Period Grating: Next Generation of Fibre Sensors, Photonics *Spectra,* Jan. 1997.

Tsao, C., Optical Fibre Waveguide Analysis, Oxford University Press, 1992.

Vengsarkar, A.M., Lemaire, P. J., Judkins, J. B, Bhatia, V., Erdogan, T. and Sipe, J. E., Long-Period Fibre Grating as Band-Rejection Filters, *Journal of Lightwave Technology,* Vol.14, No.1, pp.58-64, 1996.

Vengsarkar, A. M., Long-Period Fibre Grating Shape Optical Spectra, *Laser Focus World,* pp.243-248, June 1996.

Vengsarkar, A. M., Pedrazzani, J. R., Judkins, J. B and Lemaire, P. J., Long-Period Fibre-Grating -Based Gain Equalizers, *Optics Letters*, Vol.21, No.5, 1996.

Vries, M. D., Bhatia, V., Alberto, T. D., Arya, V. and Claus R. O., Photoinduced Grating-Based Optical Fibre Sensors for Structural Analysis and Control, *Engineering Structure,* Vol.20, No.3, pp.205-210, 1998.

Wangsness, R. K., Electromagnetic fields, John Wiley & Sons Inc., 1979.

Wysocki, P. F., Judkins, J. B., Espindola, R. P. and Andrejeo, M., Broad-Band Erbium-Doped Fibre Amplifier Flattened Beyond 40 nm Using Long-Period Grating Filter, *IEEE Photonics Technology Letters,* Vol.9, Num.10, pp.1343-1345, 1997.

Yariv, A., Coupling-Mode Theory for Guided-Wave Optics, *IEEE Journal of Quantum Electronics,* Vol.QE-9 (9), pp919-933, *1973.*

Yariv, A., Optical Electronics in Modern Communications, Oxford University Press, Oxford, 1997.

Zhang, Z., *Development of Optical Fibre Biosensors with Long Period Gratings,* Dissertation of Doctor of Philosophy. University of Maryland, USA, 1999.

Zyskind, J. L., Performance Issues in Optically Amplified Systems and Net Works, in: Proc. OFC'97, Dallas, TX, paper TuP1, 1997.

http://www.e-tek.com/products/dcompensators/dcompensators.html

http://www.nes.cov.ac.uk/Research/CMBE/gassens.html

http://www.o-eland.com/AmplitudeMasks.html

http://samsungelectronics.com/products/fibreoptics/d31.html

APPENDICES

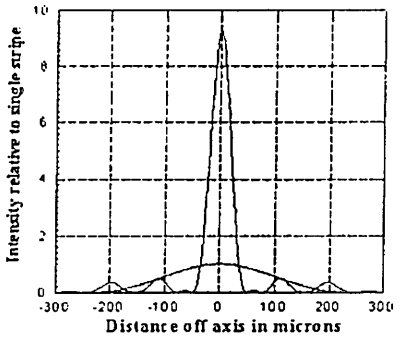

Figure 2 Curves showing relative intensities for n=1 and n=15 domain inverted $LiNbO_3$ transducers The total width of the n=1 stripe is 0 493 mm, the total width of the n=15 array is 2 692 mm. The focal length is 4 mm

Figure 2.

IT.2.4
Modelling of long period grating based fibre sensor

R Hou, Z Ghassemlooy, A K Hassan, A Nabok, K P Dowker
Sheffield Hallam University, UK

Long period gratings (LPGs) were first presented by Wengsarkar A.M. and co-workers in 1996 as band-rejection filters. Since then the LPG has been used as a novel fibre device in both telecommunications as a gain flattening and band rejection filter, and in the sensor field as temperature and strain sensor. A long period grating is a photoinduced periodic structure which, using UV exposure through an amplitude mask, is written in the core of communication fibre without removing the cladding. The fundamental guided mode propagating along the core is coupled into forward propagating cladding modes. These modes are very sensitive to the changes of the refractive index of the material surrounding the cladding. In this article a mathematical model of the LPG sensor has been developed. The model is based on Eigenvalue equations, coupled mode theory and other LPG related equations. Numerical simulation of the LPG transmission spectrum behaviour is studied when changing the ambient refractive index. Results show that the long period grating is very sensitive to surrounding index n3 changes, especially when n3 approaches the value of the cladding index. The associated graph functions display the shift of the attenuation bands to shorter wavelength as the surrounding index is increased from n3=1 (air) to n3=1.46 (near fibre cladding index). This mathematical model can be used to simulate different coating materials, which will change refractive index when they react with special target gas, and to assist the development of LPG based environmental monitoring sensors.

IT.2.5
Digital Synthetic-Heterodyne Detection of Dynamic Pressure in an Optical Fibre Cavity Sensor

M.J. Connelly, R. Kenny*, M. Whelan*
University of Limerick, Ireland
**ISIS, European Commission Joint Research Centre, Italy*

I. INTRODUCTION

Optical cavity sensors work on the principal of interferometric detection of the phase difference, caused by some external interest the sensor is used to measure dynamic pressure. A laser diode is used as the optical source. The laser bias current is modulated at a single frequency. The laser output is transmitted down an optical fibre to an external cavity. The fibre end is partially reflective so some of the light is reflected back down the fibre. The output light from the fibre is formed into a parallel beam by a lens and travels through free space for a short distance prior to reflection by a flexible membrane. The membrane has high reflectivity. As the membrane flexes the cavity length will vary and hence the phase difference between the reflected light waves. The intensity of the reflected light is a function of the phase difference. The reflected light travels back down the fibre where it is converted to an electrical signal by an optical receiver. The electrical signal is then processed to output a signal proportional to the dynamic pressure on the membrane. This type of sensor has many possible applications including a miniature surveillance microphone and a medical sensor to monitor breathing. The advantage of the sensor is that the sensor head is potentially replaceable. Its construction is simple with potentially low manufacturing cost. The laser, optical receiver and signal processing components can be located together in a unit remote from the sensor head. Various techniques exist for recovering a signal proportional to the dynamic pressure [1]. The Synthetic-Heterodyne technique is considered here [2-3]. It a powerful method for overcoming the interferometric fading problem. In this paper this technique is implemented on a digital signal processor and analysed with respect to noise and distortion. Experimental results are also presented.

II. DIGITAL IMPLEMENTATION AND EXPERIMENTAL RESULTS

The synthetic-heterodyne scheme can be implemented by analog circuitry or digitally. The digital method makes the scheme more amenable to control by computer. A practical system was constructed using a temperature stabilized DFB laser. The laser was biased to give an input power of 1 mW into the fibre. A bulk external cavity with a length of 10 cm was used. A mirror mounted on an accelerometer is used as the flexible membrane. For evaluation purposes, the accelerometer was driven by a sinusoidal voltage at 100 Hz to emulate a sinusoidal cavity displacement. A modulation current amplitude of 3.6 mA was required to give the optimum sensitivity for the cavity length used. The modulation current frequency was 2.4 kHz. A low-noise optical receiver was used to detect the return optical signal from the external cavity. The receiver signal is passed through an anti-aliasing filter, a DC blocking capacitor and amplified before acquisition and signal processing on a dSPACE DS1102 digital signal processing card. A schematic diagram of the digital implementation of the scheme is shown in Fig. 1. Signals on the dSPACE card can be displayed in real time on a personal computer. A/D and D/A converters with 12-bit resolution were used. The laser modulation current is obtained by passing a sinusoidal voltage generated by the DS1102 through a smoothing low-pass filter and a voltage-to-current converter. The acquired signal is shown in Fig. 2. The output phase signal from the dSPACE card is passed through a smoothing low-pass filter. A display of the detected phase signal (before D/A conversion) is shown in Fig. 2. The signal is, as expected, a sinusoid at 100 Hz. The waveform exhibits sharp jumps. This is due to quantisation effects inherent in the sampling process. This effect can be removed through the use of a soothing low-pass filter. The waveform also has a low-frequency drift component. This is probably due to thermal variations in the cavity and low- frequency ambient vibrations. Other frequencies within the detection bandwidth of 550 Hz, were successfully detected.

(Paper submitted to *Measurement Science and Technology,* 3 November 2000)

Modelling of Optical Fibre Long- Period Gating Sensors

Rujie Hou, Z.Ghassemlooy, Aseel Hassan, Alexei Nabok, Kenneth P. Dowker

Optical Communications Research Group, School of Engineering, Sheffield Hallam University Pond Street, S1 1WB, Sheffield U.K.

r.hou@shu.ac.uk, z.f.ghassemlooy@shu.ac.uk, a.hassan@shu.ac.uk, a.nabok@shu.ac.uk, k.p.dowker@shu.ac.uk

Abstract. In this article a mathematical model of optical fibre long-period grating (LPG) sensors has been developed. Numerical simulation of the LPG coupling wavelength behaviour is studied. Especially, we present the use of a hollow circular waveguide method to model the LPG coupling wavelength shift when the index of the surrounding material is higher than that of the cladding. This model can be used to simulate an LPG gas sensor.

Keywords: long-period grating, core mode, cladding mode, leaky mode, index sensors

1. Introduction

Long-period gratings (LPGs) were first presented by Vengsarkar and co-workers in1996 as band-rejection filters [12]. At the same time, it has been shown that the coupling wavelengths shift with the external refractive index change [13]. Since then the LPG has been used as a novel fibre device in both telecommunications as a gain flattening and band rejection filter, and in the sensor field as a temperature, strain and refractive index sensor.

An LPG is a photoinduced periodic structure which is written in the core of a communication fibre using UV exposure through an amplitude mask. The fundamental guided mode propagating along the core is coupled to the forward propagating cladding modes. These modes are very sensitive to changes in the refractive index of the surrounding material; especially when the index is close to the cladding index.

Since the refractive indices of all gases are much less than that of the cladding, and in order to develop a gas sensor, it is necessary to find a thin polymer film which is coated on the fibre cladding. The refractive index of the coated film will change due to the absorption of target gas molecules. However, the refractive indices of most coating materials are higher than the fibre cladding index (1.45). Therefore it is necessary to develop a model that can to satisfy each case.

The case where the ambient index of refraction (n_3) is higher then the cladding index (n_{cl}) is referred to as a leaky or hollow dielectrical waveguide [5]. In previous works using the leaky waveguide formula in LPGs are: Patrick and co-workers demonstrated chemical sensors based on an LPG response to external refractive index, using index oil with on index of refraction ranging from 1.40 to 1.72 [8]. Lee and co-workers presented a graphical method for the analysis of the displacement of the resonant peaks of the LPG by a change of ambient index [4]. Duhem and co-workers experimental study of the LPG's response to different media of refractive index higher than that of silica,

focused on determining the coupling intensities in different types of fibre [2]. Stegall and Erdogan estimate the cladding mode losses by using a one-dimensional (planar) waveguide approximation [10].

The present work introduces a method of modelling LPG sensors and presents a numerical method to calculate the leaky HE cladding modes. In developing this model the core, cladding and surrounding material dispersion effects have been ignored for the sake of simplicity. The LPG coupling wavelength shift is then examined when the surrounding index is larger than that of the cladding. Finally a numerical example of the simulated an LPG gas sensor is given.

2. Theory

2.1. Optical fibre long-period grating (LPG)

Typically in a single mode fibre, an LPG couples the fundamental core mode to a co-propagating cladding mode at a coupling wavelength give by [9]

$$\lambda^{(n)}{}_i = \left(n_{core}(\lambda_i) - n_{clad}{}^{(n)}(\lambda_i)\right)\Lambda \tag{1}$$

where $\lambda^{(n)}{}_i$ is the nth coupling wavelengths, $n_{core}(\lambda_i)$ is the effective index of the core , $n_{clad}{}^{(n)}(\lambda_i)$ is the effective index of the nth cladding mode and Λ is the pitch of the LPG period.

2.2. Core mode

The core mode is not affected by the surrounding index change, so at a specific wavelength λ_i the HE core mode is obtained using Eq.2 [6]

$$u_1 \frac{J_m(u_1)}{J_{m-1}(u_1)} = w_1 \frac{K_m(w_1)}{K_{m-1}(w_1)} \tag{2}$$

For HE_{11} core mode $m = 1$, $u_1 = a_1\left(k^2 n_{co}{}^2 - \beta^2{}_{core}\right)^{1/2}$ is the normalized transverse phase constant and $w_1 = a_1\left(\beta^2{}_{core} - k^2 n_{cl}{}^2\right)^{1/2}$ is the normalized transverse attenuation constant in core, where $k = 2\pi / \lambda_i$, a_1 is the core radius and β_{core} is the propagation constant of core mode. The core effective index is obtained using Eq.3.

$$n_{core}(\lambda_i) = \frac{\beta_{core}}{k} \tag{3}$$

2.3. Cladding mode

When calculating the cladding modes the two layer standard multimode waveguide formula is used ignoring the effect of the core, treating the cladding as a core of multimode fibre and the ambient or coating material as a fibre cladding in the LPG region.

Cladding modes classification:

2.3.1. Case 1: $n_3 < n_{cl}$

When $n_3 < n_{cl}$, this is a total internal reflection condition. From the well-known eigenvalue equation, obtained an HE cladding mode expression is obtained [14]:

$$\frac{J_{m-1}(u_2)}{u_2 J_m(u_2)} = -\frac{(n_{cl}^2 + n_3^2)K_m'(w_2)}{2n_{cl}^2 w_2 K_m(w_2)} + \left\{ \frac{m}{u_2^2} - \left[\left(\frac{(n_3^2 - n_{cl}^2)K_m'(w_2)}{2n_{cl}^2 w_2 K_m(w_2)} \right)^2 + \left(\frac{mv^2 \beta_{clad}}{u_2^2 w_2^2 n_{co} k} \right)^2 \right]^{\frac{1}{2}} \right\} \quad (4)$$

For HE_{1n} cladding modes, $m = 1$, where $u_2 = a_2\left(k^2 n_{clad}^2 - \beta^2_{clad}\right)^{1/2}$ is the normalized transverse phase constant, $w_2 = a_2\left(\beta^2_{clad} - k^2 n_3^2\right)^{1/2}$ is the normalized transverse attenuation constant in cladding region, $v = (u_2^2 + w_2^2)^{1/2}$ is the normalized frequency and a_2 is the cladding radius. The cladding effective indices are obtained from the following Eq.5.

$$n^{(n)}{}_{clad}(\lambda_i) = \frac{\beta^{(n)}{}_{clad}}{k} \quad (5)$$

2.3.2. Case 2: $n_3 \cong n_{cl}$

When the surrounding index is approximately equal to the cladding index, the distinct loss bands disappear since the cladding modes get converted to radiation mode loss [13]. There are a few dB of broadband radiation-mode coupling losses, but no distinct resonance [10].

2.3.3. Case3: $n_3 > n_{cl}$

For the case $n_3 > n_{cl}$, the cladding modes no longer experience total internal reflection and are referred to as leaky modes. Now the fibre waveguide is treated as a hollow circular dielectric waveguide, the cross-section of which is illustrated in Figure1, where a_2 is the radius of the hollow guide (corresponding to the fibre cladding radius), the hollow index is n_{cl} (corresponding to the fibre cladding index) and n_3 is corresponding to the index of surrounding medium or coating material.

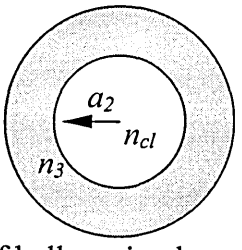

Figure 1. Cross-section of hollow circular waveguide where $n_3 > n_{cl}$

In this case Eq.5 is still valid provided we take into consideration that the quantities $\beta_{clad}, u_2, w_2, v$ have complex values and the Bessel functions may have complex arguments [1]. If the propagation constant β_{clad} becomes complex, then it is necessary to consider lossy or leaky modes. For complex β_{clad}, its real part β_r equals the phase velocity of the specified mode, whereas the imaginary part β_i represents its loss rate [11]. Using MATLAB, both graphical and numerical method can calculate the real and imaginary parts of propagation constant of leaky cladding modes.

However, for circular waveguides, Adams [1] has shown that, by making certain approximations, β_{clad} can be expressed in terms of its real part and power attenuation coefficient α as given by:

$$\beta_{clad} = \beta_r - \frac{i\alpha}{2} \tag{6}$$

where

$$\beta_r = kn_{cl}\left[1 - \frac{1}{2}\left(\frac{(l+0.25)\pi}{akn_{cl}}\right)^2\right] \tag{7}$$

$$\alpha \cong \frac{\left(n_3^{\,2} + n_{cl}^{\,2}\right)}{akn_{cl}^{\,3}\sqrt{n_3^{\,2} - n_{cl}^{\,2}}}\left(l + \frac{1}{4}\right)\pi \qquad \text{for HE modes} \tag{8}$$

where $l = 1,2,3,.....$

3. Modelling results and discussion

From Eqs.1 to 5 it can be seen that by changing the surround index (n_3) to be higher than that of cladding, the LPG coupling wavelength $\lambda_i(i)$ will experience a shift. For $n_3 = 1.7$ the shift in the wavelength $\Delta\lambda \approx 2.5$ nm as compared to the case when $n_3 = 1$. This spectral shift is very small but is still measurable using a spectrum analyser.

Eqs.1 to 5 are used to obtain simulation results for the LPG resonance wavelength shift versus the surrounding refractive index. This is obtained for the *7th* order cladding mode, as shown in Figure 2. The parameters used are; core index n_1=1.458, cladding index n_2=1.45, the core and cladding radii are 2.625 μm and 62.5 μm, respectively, and the pitch of the grating is 290 μm.

Figure 2 shows that the very sensitive region occurs when n_3 is close to n_{cl} and when the n_3 changes from 1.4499965 to 1.449997(i.e. $\Delta n = 5\times10^{-7}$), the coupling wavelength shift shows a dramatic change from a sharp decrease to a sharp increase, with values from -96.10 nm to +0.45 nm. The "switch properties" in this sensitive region have a potential application in the communications and sensor fields. When $n_3 > n_{cl}$, the leaky

cladding modes coupling wavelengths are slightly longer than initial coupling wavelength when the index of surrounding material $n_3 = 1$(in air).

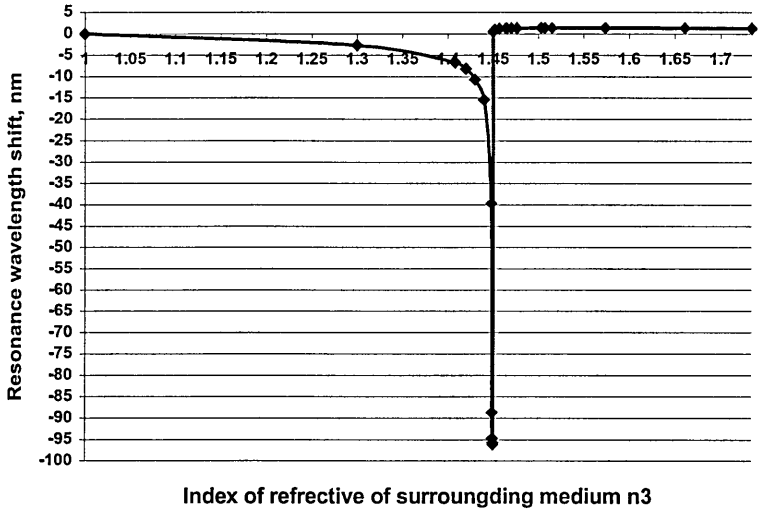

Figure 2. Simulation obtained LPG coupling wavelength of 7*th* resonance shift versus n_3 on a wide range.

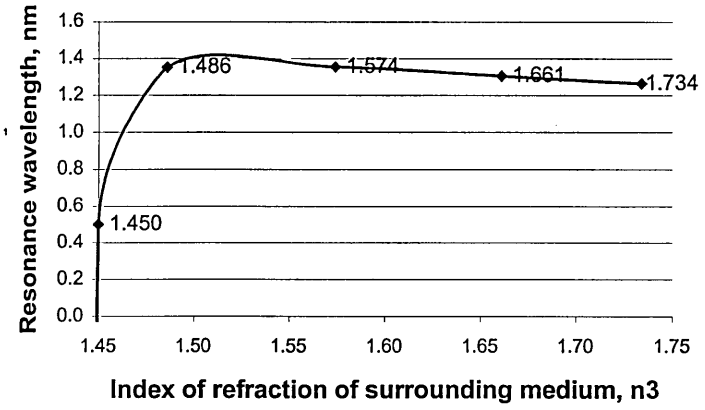

Figure 3. Theoretical results revealing that when the surrounding index is higher than cladding index, the LPG resonance wavelength still shifts.

It was shown that when $n_3 > n_{cl}$, the theoretical leaky coupling wavelengths shift smoothly, but when n_3 is higher than certain value which is around 1.486, the coupling wavelength is decreased. This result shows a good agreement with experimentally measured data as shown in Figure 4.

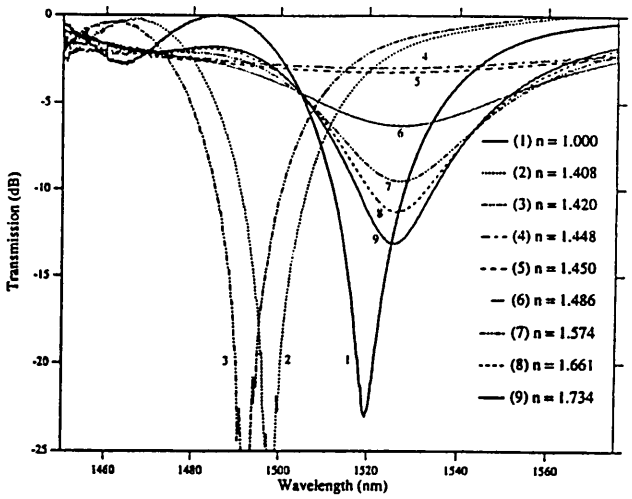

Figure 4. Experimentally measured LPG transmission for several surrounding indexes. [10]

Leaky cladding coupling loss can be calculated but it is out of the scope of the present work. Detail can found in the literature [10].

4. Modelling simulation of gas sensor

Since in most LPG gas sensors the refractive index of the coating materials are higher than the cladding index ($n_{cl} \approx 1.45$), it is useful to be able to apply the above model to simulate an LPG gas sensor.

Data of a coating material called phosphorylated calix-4-resorcinolarene (PC-4-RA) are used in the present work [3]. Index of refraction of thin films of PC-4-RA deposited by Langmuir-Blodgett (LB) technique has been determined by the method of surface plasmon resonance (SPR). On exposure to toluene vapour of concentration in the range 0.1-5% in volume, the index of refraction of PC-4-RA films changes as follows:

initial state is	1.458,
post adsorption to toluene is	1.508,
post recovery is	1.470.

Using this model the LPG coupling wavelength of 7th leaky mode shift was calculated. The results are shown in Figure 6. The calculated values of the wavelength shifts are small as shown in Figure 5. However with the use of optical spectrum analysers of sufficient resolution it is possible to detect such small changes.

From Figure 5 the obtained shift value is small (about 0.14 nm and 0.02 nm), this value can be detected by optical spectrums analyses of sufficient resolution. Currently some coating material for LPG gas sensor is under investigation in our research group.

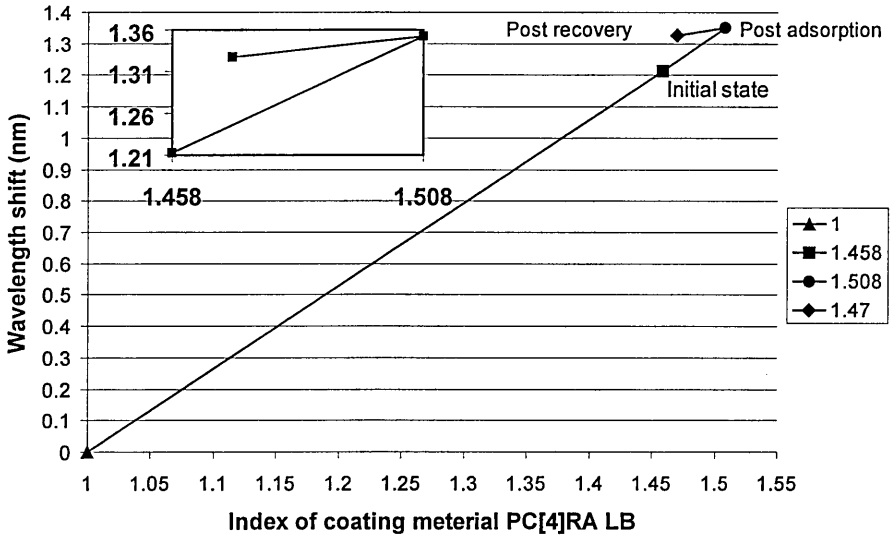

Figure 5. Simulated *7th* leaky mode shift when the coating material PC- 4-RA films exposed to toluene. Inset to shows an enlarged section showing the coupling wavelength shift versus LB film index change.

5. Conclusion

In the leaky waveguide LPG, resonance wavelengths shift have been simulated. The modelling results show that when the refractive index of the surrounding medium is higher than the cladding index, the resonant wavelength shift will be towards to longer wavelength compared to the case n_3 =1. In this case when n_3 is higher than a certain value e.g. n_3 = 1.486, direction of the shift changes back towards the shorter wavelength value. This model can be used to assist the development of environmental monitoring chemical sensors based on the LPG, in which the refractive index of the coating material is higher than that of the cladding.

6. Acknowledgements

The authors gratefully acknowledge Dr. Lin Zhang, Dr. Tom D. P. Allsop and Dr. Wei Zhang (in Photonics Research Group of Aston University, UK) for the technical help and supplying LPG.

References

1. Adams M J 1981 *An Introduction to Optical Waveguides*, John Wiley & Sons,.

2. Duhem O Henninot J F and Douay M 2000 Study of in fibre Mach-Zehnder interferometer based on two spaced 3-dB longperiod gratings surrounded by a refractive index higher than that of silica, *Optics Communications*, **180** 255-262

3. Nabok A V, Hassan A, K Ray A K, Omar O and Kalchenko V I 1997 Study of adsorption of some organic molecules in calix[4]resorcinolarene LB films by surface plasmom resonace, *Sensors and actuators B45* 115-121

4. Lee B H, Liu Y Lee S B and Choi S S 1997 Displacements of the resonant peaks of a long-period fibre gratinginduced by a change of ambient refractive index *Optics Letters.* Vol.22, pp.1769-1771,.

5. Marcuse D 1991 *Theory of Dielectric Optical Waveguides*. Boston.MA:Academic,.

6. Okoshi T 1982 *Optical Fibres*. New York: Academic Press Inc

7. Olivier Duhem, Jean-Francois Henninot, Marc Warenghem, and Marc Douay 1998 Demonstration of long-period-grating efficient couplings with an external medium of a refractive index higher than that of silica *Apllied Optics*. **37**, No.31, 7223-7228,.

8. Patrick H J, Kersey A D, Bucholtz F, Ewing K J, Judkins J B, Vengsarkar A M, 1997 Chemical sensors based on long-period fibre grating response to index of refraction, presented at the *Conf. Lasers and Electro-Optics. Baltimore, MD, CThQ5* 420-421

9. Patrik H J, Kersey A D and Bucholtz F 1998 Analysis of the Response of Long Period Fibre Grating to External Index of Refraction *Journal of lightwave thecnology*, Vol. **16**. No. 9 1606-1612

10. Stegall D B and Erdogan T 1999 Leaky Cladding Mode propagation in Long-Period Fibre Grating Devices *IEEE Photonics technology Letters*, **11** No.3, 343- 345,.

11. Tsao C 1992 *Optical Fibre Waveguide Analysis*, Oxford University Press,.

12. Vengsarkar A M, Lemaire P J, Judkins J B, Bhatia V, Erdogan T. and Sipe J E 1996 Long-period grating as band-rejection filters, *Journal of Lightwave Technology* **14** 58-64,

13. Vikram B and Vengsarkar A M 1996 Optical fibre long-period grating sensors, *Optics Letters* Vol.**21**, No.9, 692-694.

14. Yariv A 1996 *Optical Electronics in Modern Communications*, Oxford University Press

Appendix 3.1 MATLAB code used to determine the fibre Bragg grating reflectivity, for Fig. 2.16.

```
clear all
l=0.84*10^(-3);
A=1.286/2/1.46*10^(-6);
k=pi*1.2*10^(-3)/(1.286*10^(-6));
r=1.282*10^(-6):1*10^(-11):1.290*10^(-6);
db=2*pi*1.46./r-2*pi*1.46/(1.286*10^(-6));
s=sqrt(k^2-db.^2);
R=k^2*sinh(s.*l).^2./(db.^2.*sinh(s.*l).^2
   +s.^2.*cosh(s.*l).^2);
plot(r,R)
hold on
xlabel('wavelangth')
ylabel('relectivity(%)')
```

Appendix 3.2 MATLAB code used to determine increase the fibre Bragg grating reflectivity with grating length, for Fig. 2.17.

```
clear all
clear,clf
xa=0.2*10^(-3):0.1*10^(-4):0.9*10^(-3);
ya=1.28*10^(-6):1*10^(-10):1.29*10^(-6);
k=pi*1.2*10^(-3)/(1.286*10^(-6));
[x,y]=meshgrid(xa,ya);
db=2*pi*1.46./y-2*pi*1.46/(1.286*10^(-6));
s=sqrt(k^2-db.^2);
z=100.*k^2*sinh(s.*x).^2./(db.^2.*sinh(s.*x).^2
   +s.^2.*cosh(s.*x).^2);
plot3(x,y,z)
xlabel('grating')
ylabel('wavelangth')
zlabel('relectivity(%)')
```

Appendix 3.3 MATLAB code used to calculated the ratio of power coupled into cladding mode to the initial power contained in the guided LP_{01} mode through uniform long period gratings, for Fig. 2.19.

```
clear all
x=1370*10^(-9):4*10^(-11):1750*10^(-9);%Wavelength range
L=25e-003;%Grating length
P=600*10^(-6);%period
xm=1550e-009;%designed wavelength
```

```
%k=(pi/xm)*0.32*1e-004;%k.*L=pi/2;
k=3*pi/(2*L);%Coupling coefficient
%Neff =3.1000e-003;
DNeff= 0.00258333333333;
s=pi*DNeff.*(1./x-1/xm);%s=1/2(Bcore-Bcladding-2*pi/A)
P=((sin(L.*sqrt(k^2+s.^2))).^2./(1+(s./k).^2));
plot(x,P,'b');
hold on
x=1370*10^(-9):4*10^(-11):1750*10^(-9);%Wavelength range
L=25e-003;%Grating length
P=600*10^(-6);%period
xm=1550e-009;%Designed wavelength
k=pi/(2*L);%Coupling coefficient
DNeff= 0.00258333333333;%
s=pi*DNeff.*(1./x-1/xm);%s=1/2(Bcore-Bcladding-2*pi/A)
P=((sin(L.*sqrt(k^2+s.^2))).^2./(1+(s./k).^2));
plot(x,P,'r');
hold on
```

Appendix 3.4 MATLAB code used to determine the long period grating transmission for Fig. 2.20.

```
clear all
x=1525*10^(-9):4*10^(-11):1575*10^(-9);%Wavelength range
L=50e-003;%Grating length
A=600*10^(-6);%period
xm=1545e-009;
k=0.39/L;%coupling coefficient
Neff= 0.0042;
s=pi*Neff.*(1./x-1/xm);%s=1/2(Bcore-Bcladding-2*pi/A)
T=(((sin(L.*sqrt(k^2+s.^2))).^2./(1+(k./s).^2))+(cos(L.*sqr
t(k^2+s.^2))).^2);
%transmition
plot(x,T,'b');
hold on
```

Appendix 3.5 MATLAB code used to determine the HE_{11} core mode of Eq.4.99 for Fig.5.6. The plot of $uJ_1(u)/J_0(u)$ And $wK(w)/K_0(w)$with the crossing corresponding to the solution HE_{11} mode.

```
clear all
A=1.550*10^(-6); %wavelength
a1=2.625*10^(-6);%Core radius
n1=1.458;%Core index
k=2*pi./A;
```

```
B=n2*k:n2*k/1e+004:n1*k;% B range
neff=B/k;% x=B propagation constant
u=sqrt(k^2*n1^2-B.^2)*a1;%Normalized effective index
w=sqrt(B.^2-k^2*n2^2)*a1;%V number
LHS=u.*(besselj(1,u)./besselj(0,u));%Left hand side
RHS=w.*(besselk(1,w)./besselk(0,w));%Right hand side
f=LHS-RHS;
plot(B,LHS,'+b',B,RHS,'*r')
grid;
```

Appendix 3.6-1 MATLAB code used to determine the HE_{11} core mode of Eq.5.97 for Fig.5.7. plot $f = uJ_1(u)/J_0(u)-wK(w)/K_0(w)$ a single curve to produce zero-crossing corresponding to the solution of HE_{11} mode

```
A=1.550*10^(-6); %wavelength
a1=2.625*10^(-6);%Core radius
n1=1.458;%Core index
n2=1.45;%Cladding index
k=2*pi./A;
B=n2*k:n2*k/1e+006:n1*k;% B range
neff=B/k;% x=B propagation constant
u=sqrt(k^2*n1^2-B.^2)*a1;%Normalized effective index
w=sqrt(B.^2-k^2*n2^2)*a1;%V number
LHS=u.*(besselj(1,u)./besselj(0,u));%Left hand side
RHS=w.*(besselk(1,w)./besselk(0,w));%Right hand side
f=LHS-RHS;
plot(B,f,'.m')
grid
```

Appendix 3.6-2 MATLAB code used to determine the value of HE_{11} core mode

```
clear all
A=1.550*10^(-6); %wavelength
a1=2.625*10^(-6);%Core radius
n1=1.458;%Core index
n2=1.45;%Cladding index
k=2*pi./A;
B=n2*k:n2*k/1e+004:n1*k;% B range
neff=B/k;% x=B propagation constant
u=sqrt(k^2*n1^2-B.^2)*a1;%Normalized effective index
w=sqrt(B.^2-k^2*n2^2)*a1;%V number
LHS=u.*(besselj(1,u)./besselj(0,u));%Left hand side
```

```
RHS=w.*(besselk(1,w)./besselk(0,w));%Right hand side
f=LHS-RHS;
zeros=0;
index = 1;
for i=1:length(B)-1
   if (f(i)*f(i+1)<0)
      zeros=zeros+1;
      Bco(index)=(B(i)+B(i+1))/2;
      fval(index)=(f(i)+f(i+1))/2;
      index=index+1;
   end
end
for k = 1:length(Bco)
   sent = sprintf('HE1,%d= %f, F value: %0.4f', k,Bco(k),
fval(k));
   disp(sent);
end
total_modes=zeros
```

Appendix 3.7-1 MATLAB code used to determine the HE cladding modes of Eq.5.108, for Fig.5.9.

```
clear all
A=1.55e-006
a1=2.625e-006;
a2=62.5e-006;
k=2*pi/A;
n2=1.45;
n3=1;
x=n2*k:-n2*k/1e+005:n3*k;% x is propagation constant range.
w=a2*sqrt((x.*x)-(n3*n3).*(k.*k));
u=a2*sqrt(((n2*n2).*(k.*k))-(x.*x));
%v=sqrt(u.^2+w.^2);
%u1=a2.*sqrt((n2*n2.*k.*k)-((n3.*k)*(n3.*k)));
JJ=BESSELJ(0,u)-(1./u).*BESSELJ(1,u);
KK=-BESSELK(0,w)-(1./w).*BESSELK(1,w);
HEL=(BESSELJ(0,u)./(u.*BESSELJ(1,u)));
R=sqrt(((n2^2-n3^2)/(2*n2^2))^2.*(KK./(w.*BESSELK(1,w))).^2
+(x/(n2*k)).^2.*(1./u.^2+1./w.^2).^2);
```

```
HER=-(((n2^2+n3^2)/(2*n2^2))^2).*(KK./(w.*BESSELK(1,w)))
+(1./u.^2-R);
y=HEL-HER;
plot(x,y,'b')
grid
zeros=0;
index = 1;
for j=1:length(x)-1
  if ((y(j)*y(j+1)<0))&((y(j)<0.1)&(y(j+1)<0.1))
%&(abs(y(j)-y(j+1))<0.1))
      zeros=zeros+1;
      Bcl(index)=(x(j)+x(j+1))/2;
      yval(index)=(y(j)+y(j+1))/2;
      index=index+1;
   end
end
for kk = 1:length(Bcl)
   sent = sprintf('Cladding modes:HE1,%d= %f, F:%0.4f',
kk,Bcl(kk), yval(kk));
   disp(sent);
end
total_modes=zeros
```

Appendix 3.7-2 The MATLAB codes used to calculate HE cladding mode values

```
clear all
A=1550*10^(-9);
k=2*pi./A;
a2=62.5*10^(-6);
n2 =1.45;
n3=1;
x=n2*k:-n3*k/1e+007:0.997*n2.*k;% range of propagation
constant
%x=n2*k:-n3*k/1e+6:n3*k;
%x=5.877e+006:-n3*k/1e+7:0.998*n2.*k;
%B22=1.0e+006 *5.9080:0.001*n3.*k:n2.*k;
w=a2*sqrt((x.*x)-(n3*n3).*(k.*k));
u=a2*sqrt(((n2*n2).*(k.*k))-(x.*x));
%v=sqrt(u.^2+w.^2);
%u1=a2.*sqrt((n2*n2.*k.*k)-((n3.*k)*(n3.*k)));
JJ=BESSELJ(0,u)-(1./u).*BESSELJ(1,u);
KK=-BESSELK(2,w)+(1./w).*BESSELK(1,w);
```

```
HEL=(BESSELJ(0,u)./(u.*BESSELJ(1,u)));
R=sqrt(((n2^2-n3^2)/(2*n2^2))^2.*(KK./(w.*BESSELK(1,w))).^2
+(x/(n2*k)).^2.*(1./u.^2+1./w.^2).^2);
HER=-(((n2^2+n3^2)/(2*n2^2))^2).*(KK./(w.*BESSELK(1,w)))
+(1./u.^2-R);
f=HEL-HER;
plot(x,f,'b')%,x,HEL,'y',x,HER,'g')
hold on
%B values are obtained where f crosses x axis, (i.e.f=0)
zeros=0;
index = 1;
for i=1:length(x)-1
   if ((f(i)*f(i+1)<0)&(((f(i)*f(i+1))^2)<0.00001))
      zeros=zeros+1;
      Bval(index)=(x(i)+x(i+1))/2;
      fval(index)=(f(i)+f(i+1))/2;
      index=index+1;
   end
end
for k = 1:length(Bval)
   sent = sprintf('HE1,%d= %f, F:%0.4f', k,Bval(k),
fval(k));
   disp(sent);
end
total_modes=zeros
grid
```

Appendix 3.8 MATLAB code used to determine the long-period grating periodicity prediction for Table 5.1 and Fig. 5.11:

```
clear all
for   A=1.1e-006:0.1e-006:1.7e-006;
a1=2.625*10^(-6);
a2=62.5*10^(-6);
n1=1.458+3.6e-004/2;%3.6e-004 is value of peak induced-
index change in core
n2=1.45;
```

```
n3=1;
Z0=377;
k=2*pi./A;
x=n2*k:-n2*k/1e+007:0.994*n2*k;%1.0e+006 *5.87717050691244%
B range
B2=n2*k;
B3=n3*k;
neff=x./k;% x=B propgation constent
b=(neff.^2-n2^2)./(n1^2-n2^2);
V=(2*pi/A)*a1*sqrt(n1^2-n2^2);
d1=(neff./Z0)*i;%(8)
d2=(neff.*Z0)*i;%(9)
u1=sqrt((2*pi/A)^2*(n1^2-neff.^2));%(12),j=1
u2=sqrt((2*pi/A)^2*(n2^2-neff.^2));%(12),j=2
w3=sqrt((2*pi/A)^2*(neff.^2-n3^2));%(13)
u21=1./u2.^2-1./u1.^2;%(10)
u32=1./w3.^2+1./u2.^2;%(11)
JJ1=(1/2).*(besselj(0,u1*a1)-besselj(2,u1*a1));
%diffrective 0f BESSELJ J'(u2*a2)
KK1=-(1/2).*(besselk(0,w3*a2)+besselk(2,w3*a2));%K'(u2*a2)
J=JJ1/(u1.*besselj(1,u1*a1));%(14)
K=KK1/(w3.*besselk(1,w3*a2));%(15)
JJ21=(1/2)*(besselj(0,u2*a1)-besselj(2,u2*a1));%diffrective
0f BESSELJ'(u2*a1)
JJ22=(1/2)*(besselj(0,u2*a2)-besselj(2,u2*a2));%diffrective
0f BESSELJ'(u2*a2)
NN21=(1/2)*(bessely(0,u2*a1)-bessely(2,u2*a1));%diffrective
0f BESSELY'(u2*a1)
NN22=(1/2)*(bessely(0,u2*a2)-bessely(2,u2*a2));%diffrective
0f BESSELY'(u2*a2)
p1=besselj(1,u2*a2).*bessely(1,u2*a1)-
besselj(1,u2*a1).*bessely(1,u2*a2);%(16)
q1=besselj(1,u2*a2).*NN21-JJ21.*bessely(1,u2*a2);%(17)
r1=JJ22.*bessely(1,u2*a1)-besselj(1,u2*a1).*NN22;%(18)
s1=JJ22.*NN21-JJ21.*NN22; %(19)
AA=u2.*(J.*K+(d1.*d2.*u21.*u32)./(n2^2*a1*a2)).*p1
-K.*q1+J.*r1-(1./u2).*s1;
B=-u2.*((u32./(n2^2.*a2)).*J-(u21./(n1^2*a1)).*K).*p1
+(u32./(n1^2*a2)).*q1+(u21./(n1^2*a1)).*r1;
G0=(1./d2).*AA./B;%(6)
G0imag=imag(G0);
C=u2.*((u32/a2).*J-(n3^2.*u21./(n2^2*a1)).*K).*p1
-(u32/a2).*q1-(u21/a1).*r1;
D=u2.*((n3^2/n2^2)*J.*K+d1.*d2.*u21.*u32/(n1^2*a1*a2)).*p1
-(n3^2/n1^2).*K.*q1+J.*r1-(n2^2./(n1^2.*u2)).*s1;
G1=d1.*C./D;%(7)
G1imag=imag(G1);
%y=G-G1; %G=G1
y=G0imag-G1imag;
plot(x,y,'b',x,G0imag,'r',x,G1imag,'g'),grid;

zeros=0;
```

```
index = 1;
for i=1:length(x)-1
  if
((y(i)*y(i+1)<0)&((abs(y(i)))<0.01)&((abs(y(i+1)))<0.01))
      zeros=zeros+1;

      Bcl(index)=(x(i)+x(i+1))/2;
      yval(index)=(y(i)+y(i+1))/2;
      index=index+1;
   end
end
%Core mode
k=2*pi./A;
B=n2*k:n2*k/1e+007:n1*k;% B range
%x=  1.0e+006 * 5.88689304224413;%Bcore value
neff=B/k;% x=B propgation constent
b=(neff.^2-n2^2)/(n1^2-n2^2);
V=k*a1*sqrt(n1^2-n2^2);
YL=V.*sqrt(1-b).*(besselj(1,V.*sqrt(1-b))
./besselj(0,V.*sqrt(1-b)));
YR=V.*sqrt(b).*(besselk(1,V.*sqrt(b))
./besselk(0,V.*sqrt(b)));
f=YL-YR;
%plot(B,YL,'r',B,YR,'g',B,f,'y'),grid;
zeros=0;
index = 1;
for i=1:length(B)-1
   if (f(i)*f(i+1)<0)
      zeros=zeros+1;

      Bco(index)=(B(i)+B(i+1))/2;
      fval(index)=(f(i)+f(i+1))/2;
      index=index+1;
   end
end
for k = 1:length(Bco)
   sent = sprintf('HE1,%d= %f, F value: %0.4f', k,Bco(k),
fval(k));
   disp(sent);
end
total_modes=zeros
A %LPG peak wavelength
k=2*pi./A;
Period=[1e+006*A./(Bco/k-Bcl/k)]% Wavelength unit is μm
end
```

Appendix 3.9 MATLAB code used to determine the long-period grating coupling wavelength resonance shift versus n_3 on a wide range of refractive index for Fig. 5.16.

```
clear all
n3=1.4
   A=1.39e-006:1e-10:1.6e-006;
   for jj=1:length(A);
     sent = sprintf('First guss Wavelength=, %11.9e',
A(jj));
     disp(sent);
k=2*pi/A(jj);
a2=62.5e-006;
n2 =1.45;
x=n2*k:-k/1e+007:0.998*n2*k;% x is propagation constant
range.
w=a2*sqrt((x.*x)-(n3*n3).*(k.*k));
u=a2*sqrt(((n2*n2).*(k.*k))-(x.*x));
%v=sqrt(u.^2+w.^2);
%u1=a2.*sqrt((n2*n2.*k.*k)-((n3.*k)*(n3.*k)));
JJ=BESSELJ(0,u)-(1./u).*BESSELJ(1,u);
KK=-BESSELK(0,w)-(1./w).*BESSELK(1,w);
HEL=(BESSELJ(0,u)./(u.*BESSELJ(1,u)));
R=sqrt(((n2^2-n3^2)/(2*n2^2))^2.*(KK./(w.*BESSELK(1,w))).^2
+(x/(n2*k)).^2.*(1./u.^2+1./w.^2).^2);
HER=-(((n2^2+n3^2)/(2*n2^2))^2).*(KK./(w.*BESSELK(1,w)))
+(1./u.^2-R);
y=HEL-HER;
figure(1)
plot(x,y,'r');
Title('Cladding modes')
xlabel('x')
ylabel(' y=HEL-HER ')
grid
zeros=0;
index = 1;
for j=1:length(x)-1
  if ((y(j)*y(j+1)<0)&(y(j)>0)&(y(j+1)<0))
      zeros=zeros+1;
      Bcl(index)=(x(j)+x(j+1))/2;
      yval(index)=(y(j)+y(j+1))/2;
      index=index+1;
   end
end
for k = 1:length(Bcl)
   sent = sprintf('Cladding modes:HE1,%d= %f, F:%0.4f',
k,Bcl(k), yval(k));
   disp(sent);
end
total_modes=zeros
```

%Core mode

```
a1=2.5*10^(-6);
a2=62.5*10^(-6);
n1=1.45656937670071;
n2=1.45;
```

```
k=2*pi/A(jj);
B=n2*k:n2*k/1e+7:n1*k;% B range
%x=  1.0e+006 * 5.88689304224413;%Bcore value
neff=B/k;% x=B propgation constent
b=(neff.^2-n2^2)/(n1^2-n2^2);
V=k*a1*sqrt(n1^2-n2^2);
YL=V.*sqrt(1-b).*(besselj(1,V.*sqrt(1-b))
./besselj(0,V.*sqrt(1-b)));
YR=V.*sqrt(b).*(besselk(1,V.*sqrt(b))
./besselk(0,V.*sqrt(b)));
f=YL-YR;
figure(2)
plot(B,f,'r');
Title('Core mode')
xlabel('B')
ylabel(' f=YL-YR ')
grid
zeros=0;
index = 1;
for i=1:length(B)-1
   if (f(i)*f(i+1)<0)
      zeros=zeros+1;
      Bco(index)=(B(i)+B(i+1))/2;
      fval(index)=(f(i)+f(i+1))/2;
      index=index+1;
   end
end
for kk = 1:length(Bco)
sent =sprintf('HE1,%d= %f, F:%0.4f', kk,Bco(kk), fval(kk));
      %sent = sprintf('HE1,%d= %f, F value: %0.4f',
k,Bco(kk), fval(kk));
   disp(sent);
end
total_modes=zeros
%Period
DP=454.1e-006;% DP=design period of LPG
I=Bcl./Bcl;
BBco=Bco.*I;
k=2*pi/A(jj);
CP(jj)=A(jj)/(BBco(6)/k-Bcl(6)/k)% CP=Calculate Period
% Bcl(6) is just  calculate HE1,6 cladding mode
   if (CP(jj)>DP & CP(jj-1)<DP)
      Wavelength(jj)=(A(jj)+A(jj-1))/2
      Period(jj)=( CP(jj)+ CP(jj-1))/2
      sent =
sprintf('FindWavelength= %11.9e', (A(jj)+A(jj-1))/2);
      disp(sent);
      stop
       end
end
```

Appendix 3.10 MATLAB code used to determining the Long-period grating transmissions value(core mode, cladding mode and coupling wavelength)which show that when surrounding index n_3 is changed, the coupling wavelength shifts, and the transmission amplitude also changws, for Fig. 5.31.

```
%  MATLAB code for calculation the coupling wavelength
(three layer
%  cladding mode) when n3 changes:

%  Cladding mode
clear all
format long;
n3=1.4472%:0.01:1.55;
for l=1:length(n3);
   A=1.5669026*10^(-6):0.1*10^(-8):1.9*10^(-6);
   for jj=1:length(A);
     sent = sprintf('A=, %11.9e', A(jj));
     disp(sent);
a1=2.625*10^(-6);
a2=62.5*10^(-6);
n1=1.458+1e-004/2;%1e-004 is value of peak induced-index
change in core
n2=1.45;
Z0=377;
k=2*pi/A(jj);
x=n2*k:-n2*k/1e+007:0.998*n2*k;%1.0e+006 *5.87717050691244%
B range
B2=n2*k;
B3=n3*k;
neff=x/k;% x=B propgation constent
b=(neff.^2-n2^2)/(n1^2-n2^2);
V=(2*pi/A(jj))*a1*sqrt(n1^2-n2^2);
d1=(neff/Z0)*i;%(8)
d2=(neff*Z0)*i;%(9)
u1=sqrt((2*pi/A(jj))^2*(n1^2-neff.^2));%(12),j=1
u2=sqrt((2*pi/A(jj))^2*(n2^2-neff.^2));%(12),j=2
w3=sqrt((2*pi/A(jj))^2*(neff.^2-n3^2));%(13)
u21=1./u2.^2-1./u1.^2;%(10)
u32=1./w3.^2+1./u2.^2;%(11)
JJ1=(1/2).*(besselj(0,u1*a1)-besselj(2,u1*a1));
%diffrective Of BESSELJ J'(u2*a2)
KK1=-(1/2).*(besselk(0,w3*a2)+besselk(2,w3*a2));%K'(u2*a2)
J=JJ1/(u1.*besselj(1,u1*a1));%(14)
K=KK1/(w3.*besselk(1,w3*a2));%(15)
JJ21=(1/2)*(besselj(0,u2*a1)-besselj(2,u2*a1));%diffrective
Of BESSELJ'(u2*a1)
```

```
JJ22=(1/2)*(besselj(0,u2*a2)-besselj(2,u2*a2));%diffrective
0f BESSELJ'(u2*a2)
NN21=(1/2)*(bessely(0,u2*a1)-bessely(2,u2*a1));%diffrective
0f BESSELY'(u2*a1)
NN22=(1/2)*(bessely(0,u2*a2)-bessely(2,u2*a2));%diffrective
0f BESSELY'(u2*a2)
p1=besselj(1,u2*a2).*bessely(1,u2*a1)-
besselj(1,u2*a1).*bessely(1,u2*a2);%(16)
q1=besselj(1,u2*a2).*NN21-JJ21.*bessely(1,u2*a2);%(17)
r1=JJ22.*bessely(1,u2*a1)-besselj(1,u2*a1).*NN22;%(18)
s1=JJ22.*NN21-JJ21.*NN22; %(19)
AA=u2.*(J.*K+(d1.*d2.*u21.*u32)./(n2^2*a1*a2)).*p1
-K.*q1+J.*r1-(1./u2).*s1;
B=-u2.*((u32./(n2^2.*a2)).*J-(u21./(n1^2*a1)).*K).*p1
+(u32./(n1^2*a2)).*q1+(u21./(n1^2*a1)).*r1;
G0=(1./d2).*AA./B;%(6)
G0imag=imag(G0);
C=u2.*((u32/a2).*J-(n3^2.*u21./(n2^2*a1)).*K).*p1
-(u32/a2).*q1-(u21/a1).*r1;
D=u2.*((n3^2/n2^2)*J.*K+d1.*d2.*u21.*u32/(n1^2*a1*a2)).*p1
-(n3^2/n1^2).*K.*q1+J.*r1-(n2^2./(n1^2.*u2)).*s1;
G1=d1.*C./D;%(7)
G1imag=imag(G1);
%y=G-G1; %G=G1
y=G0imag-G1imag;
plot(x,y,'b',x,G0imag,'r',x,G1imag,'g'),grid;
zeros=0;
index = 1;
for i=1:length(x)-1
  if
((y(i)*y(i+1)<0)&((abs(y(i)))<0.01)&((abs(y(i+1)))<0.01))
      zeros=zeros+1;
      Bcl(index)=(x(i)+x(i+1))/2;
      yval(index)=(y(i)+y(i+1))/2;
      index=index+1;
   end
end
%Core mode
k=2*pi./A(jj);
B=n2*k:n2*k/1e+007:n1*k;% B range
%x=  1.0e+006 * 5.88689304224413;%Bcore value
neff=B/k;% x=B propgation constent
b=(neff.^2-n2^2)/(n1^2-n2^2);
V=k*a1*sqrt(n1^2-n2^2);
YL=V.*sqrt(1-b).*(besselj(1,V.*sqrt(1-b))
./besselj(0,V.*sqrt(1-b)));
YR=V.*sqrt(b).*(besselk(1,V.*sqrt(b))
./besselk(0,V.*sqrt(b)));
f=YL-YR;
%plot(B,YL,'r',B,YR,'g',B,f,'y'),grid;
zeros=0;
index = 1;
```

```
for i=1:length(B)-1
   if (f(i)*f(i+1)<0)
      zeros=zeros+1;
      Bco(index)=(B(i)+B(i+1))/2;
      fval(index)=(f(i)+f(i+1))/2;
      index=index+1;
   end
end
for k = 1:length(Bco)
   sent = sprintf('HE1,%d= %f, F value: %0.4f', k,Bco(k),
fval(k));
   disp(sent);
end
total_modes=zeros
%Period
DP=570e-006;
k=2*pi/A(jj);
CP(jj)=A(jj)/(Bco/k-Bcl(5)/k)% for cladding mode 2
%%%
DP=570e-006;
     if (CP(l,jj)>DP & CP(jj-1)<DP)
    W(l,j)=(A(jj)+A(jj-1))/2
    P(l,jj)=(CP(jj)+CP(jj-1))/2
     end
end
end
```

Appendix 3.11 MATLAB code used to determining the Long-period grating transmissions which show that when index n_3 change from n_3=1 to n_3 = 1.447, the coupling wavelength shifts, and the transmission amplitude also changws, for Fig. 5.31.

```
clear all
% n3=1,
x=1.4:4*10^(-4):1.7 %wavelangth range
wave=1.5669026
L=25e+003;%LPG period Length μ m
A=570;% pitch of period
KK= 0.4725 %coupling constant
dn=1e-004 %
k=dn*KK
kk=2*pi/wave % wave number
Bco=5.823285, % propagation constant in core
Bcl=5.811457, % propagation constant in cladding
Neff =Bco./kk-Bcl./kk;
xm=wave;%peak wavelength
s=pi.*Neff.*(1./x-1./xm);%s=1/2(Bcore-Bcladding-2*pi/A)
```

```
T=10.*LOG10(((sin(L.*sqrt(k^2+s.^2))).^2./(1+(k./s).^2))+(c
os(L.*sqrt(k^2+s.^2))).^2);%transmition
plot(x,T,'m');
hold on

% n3=1.447
x=1.4:4*10^(-4):1.7%wave range
wave= 1.5390
L=25e+003;%period Length
A=570;%period
KK=0.4262 %Coupling constant k_{m-01}^{cl-co}
dn=1e-004%3.6e-004
k=dn*KK
kk=2*pi/wave
Bco=5.929245
Bcl=5.917883
Neff =Bco./kk-Bcl./kk;
xm=wave;%peak wavelength
s=pi.*Neff.*(1./x-1./xm);%s=1/2(Bcore-Bcladding-2*pi/A)
T=10.*LOG10(((sin(L.*sqrt(k^2+s.^2))).^2./(1+(k./s).^2))+(c
os(L.*sqrt(k^2+s.^2))).^2);%transmition
plot(x,T,'c');
hold on
```

Appendix 3.12 MATLAB code used to determine the coupling constant k_{m-01}^{cl-co} for Eq.5.140.

```
%Cladding modes
clear all
format short;
a1=2.625;
a2=62.5;
n1=1.458;
n2=1.45;
n3=1;
Z0=377;
A=1.55;%Wavelength
k=2*pi./A;
x=n2*k:-n3*k/1e+007:n3*k;% x is propagation constant range.
neff=x./k;% x=B propagation constant
V=(2*pi/A)*a1*sqrt(n1^2-n2^2);
d1=(neff./Z0)*i;%Eq.(8)
d2=(neff.*Z0)*i;%Eq.(9)
u1=sqrt((2*pi/A)^2.*(n1^2-neff.^2));%Eq.(12),j=1
u2=sqrt((2*pi/A)^2.*(n2^2-neff.^2));%Eq.(12),j=2
w3=sqrt((2*pi/A)^2.*(neff.^2-n3^2));%Eq.(13)
u21=1./u2.^2-1./u1.^2;%Eq.(10)
u32=1./w3.^2+1./u2.^2;%Eq.(11)
JJ1=(1/2).*(besselj(0,u1*a1)-besselj(2,u1*a1));
```

```
 %diffrective of BESSELJ J'(u1*a1)
KK1=-(1/2).*(besselk(0,w3*a2)+besselk(2,w3*a2));%K'(w3*a2)
J=JJ1./(u1.*besselj(1,u1*a1));%Eq.(14)
K=KK1./(w3.*besselk(1,w3*a2));%Eq.(15)
JJ21=(1/2).*(besselj(0,u2*a1)-besselj(2,u2*a1));
%diffrective of BESSELJ'(u2*a1)
JJ22=(1/2).*(besselj(0,u2*a2)-besselj(2,u2*a2));
%diffrective of BESSELJ'(u2*a2)
NN21=(1/2).*(bessely(0,u2*a1)-bessely(2,u2*a1));
%diffrective of BESSELY'(u2*a1)
NN22=(1/2).*(bessely(0,u2*a2)-bessely(2,u2*a2));
%diffrective of BESSELY'(u2*a2)
p1=besselj(1,u2*a2).*bessely(1,u2*a1)-
besselj(1,u2*a1).*bessely(1,u2*a2);%Eq.(16)
q1=besselj(1,u2*a2).*NN21-JJ21.*bessely(1,u2*a2);%Eq.(17)
r1=JJ22.*bessely(1,u2*a1)-besselj(1,u2*a1).*NN22;%Eq.(18)
s1=JJ22.*NN21-JJ21.*NN22; %Eq.(19)
AA=u2.*(J.*K+(d1.*d2.*u21.*u32)./(n2^2*a1*a2)).*p1-
K.*q1+J.*r1-(1./u2).*s1;%Eq.(6) numerator
B=-u2.*((u32./(n2^2.*a2)).*J-(u21./(n1^2*a1)).*K).*p1
+(u32./(n1^2*a2)).*q1+(u21./(n1^2*a1)).*r1;
%Eq.(6) denominator
G0=(1./d2).*AA./B;%Eq.(6)
G0imag=imag(G0);
C=u2.*((u32/a2).*J-(n3^2.*u21./(n2^2*a1)).*K).*p1
-(u32/a2).*q1-(u21/a1).*r1;%Eq.(7) numerator
D=u2.*((n3^2/n2^2)*J.*K+d1.*d2.*u21.*u32/(n1^2*a1*a2)).*p1
-(n3^2/n1^2).*K.*q1+J.*r1-(n2^2./(n1^2.*u2)).*s1;
%Eq.(7) denominator
G1=d1.*C./D;%Eq.(7)
G1imag=imag(G1);
y=G0imag-G1imag;
figure(1)
plot(x,y,'b',x,G0imag,'r',x,G1imag,'g'),grid;
hold on
zeros=0;
index = 1;
for j=1:length(x)-1
  if ((y(j)*y(j+1)<0)&(abs(y(j)-y(j+1))<0.1))
      zeros=zeros+1;
      Bcl(index)=(x(j)+x(j+1))/2;
      yval(index)=(y(j)+y(j+1))/2;
      index=index+1;
   end
end
for k = 1:length(Bcl)
   sent = sprintf('Cladding modes:HE1,%d= %f, F:%0.4f',
k,Bcl(k), yval(k));
   disp(sent);
end
total_modes=zeros
```

```
%Calculate the field normalization constant E1v
x=Bcl;
k=2*pi./A;
neff=x/k;% x=B propgation constent
V=(2*pi/A)*a1*sqrt(n1^2-n2^2);
d1=(neff./Z0)*i;%Eq.(8)
d2=(neff.*Z0)*i;%Eq.(9)
u1=sqrt((2*pi/A)^2.*(n1^2-neff.^2));%Eq.(12),j=1
u2=sqrt((2*pi/A)^2.*(n2^2-neff.^2));%Eq.(12),j=2
w3=sqrt((2*pi/A)^2.*(neff.^2-n3^2));%Eq.(13)
u21=1./u2.^2-1./u1.^2;%Eq.(10)
u32=1./w3.^2+1./u2.^2;%Eq.(11)
JJ1=(1/2).*(besselj(0,u1*a1)-besselj(2,u1*a1));
%diffrective 0f BESSELJ J'(u1*a1)
KK1=-(1/2).*(besselk(0,w3*a2)+besselk(2,w3*a2));
%K'(w3*a2)
J=JJ1./(u1.*besselj(1,u1*a1));%Eq.(14)
K=KK1./(w3.*besselk(1,w3*a2));%Eq.(15)
JJ21=(1/2).*(besselj(0,u2*a1)-besselj(2,u2*a1));
%diffrective 0f BESSELJ'(u2*a1)
JJ22=(1/2).*(besselj(0,u2*a2)-besselj(2,u2*a2));
%diffrective 0f BESSELJ'(u2*a2)
NN21=(1/2).*(bessely(0,u2*a1)-bessely(2,u2*a1));
%diffrective 0f BESSELY'(u2*a1)
NN22=(1/2).*(bessely(0,u2*a2)-bessely(2,u2*a2));
%diffrective 0f BESSELY'(u2*a2)
p1=besselj(1,u2*a2).*bessely(1,u2*a1)-
besselj(1,u2*a1).*bessely(1,u2*a2);%(16)
q1=besselj(1,u2*a2).*NN21-JJ21.*bessely(1,u2*a2);
%Eq.(17)
r1=JJ22.*bessely(1,u2*a1)-besselj(1,u2*a1).*NN22;
%Eq.(18)
s1=JJ22.*NN21-JJ21.*NN22; %Eq.(19)
AA=u2.*(J.*K+(d1.*d2.*u21.*u32)./(n2^2*a1*a2)).*p1-
K.*q1+J.*r1-(1./u2).*s1;%Eq.(6) numerator
B=-u2.*((u32./(n2^2.*a2)).*J-(u21./(n1^2*a1)).*K).*p1
+(u32./(n1^2*a2)).*q1+(u21./(n1^2*a1)).*r1;
%Eq.(6) denominator
G0=(1./d2).*AA./B;%Eq.(6)
J011=besselj(0,u1*a1);
J111=besselj(1,u1*a1);
J211=besselj(2,u1*a1);
J311=besselj(3,u1*a1);
J021=besselj(0,u2*a1);
J022=besselj(0,u2*a2);
J121=besselj(1,u2*a1);
J122=besselj(1,u2*a2);
J221=besselj(2,u2*a1);
J222=besselj(2,u2*a2);
J321=besselj(3,u2*a1);
J322=besselj(3,u2*a2);
```

```
N021=bessely(0,u2*a1);
N022=bessely(0,u2*a2);
N121=bessely(1,u2*a1);
N122=bessely(1,u2*a2);
N221=bessely(2,u2*a1);
N222=bessely(2,u2*a2);
N321=bessely(3,u2*a1);
N322=bessely(3,u2*a2);

OJ=a2^2.*(J222.^2-J122.*J322)-a1^2.*(J221.^2-J121.*J321);
ON=a2^2.*(N222.^2-N122.*N322)-a1^2.*(N221.^2-N121.*N321);
OJN=a2^2.*(J222.*N222-(1/2).*(J122.*N322+J322.*N122))-
a1.^2.*(J221.*N221-0.5*(J121.*N321+J321.*N121));
OOJ=a2^2.*(J222.^2+J122.^2)-a1^2.*(J221.^2+J121.^2);
OON=a2^2.*(N222.^2+N122.^2)-a1^2.*(N221.^2+N121.^2);
OOJN=a2^2.*(J022.*N022+J122.*N122)-
a1^2.*(J021.*N021+J121.*N121);

Q=OJ.*N121.^2+ON.*J121.^2-2*OJN.*J121.*N121;%Eq.(B4)
QQ=OOJ.*N121.^2+OON.*J121.^2-2.*OOJN.*J121.*N121;%Eq.(B5)
R=(1/4).*OJ.*(N221-N021).^2+(1/4).*ON.*(J221-J021).^2
-(1/2).*OJN.*(N221-N021).*(J221-J021);%Eq.(B6)
RR=(1/4).*OOJ.*(N221-N021).^2+(1/4).*OON.*(J221-J021).^2
-(1/2).*OOJN.*(N221-N021).*(J221-J021);%Eq.(B7)
S=(1/2).*OJ.*N121.*(N021-N221)+(1/2).*ON.*J121.*(J021-
J221)-(1/2).*OJN.*(N121.*(J021-J221)
+J121.*(N021-N221));%Eq.(B8)
SS=(1/2).*OOJ.*N121.*(N021-N221)+(1/2).*OON.*J121.*(J021-
J221)-(1/2).*OOJN.*(N121.*(J021-J221)+J121.*(N021-
N221));%Eq.(B9)

P11=(neff/Z0-((neff*Z0.*G0.^2)/(n1^2))
+(1+(neff.^2)/(n1^2)).*imag(G0));%part of Eq.(B2)
P12=(neff/Z0-((neff*Z0.*G0.^2)/(n1^2))
-(1+(neff.^2)/(n1^2)).*imag(G0));%part of Eq.(B2)
P1=((pi*a1^2.*u1.^2)/4).*(P11.*(J211.^2-
J111.*J311)+P12.*(J011.^2+J111.^2));%Eq.(B2)
u21=1./u2.^2-1./u1.^2;%Eq.(10)
J=JJ1./(u1.*besselj(1,u1*a1));
d1=(neff./Z0)*i;%Eq.(8)
d2=(neff.*Z0)*i;%Eq.(9)
F2=J-(u21.*d2.*G0)/(n1^2*a1);
G2=G0.*J+u21.*d1/a1;
ne2=(1+neff.^2/n2^2);
P21=(neff/Z0.*F2.^2-(neff*Z0/n2^2).*G2.^2).*(Q+QQ);
%part of Eq.(B3)
P22=(1./(u2.^2)).*(neff/Z0
-neff.*Z0.*n2^2.*G0.^2/n1^4).*(R+RR); %part of Eq.(B3)
P23=ne2.*F2.*imag(G2).*(Q-QQ)
+ne2.*(n2^2)./(n1^2.*u2.^2).*imag(G0).*(R-RR);
%part of Eq.(B3)
```

```
P24=ne2.*(((n2^2.*imag(G0))./(n1^2.*u2)).*F2
+1./u2.*imag(G2)).*(S-SS);%part of Eq.(B3)
P25=((2*neff./u2).*((Z0.*G0/(n1^2)).*G2
-(1/Z0).*F2).*(S+SS));%part of Eq.(B3)
P2=((pi^3*a1^2.*u1.^4.*u2.^2.*J111.^2)/16).*(P21+P22+P23
-P24+P25);%in Eq(B3):(P21+P22+P23-P24'+'P25);
K032=besselk(0,w3*a2);
K132=besselk(1,w3*a2);
K232=besselk(2,w3*a2);
K332=besselk(3,w3*a2);
ne3=1+neff.^2/n3^2;
F3=-F2.*p1+(1./u2).*q1;
G3=-(n3^2/n2^2).*(G2.*p1+(n2^2.*G0./(n1^2.*u2)).*q1);
P31=((neff*Z0/n3^2).*G3.^2-(neff/Z0).*F3.^2
-ne3.*F3.*imag(G3)).*(K232.^2-K132.*K332);%part of Eq.(B16)
P32=(((neff*Z0/n3^2).*G3.^2-(neff/Z0).*F3.^2
+ne3.*F3.*imag(G3)).*(K032.^2-K132.^2));%part of Eq.(B16)
P3=((pi^3.*a1^2.*a2^2.*u1.^4.*u2.^4.*J111.^2)./(16.*w3.^2.*
K132.^2)).*(P31+P32);%Eq.(B16)
E1v=sqrt(1./(P1+P2+P3));
%plot(Bcl,E1v,'r')
hold on

%Core mode
A=1.55;%LPG peak wavelength
a1=2.625;%Core radia
a2=62.5;%Cladding radia
n1=1.458;%Core index
n2=1.45;%Cladding index
n3=1;%Souround index
k=2*pi./A;
B=n2*k:n2*k/1000000:n1*k;% B range
neff=B/k;% x=B propgation constent
b=(neff.^2-n2^2)/(n1^2-n2^2);%Normalized effective index
V=k*a1*sqrt(n1^2-n2^2);%V number
YL=V.*sqrt(1-b).*(besselj(1,V.*sqrt(1-b))
./besselj(0,V.*sqrt(1-b)));%Eq.(1) Left side
YR=V.*sqrt(b).*(besselk(1,V.*sqrt(b))
./besselk(0,V.*sqrt(b)));%Eq.(1) Right side
f=YL-YR;
%plot(B,f,'g'),grid;
%plot(B,YL,'r',B,YR,'k',B,f,'r'),grid;
hold on
zeros=0;
index = 1;
for j=1:length(B)-1
   if (f(j)*f(j+1)<0)
      zeros=zeros+1;
      Bco(index)=(B(j)+B(j+1))/2;
      fval(index)=(f(j)+f(j+1))/2;
      index=index+1;
   end
```

```
end
for k = 1:length(Bco)
   sent = sprintf('Core mode:HE1,%d= %f, F value: %0.4f',
k,Bco(k), fval(k));
   disp(sent);
end
total_modes=zeros
%Plot coupling constant Kcl-co
m=1:length(x);
figure(2)
A=1.55;
k=2*pi./A;
neffco=Bco/k;
b=(neffco.^2-n2^2)/(n1^2-n2^2);%Normalized effective index
D=(n1-n2)/n1;
K1=((pi*b)/(Z0*n2*sqrt(1+2*b*D)))^0.5;
K2=(n1^2.*u1)./(u1.^2-(V^2*(1-b)/(a1^2)));
K3=(1+(d2.*G0)/(n1^2));
K4=u1.*BESSELJ(1,u1*a1);
K5=BESSELJ(0,V*sqrt(1-b))/BESSELJ(1,V*sqrt(1-b));
K6=((V*sqrt(1-b))/a1).*BESSELJ(0,u1*a1);
Kclco=abs(k.*K1.*K2.*K3.*E1v.*(K4.*K5-K6))%Eq.(36)
plot(m,Kclco,'*r'),grid;
hold on
```

Appendix 4 General Coupled Mode Theory Formalism

The derivation in this section closely follows the work by Erdogan [Erdogan 1997], which begins by writing the transverse component of the electric field in the ideal-mode approximation to coupled-mode theory as a superposition of the ideal modes (the modes in an ideal waveguide where no grating perturbation j exist). Given that the modes are labelled index j, we then have:

$$E_t^{\ T}(x,y,z,t) = \sum_j \left[A_j(z)\exp(i\beta_j z) + B_j(z)\exp(-i\beta_j z)\right] e_{jt}^{\ T}(x,y)\exp(-i\omega t) \qquad \text{(A.1)}$$

Where the coefficients $A_j(z)$ and $B_j(z)$ are slowly varying amplitudes of the jth mode Travelling in the +z and –z directions, respectively, and the propagation constants β is simply $\beta = (2\pi/\lambda)\, n_{eff}$. The transverse mode field $e_j^{\ T}(x,y)$ might describe the bound-core mode or they might describe cladding modes. While the modes are orthogonal in an ideal waveguide and hence, do not exchange energy, the presence of a dielectric perturbation causes the modes to be coupled such that amplitudes A_j and B_j of the jth mode evolve along the z-axis according to:

$$\frac{dA_j}{dz} = i\sum_k A_k\left(K_{kj}^{\ t} + K_{kj}^{\ z}\right)\exp\left[i\left(\beta_k - \beta_j\right)z\right] + i\sum_k B_k\left(K_{kj}^{\ t} - K_{kj}^{\ z}\right)\exp\left[-i\left(\beta_k + \beta_j\right)z\right] \qquad \text{(A.2)}$$

$$\frac{dB_j}{dz} = -i\sum_k A_k\left(K_{kj}^{\ t} - K_{kj}^{\ z}\right)\exp\left[i\left(\beta_k + \beta_j\right)z\right] - i\sum_k B_k\left(K_{kj}^{\ t} + K_{kj}^{\ z}\right)\exp\left[-i\left(\beta_k - \beta_j\right)z\right] \qquad \text{(A.3)}$$

in Eq. A.2 and Eq. A.3, $K_{kj}^{\ t}(z)$ is the transverse coupling coefficient between modes j and k given by:

$$K_{kl}^{\ t}(z) = \frac{\omega}{4}\iint_{\infty} dxdy\,\Delta\varepsilon(x,y,z)\vec{e}_{kt}(x,y) * \vec{e}^{\,*}_{jt}(x,y) \qquad \text{(A.4)}$$

Where $\Delta\varepsilon$ is the perturbation to the permittivity, approximately $\Delta\varepsilon \cong 2n\delta n$ when $\delta n << n$. The longitudinal coefficient $K_{kj}{}^{z}$ is analogous to $K_{kj}{}^{t}$, but generally $K_{kj}{}^{z} << K_{kj}{}^{t}$ for fibre modes, and thus this coefficient is usually neglected.

In most fibre gratings the induced index change $\delta n(x,y,z)$ is approximately uniform across the core and non-existent outside the core. We can thus describe the core index by an expression:

$$\delta n_{co-eff}(z) = \bar{\delta} n_{co-eff}(z)\left\{1 + v\cos\left[\frac{2\pi}{\Lambda}z + \phi(z)\right]\right\} \tag{A.5}$$

where $\bar{\delta} n_{co-eff}$ is the "dc" index change spatially averaged over a grating period, v is the fringe visibility of the index change, Λ is the period, and $\phi(z)$ describes grating chirp. If we define two new coefficients

$$\sigma_{kj}(z) = \frac{\omega n_{co}}{2}\bar{\delta} n_{co}(z)\iint_{core} dxdy\vec{e}_{kt}(x,y) * \vec{e}^{*}{}_{jt}(x,y) \tag{A.6}$$

$$k_{kj}(z) = \frac{v}{2}\sigma_{kj}(z) \tag{A.7}$$

Where $\sigma_{kj}(z)$ is a "dc" (period-averaged) coupling coefficient and $k_{kj}(z)$ is an "ac" coupling coefficient, then the general coupling coefficient can be written:

$$K_{kj}{}^{t}(z) = \sigma_{kj}(z) + 2k_{kj}(z)\cos\left[\frac{2\pi}{\Lambda}z + \phi(z)\right] \tag{A.8}$$

Eqs.A.2 - A.8 are the coupled-mode equations that we use to describer fibre-grating spectra.